Development of a nose landing gear of an unmanned aircraft (RPAS)

José Miguel Casaca Faria Silva

Dissertação de Mestrado

Orientador na FEUP: Prof. António Torres Marques
Orientadora na empresa: Engª. Inês Lopes Martins

U.PORTO

FEUP **FACULDADE DE ENGENHARIA**
UNIVERSIDADE DO PORTO

Mestrado Integrado em Engenharia Mecânica

Março de 2017

Resumo

A proposta deste estudo partiu de Eng. Renato Machado, da empresa CEiiA em Matosinhos, Porto.

O objetivo deste trabalho foi desenvolver um trem de aterragem frontal em compósitos para a aeronave UAS30 P1, com características superiores às do anteriormente desenvolvido, que apresentava problemas de integridade em aterragens mais bruscas.

O CEiiA já sabia que há no mercado UAVs cujos trens de aterragem são lâminas compósitas curvas e pretendia saber se essa solução seria viável para o projeto UAS30.

Primeiramente foi feita uma investigação do estado da arte a nível de trens de aterragem (Tecnologia, legislação atual e materiais compósitos). Considerando os requisitos impostos pelo CEiiA e pelas legislações, o próximo passo foi escolher o tipo de trem de aterragem.

Foi feito um estudo aprofundado dos fundamentos teóricos (modelos teóricos de vigas curvas (Stress e deslocamento horizontal e vertical em vigas circulares e elípticas) relativamente às cargas que o trem se encontra sujeito baseado em legislações atuais, tendo ainda sido efetuadas correções que foram devidamente comunicadas às entidades responsáveis.

Foi efetuado um estudo preliminar de design, nomeadamente a nível de parâmetros que poderiam ser variados e de seguida um estudo mais pormenorizado. Foi também desenvolvido um programa em software MATLAB® que permite rapidamente ter uma noção dos resultados a esperar para um determinado laminado, com determinado material e geometria curva. Isto possibilita que se evite a repetição de vários testes a nível de software de elementos finitos, permitindo uma poupança de tempo considerável. Para além disto foi também desenhada uma base de testes para trens de aterragem frontais.

O protótipo final encontra-se neste momento em fase de produção na empresa pelo que não foi possível efetuar até à data os testes inicialmente previstos. Contudo, foram realizadas simulações FEM de forma a validar o conceito.

Palavras Chave: Trem de aterragem frontal, aeronave, UAV, Drone, RPAS, Método elementos finitos, FEM.

Development of a nose landing gear of an unmanned aircraft

Abstract

This challenge was proposed by Engineer Renato Machado, from CEiiA at Matosinhos, Porto, Portugal.

The main objective was to develop a new and better nose landing gear in composite materials for the prototype of the aircraft UAS30 P1.

CEiiA had already probed the UAVs market and found that there were some models with composite curved leaf spring nose landing gears. With this, it was needed to find out if this was a viable solution.

At first, an investigation about the state of the art of the landing gear's (Landing Gear technology, Legislation and Composite materials) was done. Taking into account the requirements imposed by CEiiA and by legislations, the next step was to choose a type of landing gear.

A deep study was performed, considering theoretical fundamentals (studying theoretical models of curved beams (Stress, horizontal and vertical displacement) – Circular and elliptic beams), loads that the landing gear has to stand, based on actual legislation for UAV/RPAS and even correcting part of the legislation. This corrections were communicated to the responsible entities.

A software tool was developed with MATLAB® software that provides a first approximation of the results that should be expected for a certain laminate with a certain material and curved geometry. This allows a faster approach to the problem, avoiding repetitive finite element tests.

A test base for nose landing gears was also designed.

The final prototype is currently in production at the company, thus, it was not possible to perform the initial planned tests until this moment. However, Finite Element simulations were performed in order to validate the concept.

Keywords: Nose landing gear, Aircraft, UAV, RPAS, Finite Element Method, Drone, FEM

Acknowledgements

I would like to thank my advisor Inês Lopes Martins for all the patience and motivation while guiding me through an infinite circle of content and discussion. With her critical but and great curious spirit I could improve my working capacities.

I would like to express my gratitude to my co-advisor Prof. Dr. António Torres Marques for his support and readiness to explain any doubtful subject about my research.

I would like to recognize CEiiA for offering me the opportunity to learn new subjects with a great team of experts.

Finally, I must express my gratitude to my family and girlfriend for all the encouragement and support through the process of studying and writing this thesis.

Acronyms

ANAC - Autoridade Nacional de Aviação Civil

C.G. – Center of Gravity

CFRP – Carbon Fiber Reinforcement Polymer

ESL – Equivalent Single Layer

FAA - Federal Aviation Administration

FEM – Finite Element Method

MTOW – Maximum Take-Off Weight

NASTRAN - NASA Structure Analysis

NATO - North Atlantic Treaty Organization

LSS - Laminate Stacking Sequence

PSE – Primary Structure Elements

RPAS – Remotely Piloted Air System

R/C - Radio Controlled

UAV - Unmanned aircraft vehicle

UAS - Unmanned aircraft systems

WWI – First World War

WWII – Second World War

Definitions

Ground loop – a sharp, uncontrolled change of direction of the aircraft on the ground.

Taildragger aircraft – aircraft that has a main landing gear and a wheel in the tail.

Thermoset Resin – resin that cures by mean of time, pressure and temperature.

Symbols

m – Aircraft total maximum mass [kg]

d_{tire} – Tire travel [m]

d_{shock} – Shock travel [m]

d – Total shock absorber travel [m]

η_{stroke} – Shock efficiency [%]

η_{tire} – Tire efficiency [%]

η – Combined (shock + tire) efficiency [%]

ΔV – Speed variation [m/s]

n_j – Reaction/load factor on the wheels

n – Load factor

L – Lift Weight ratio

h – Drop height ratio for a drop test [m]

v_v – Vertical speed [m/s]

$E_{kinetic}$ – Kinetic energy [J]

$E_{potential}$ – Potential energy [J]

S – Aircraft wing surface Area [m^2]

d' – Distance between Nose and main landing gear considering an inclination of 14º [m]

b' – Distance between C.G. and main landing gear considering an inclination of 14º [m]

Vnose – Nose landing gear vertical loading on a level landing [N]

Dnose – Nose landing gear horizontal loading on a level landing due to spin-up forces [N]

W – Maximum weight of the aircraft at the landing instant [N]

k – Assumed drag coefficient between the wheel and the ground

$\propto$ – Angle of the combined force of Vnose and Dnose with the vertical axis that crosses the C.G. of the aircraft [º]

σ_x – Normal stress [MPa]

ε – Strain

E – Young Modulus [GPa]

G –Transverse modulus [GPa]

ν – Poisson ratio

r – Radius of the neutral surface [m]

U – Internal energy stored during strain [J]

M – Momentum [N.m]

$d\varphi$ – Angle between 2 sections of a curved beam [º]

y – Distance of a point to the neutral surface of a curved beam [m]

h1 and h2 – Distances from the neutral axis to the most remote fibers [m]

a – Inner radius of a bar [m]

c – Outer radius of a bar [m]

I_z – Second moment of area, also known as moment of inertia of a plane area [mm^4]

R – Radius of the center line [mm]

Kt – Correction stress factor

l – Length of a beam [mm]

A – Sectional Area [mm^2]

δ – Displacement of the beam along its axis [mm]

F_r – Radial Force [N]

F_θ – Tangencial Force [N]

M_b – Bending moment in a curved beam [N.m]

P – Horizontal Force [N]

Q – Vertical Force [N]

Ө – Angle [°]

φ – Angle [°]

δ_h – Horizontal deflection of a curved beam [m]

δ_v – Vertical deflection of a curved beam [m]

φ_i – Ith component of displacement or stress.

t – Time [s]

δU – Virtual strain energy [J]

δV – Virtual work [J]

δK – Virtual kinetic energy [J]

h_p – Total thickness of the plate [mm]

$Ө_k$ – Angle of orientation of a composite fiber layer [°]

Γ – Curved surface

n̂ – Normal vector

γ – Shear strain

$Q_{ij}^{(k)}$ – Plane stress-reduced stiffness

$e_{ij}^{(k)}$ – Piezoelectric moduli of the kth lamina

A_{ij} – Extensional stiffnesses

D_{ij} – Bending stiffnesses

B_{ij} – Bending-extensional coupling stiffnesses

M_{kk} – Moments applied [N.m]

N_{kk} – Normal forces applied [N]

α – Coefficients of thermal expansion [°C^{-1}]

ΔT – Temperature increment for a reference state [°C]

Z_i – Thickness considered from the middle plane to the extreme of Zth layer [mm]

$σ_Y$ – Metal yield stress [MPa]

τ – Shear stress [MPa]

X – Tensile Strength of the laminate in the direction of the fiber [MPa]

X' – Compressive Strength of the laminate in the direction of the fiber   [MPa]

Y – Tensile Strength of the laminate in the transverse direction of the fiber [MPa]

Y' – Compressive Strength of the laminate in the transverse direction of the fiber [MPa]

S – Positive shear strength [MPa]

S'– Negative shear strength [MPa]

σ_b – Bearing stress [MPa]

F_b – Compressive load [N]

A_b – Perpendicular area to F_b [mm^2]

[K] – Stiffness matrix [N/m]

{u} – Displacement vector [m]

{F} – Force vector [N]

Ψ_j – Interpolation functions

T1 – Axial stress [MPa]

T2 – Shear stress in plan 1 [MPa]

T3 – Shear stress in plan 2 [MPa]

RT – Axial Tension load ratio

RS – Shear Tension load ratio

F_{su} – Shear strength [MPa]

F_{tu} – Tension strength [MPa]

g – Gravity acceleration [m/s^2]

Figure Index

Table Index

1. Introduction

1.1. Motivation

CEiiA is a center of Engineering and product development (founded in 1999) that designs, implements and operates innovative products and systems.

The RPAS project, UAS30, is part of the aeronautical product area of CEiiA and is an aerial unmanned system designed to monitor activities with high economic or strategic value. It has 4.5 m of wingspan, a maximum take-off weight of 25 kg and an endurance of 5 h with a 72 km/h cruise speed.

The first prototype of the UAS30 had problems related to the nose landing gear – see Figure 1. When subjected to hard landings it would collapse and the nose of the aircraft would touch the ground. To solve this problem, as a temporary solution, a simple plate was welded between the beams/legs to increase the stiffness of the nose landing gear. That plate increased significantly the air drag and it should be replaced by a more aerodynamic solution. However, this was not an ideal solution and a necessity to develop a new nose landing gear was created. Therefore the main requirements for the new design were that it would be light, strong, provide great stability on the ground, easy and simple to maintain and compatible with other UAV prototypes of the same class (weight and cruise speed).

CEiiA had already probed the UAVs market and found that there were some models with composite curved leaf spring nose landing gears. With this, it was needed to find out if this was a viable solution.

Figure 1 - UAS30 first prototype - (CEiiA 2015)

1.2. Planning Method

To plan and organize all the main tasks of this work, a Gantt chart was created:

	State of the Art and Theoretical Study	Conceptual Design	Detailed Design	FEM Analysis	Test Study and Conclusions
Start date	01/06/2016	10/10/2016	12/12/2016	15/12/2016	13/01/2017
Duration	218	66	17	28	38
End date	05/01/2017	15/12/2016	29/12/2016	12/01/2017	20/02/2017
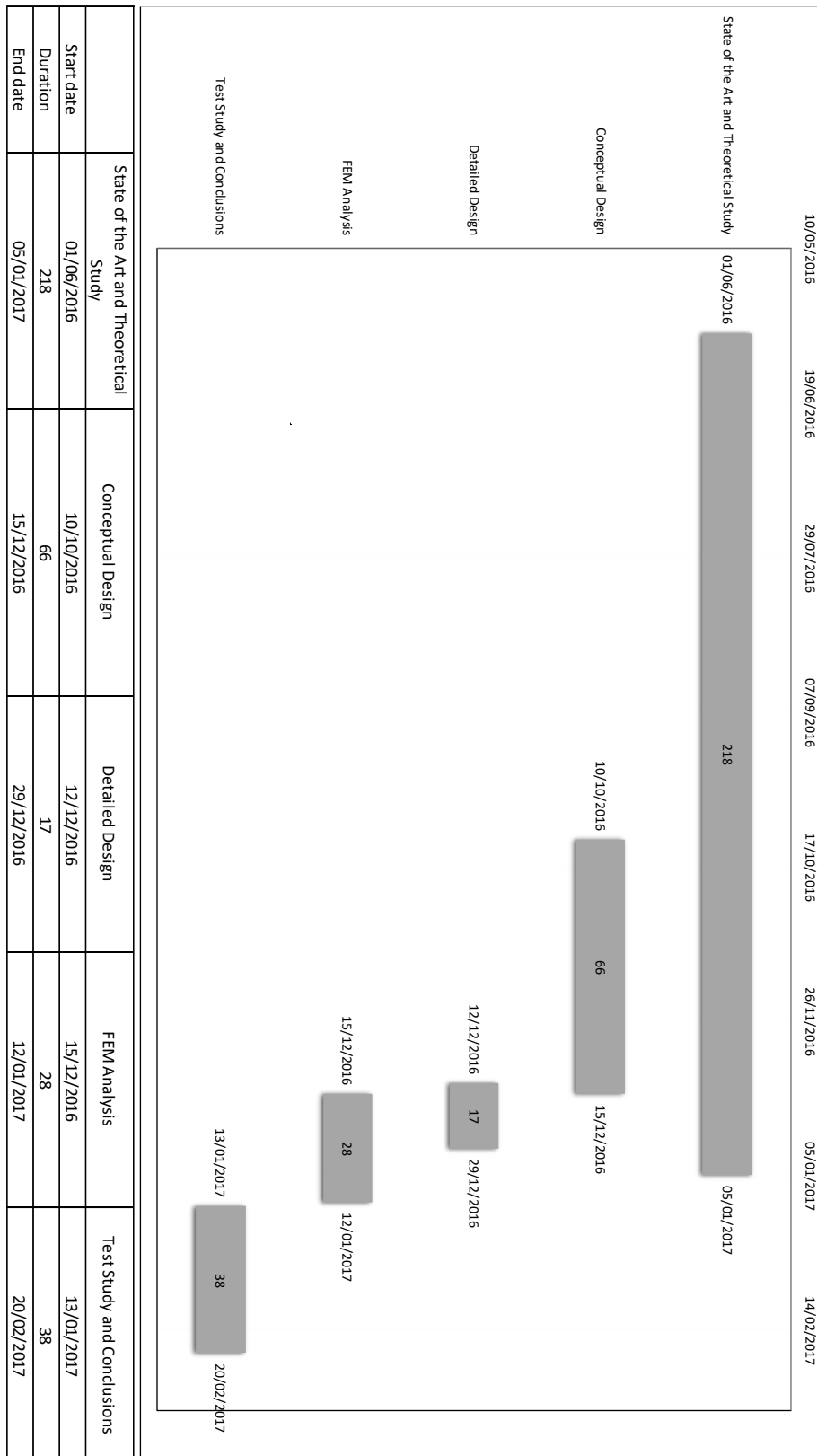
Figure 2 - GAANT chart that was used for planning the tasks

2

1.3. Thesis structure

At first, an investigation about the state of the art of the landing gear's (Landing Gear technology, Legislation and Composite materials) was done. Taking into account the requirements imposed by CEiiA and by legislations, the next step was to choose a type of landing gear. A deep study was performed, considering theoretical fundamentals (studying theoretical models of curved beams (Stress, horizontal and vertical displacement – Circular and elliptic beams), loads that the landing gear has to stand, based on actual legislation for UAV/RPAS and even correcting part of the legislation. This corrections were communicated to the responsible entities.

Then a study of design was performed (conceptual design) to find the first approach to a geometry that would lead to optimised results in terms of stress and displacements.

After validating theoretical results with FEM results and choosing the parameters (width, stack, thickness…), a more detailed design study was carried and then validated in FEM simulations. When all the results were satisfactory, a test base was designed according to the existing legislation for landing gear tests.

2. State of the Art

It is very important to take note of the technology that already exists, either in the markets either in investigation works. Obviously it is expected a better product, and if it is possible, a simpler and cheaper one.

2.1. Aircrafts landing gear history

In order to understand the evolution of technology in landing gears it's important to recall the beginning of aviation. In the following paragraphs, some examples are presented.

1- Wright Brother's Flyer

In this aircraft, the landing gear was constituted by a pair of wood sticks under the wings that would also guide the airplane in the catapult during the take off as can be checked in Figure 3.
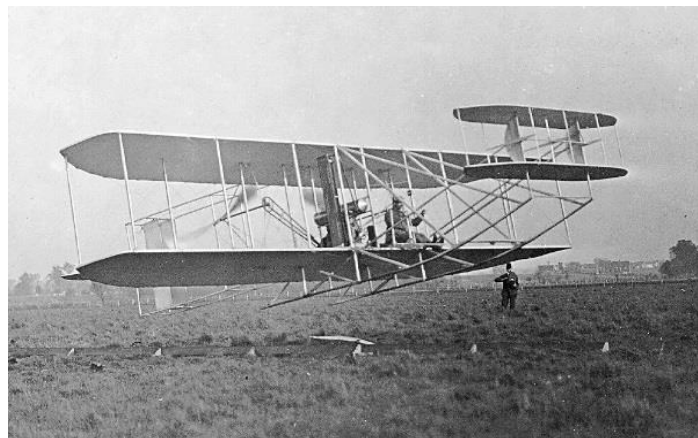
Figure 3 - Wright Brother's Flyer - (Company s.d.)

2- Sopwith Camel

This WWI aircraft had a better landing gear with wheels and wood struts, even though it had a ski in the tail acting as a non-directional tailwheel as can be checked in Figure 4.

Figure 4 - Sopwith Camel - WWI airplane - (The Aviation History Online Museum 2016)

3- P40 Warhawk

A WWII aircraft with a retractable metal landing gear. This gear had an oleo-pneumatic cylinder acting as a shock absorber and also hydraulic brakes as can be checked in Figure 5.
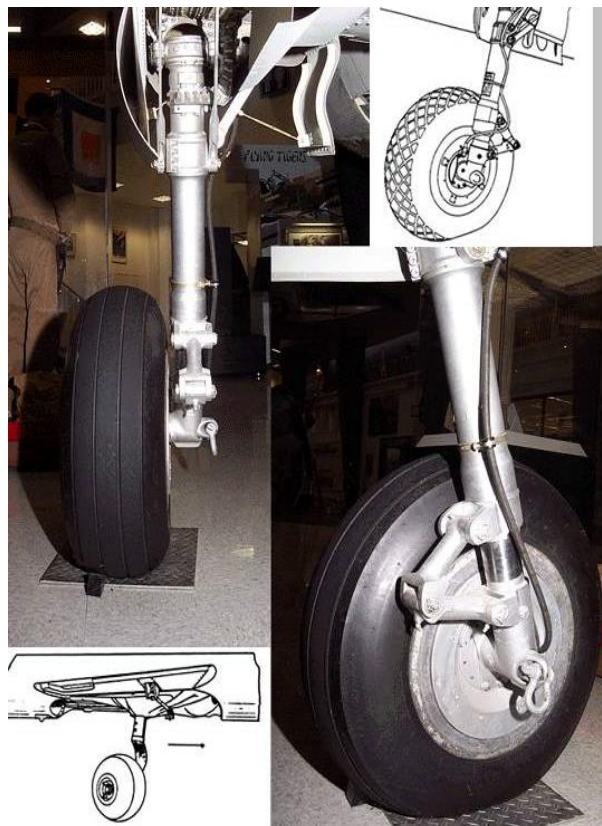
Figure 5 - P40's Landing Gear - WW2 aircraft - (Hagen 2002)

4- New Era's commercial light aircraft landing gears

Considering light aircrafts as a non-airliner and military, these light landing gears are commonly made with composite materials such glass fiber or carbon fiber composite with epoxy resins. Comparing to the old Sopwith, these composite struts act with some of the same principles, notwithstanding the fact that they can reach a lot higher stresses thanks to the material and the curvature of the glass fiber composite landing gear that acts as a shock absorber. An example of these type of landing gear can be checked in Figure 6.

Figure 6 - Light Aircraft glass fiber composite main landing gear - (C. Composites s.d.)

5- Military UAV aircraft landing gears

The Reaper's landing gear is a little more complex, having for example, a shimmy-dumper on the nose landing gear. It's built with carbon fiber composite, in order to have the best performance in terms of stress and also to maintain a light weight. An example can be seen in Figure 7.

Figure 7- MQ9 Reaper UAV Landing gear close up - (Fiber Dynamics s.d.)

2.2. Types of landing gears

There is an enormous variety of landing gears for both fixed and rotor wing aircrafts. Figure 8 presents different type of landing gears that are frequently used.
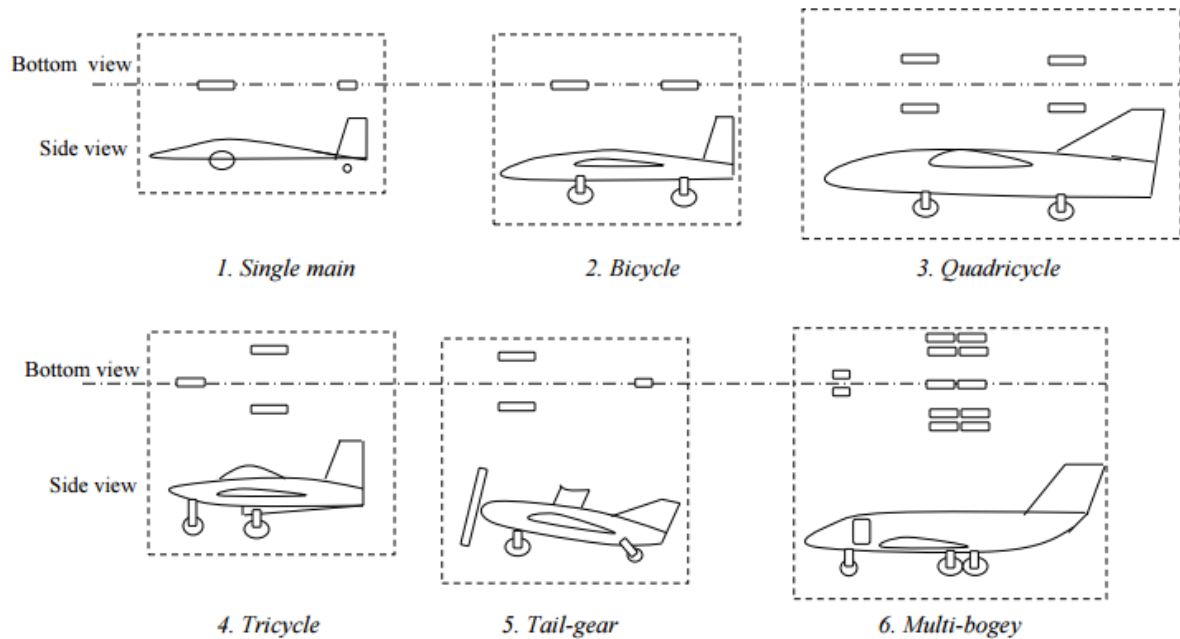
Figure 8 - Different types of landing gears for fixed wing aircraft - (Sadraey 2012)

The UAS30 P1aircraft has a fixed tricycle landing gear.

According to (TECHNOLOGY 2014) and (GUDMUNDSSON 2014) the main advantages of this type of landing gear and the main reasons why this type is used in most of the fixed wing aircraft are:

•   Enables a greater ground stability than tailwheel aircrafts, during taxi, take-off and landing, allowing abrupt braking.

•   It prevents ground loops.

•   Good ground control in cross-wind.

•   Propeller is better protected from ground strike.

•   Airplane pitches nose-down upon main gear touch-down, reducing lift.

•   Easier to land, therefore, is more forgiving for new and inexperienced pilots.

Furthermore the main disadvantages according to the same reference (GUDMUNDSSON 2014) are:

•   Requires minimum speed for rotation (usually it can't turn while the airplane is stopped).

•   Usually they have higher prices than tail draggers because it has a more complex steering mechanism.

•   Higher in-flight drag.

•   Can have nose gear shimming – a vibration that occurs during landing or taking-off and that can damage the nose landing gear.

•   Higher dynamic load than tail dragger application's.

•   Lower angle of attack after touch down, requiring more brake effort (when brakes can be applied).

Tail draggers aircrafts have a less complex landing gear than nose gear aircrafts - Figure 9 and Figure 10 present examples of this type of landing gear. And typically they have a reduced number of parts when comparing to nose gear aircrafts.

Figure 9 - Example of a taildragger aircraft - (Aero 2010)

Figure 10 - Example of a nose landing gear aircraft - (Club s.d.)

2.2.1. Retractable vs Non-Retractable landing gear

In order to obtain better performance in terms of aerodynamics, we should opt for a retractable landing gear. However, in this type of models it is not the best option because the main objective is to reduce weight so that it is possible to increase the cargo capacity. Retractable gears would occupy a considerable space of the fuselage that is usually used for electronic and other equipment. And it would also increase the weight of the aircraft when comparing to a fixed landing gear.

Finally, it is crucial to take note that retractable landing gears are more likely to fail than fixed ones, which is a very important issue since this type of aircraft (RPAS) usually carry high cost and sensible equipment such as high-technology infrared and thermographic cameras at the aircraft payload bay (belly – under the fuselage).

2.2.2. UAVs Typical landing gears

In the UAV's field it is possible to witness two very distinct options when referring to nose landing gears:

•   Metallic Landing Gears

•   Composite Landing Gears

In metallic nose landing gears, generally it's used a cylinder type or spring type landing gear.

Within Composite landing gears type it is also possible to observe two subtypes of landing gears: Spring curved leaf type and rigid strut. The rigid strut is used in quite heavy work like a RQ9 UAV (see Figure 16).

These facts can be verified in the following pictures with a considerably variety of UAVs.

Figure 11 - Mugin 4.5 meters UAV - (FPV Mmodel 2015)

As can be observed in Figure 11, this is a model with a similar size of the UAS30 P1 and it uses a composite leaf spring type nose landing gear.

Figure 12 - Penguin UAV - (UAV Factory s.d.)

Figure 12 presents Penguin, also a similar model to UAS30 P1. However, the landing gear is a metallic cylinder type.

Figure 13 - TAI Anka UAV - (Network 54 2010)

As for TAI Anka presented in Figure 13, this is a medium size Turkish UAV with a MTOW of 1600 kg and it's using a metal with spring type nose landing gear.

Figure 14 - SATUMA Flamingo - (Satuma s.d.)

Figure 14 presents Flamingo, a small-medium private UAV with a MTOW of 30/35 kg. Which is a little heavier than UAS30 P1. It uses a leaf spring type composite non-retractable landing gear.

Figure 15 - Pegasus UAV - (BB composite s.d.)

Regarding, the Pegasus UAV seen in Figure 15 was designed for Serbian military and it's in the medium-heavy category with a MTOW of 220 kg. It uses a cylinder metal type landing gear.

Figure 16 - MQ9 Reaper aircraft with a composite landing gear - (Fiber Dynamics s.d.)

MQ9 Reaper (see Figure 16) is one of the most known military heavy UAVs in the world with a MTOW of 4760 kg. It uses a rigid composite landing gear and it includes also a torque arm, due to the big size of the model.

Figure 17 - RQ2 Aircraft - (Fast Aviation Data s.d.)

Figure 17 presents RQ 2, a medium-heavy UAV with a MTOW of 205 kg. It has a leaf spring composite type landing gear.

Figure 18 - Elimco UAV E500 - (Elimco s.d.)

Finally, Elimco E500 presented in Figure 18 is a Spanish small-medium UAV with a maximum payload of 10 kg and a MTOW of 50 kg. It has also a leaf spring composite type landing gear.

2.2.3. Composite vs hydraulic landing Gear vs aluminium tube - landing gear

There are more types of landing gear than those mentioned before, such as bungee cord absorption type, but the types presented are the most used for the nose landing gear.

Oleo-Pneumatic landing gears (such as the one presented in Figure 19) are very effective in absorbing energy on the landing impact protecting the aircraft structure and also controlling the rebound. However, as (THOMPSON 2014) affirms, these type of shock absorbers are expensive and have some problems that might include oil or gas leakage, seal wear, temperature effects, corrosion, friction and a higher degree of complexity of maintenance.
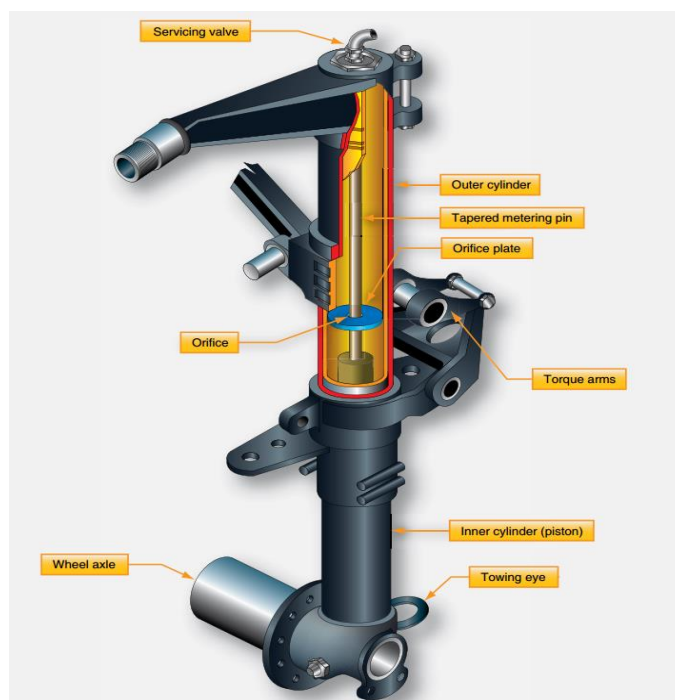
Figure 19 - Oleo-Pneumatic Landing gear leg - (FAA - Federal Aviation Administration s.d.)

As for the shimmy dumper and torque link types: the torque links align the landing gear and maintain the piston in the upper cylinder when strut is extended.

Shimmy is a vibration that occurs at a certain speed of the airplane on the ground. A shimmy damper is a small hydraulic device that helps controlling oscillations of nose landing gear (see Figure 20).

Shimmy of landing gears is potentially dangerous and may result in severe damages. This device is active during all the ground operations and permits the nose gear steering system to function normally.

Experience has shown that it is difficult to reliably demonstrate shimmy stability from laboratory tests.

Figure 20 - Shimmy damper device - Oleo-Pneumatic Landing gear leg - (FAA - Federal Aviation Administration s.d.)

Landing gears made out of composite materials entirely (leaf spring type) don't have shock absorber. The gear itself absorbs all the loads. On the other side, rigid composite struts need a shock absorber, such as the Varieze Aircraft.

2.2.4. Comparison of manned aircraft landing gear and R/C model aircraft

It's quite important to acknowledge the existent technology in both domains: R/C model and manned aircraft.

Even though R/C aircraft models might suggest a simple solution, it's possible to find very interesting ones such as presented in the following paragraphs.

1. Fults landing gear

Similar to the current UAS30 P1 landing gear these commercial landing gears are designed to a MTOW of 5 kg (see Figure 21 and Figure 22).

Figure 21 - R/C model landing gear (Fults type) - (Gear 2001-2015)
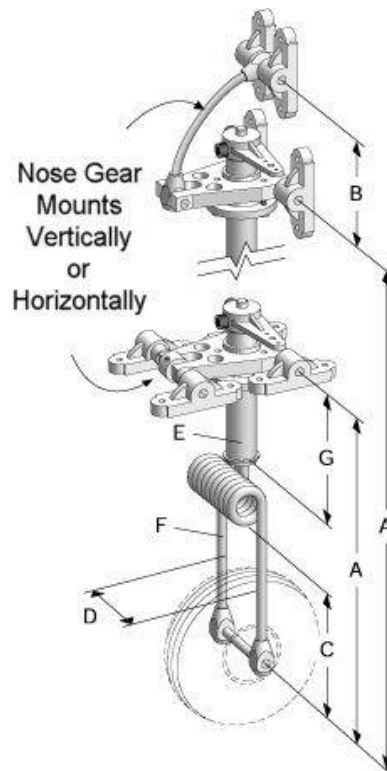
Figure 22 - R/C model landing gear (Fults type scheme) - (Gear 2001-2015)

2. Golden Skies Landing gear

This is another metal landing gear designed for a MTOW of 7.5 kg (see Figure 23).

Figure 23 - Golden Skies Landing gear - (Aircraft s.d.)

3. Sierra Giant

These landing gears are designed for a 55 kg aircraft model (see Figure 24).

Figure 24 - Sierra Giant Landing gear - (Giant 2008)

It was not possible to find a commercial composite nose landing gear solution to be sold separately as landing gear set (wheels and strut).

The following paragraphs present ultralight aircraft and gliders/motor-gliders landing gears in order to compare technologies that are used in both R/C and manned aircrafts.

1- Landing gear of the American ultralight aircraft Challenger 40 - This aircraft has a MTOW of 435 kg.
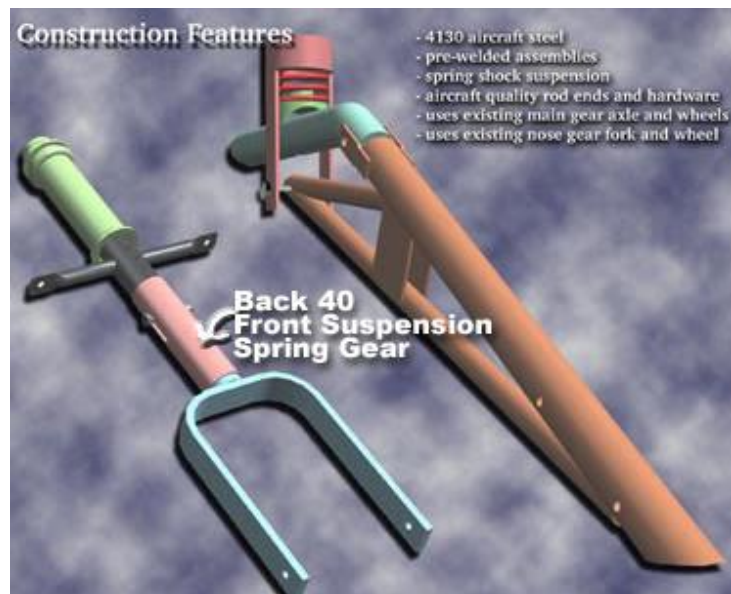
Figure 25 - Challenger 40 Ultralight Landing Gear - (Flite s.d.)

2- Landing gear made of steel tube, from a Diamond Tundra Star aircraft. This landing gear is ready for landing in rough conditions and a MTOW of 1280 kg.

Figure 26 - Diamond Tundra Star DA-40 - (Airliners 2000)

3- Composite landing gear, used in a Varieze aircraft. This is a retractable nose landing gear, with a composite strut: hard wood core and 3 layers of S-glass fiber.

Figure 27 - Construction of a composite Landing Gear strut of a Varieze type aircraft - (Wade s.d.)

Figure 28 - Finished nose landing gear of a Varieze Aircraft - (Pilot Planes s.d.)

Pros & Cons:

In the following table is possible to analyse pros and cons of type of landing gear:

Table 1 - Pros and Cons of most used UAV landing gear types

Type	Metal & Oleo-Pneumatic Cylinder	Metal & Spring	Composite & Leaf Spring	Composite & rigid strut
Pros	Easy to design	Easy to design	Lighter than metal gear Fatigue resistance Allow for complex designs	Lighter than metal landing gear
Cons	Inspection of oil Oil Leaks Usually heavier than composite struts	Need of changing the spring Usually heavier than composite struts leaks	Incompatibility of carbon and some metals (galvanic corrosion)[1] Difficult to do precise calculations	Incompatibility of carbon and some metals(galvanic corrosion) Need of a shock absorber More expensive than metal landing gear

2.2.5. *Geometries of nose landing gears*

With the type of landing gear chosen, it is possible to design some different shapes/geometries on the nose landing gear. These different geometries will be analysed in chapter 3.
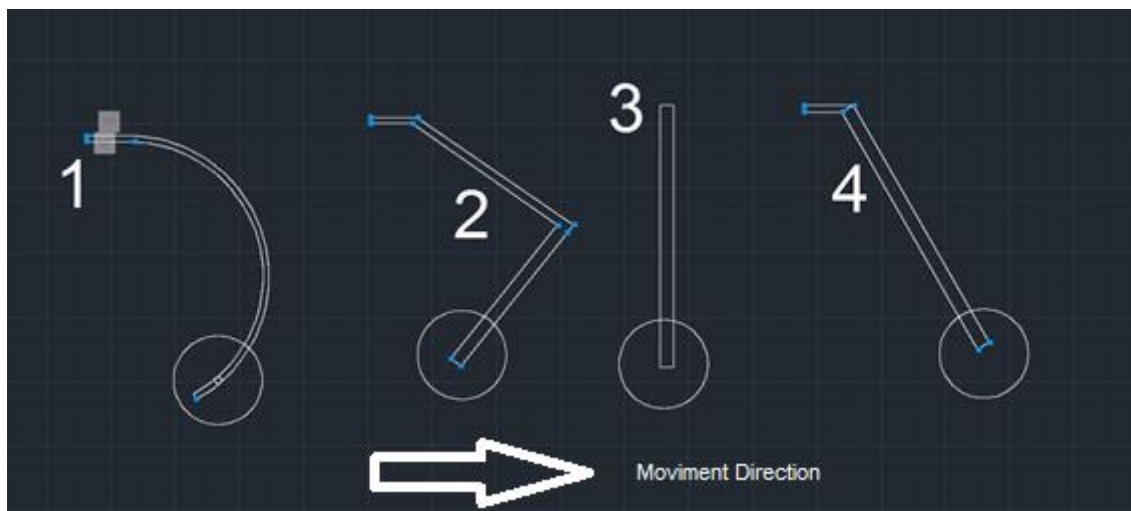
Figure 29 - Examples of nose landing gears shapes

---

[1] See chapter Metals and carbon fiber compatibility - *2.5.1*

2.3. Patents

Patents were studied in order to find how the technology of landing gears state-of-the-art.

An interesting solution was found for UAVs/RPAs in reference (WESTMAN 2012), see Figure 30. It's a new technique to attach a typical landing gears to the composite parts of the aircraft in order to distribute landing loads, including out-of-plane loads so that the landing gear and it's mounting to the aircraft (that is robust) can withstand variable landing loads. Composites don't work well with out-of-plane loads as there is a high probability to occur delamination. The main idea is to install two shock absorbers that will withstand those type of loads.
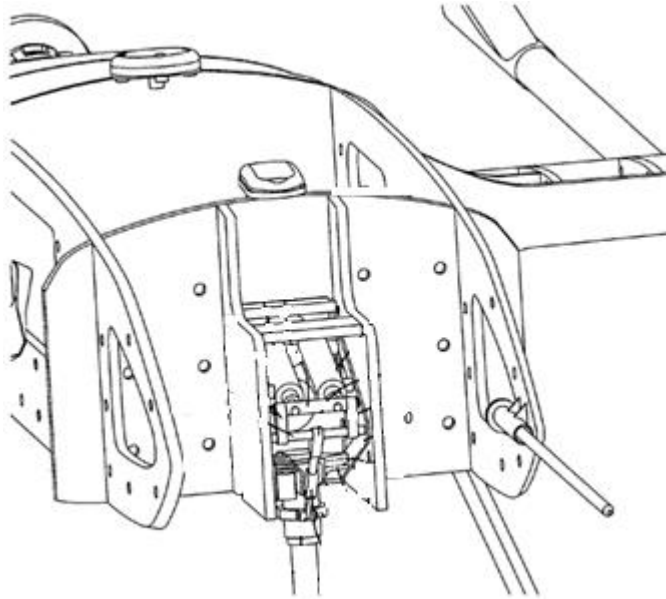
Figure 30 - 3D drawing of the invention - (Westman 2012)

Unfortunately, the second prototype of the UAS 30 was already designed and is currently in production, so there was not a possibility to provide space to install those shock absorbers.

Another very interesting concept was found in (THOMPSON 2014). It is a mixture of a shock absorber with a composite leaf spring.

It has a stiff and fixed arm, a composite leaf spring and a shock absorber so that the load is transferred directly into the pivot without a large amount of bending of the leg.

A curious advantage is that the leaf spring shock absorber typically has a reduced number of parts compared with a conventional oleo pneumatic shock absorber. By forming the leaf spring from a composite material, its weight is significantly reduced in comparison with a conventional metal spring, making it suit able for use on a relatively large aircraft.
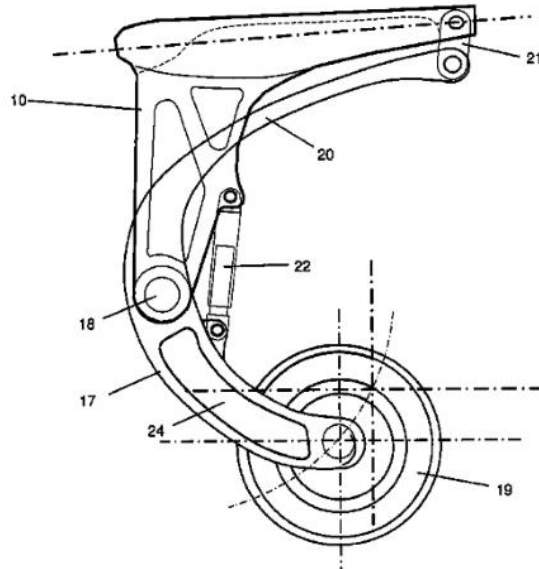
Figure 31 - 2D drawing of the landing gear invention - (Thompson 2014)

This hybrid construction is more adequate to main landing gears, that's why it was not considered to the nose landing gear as usually the nose landing gear doesn't have to withstand with such high loads.

2.4. UAVs Legislation

NATO has been working on a special legislation for unnamed aircraft: STANAG 4703/NATO AEP83 (NATO 2014).

This legislation is an adaption of the existent legislation for manned aircrafts (such as CS-VLA (very light airplanes) and FAA FAR 23 (Airworthiness Standards: Normal, Utility, Acrobatic and Commuter Category Airplanes)) to UAVs/RPAs. It's important to consider that NATO doesn't certify aircrafts. This procedure is performed by the national entity of each country (this entity in Portugal is ANAC and at the moment there is no active legislation in Portugal).

Thus, the legislations for manned aircrafts mentioned in the paragraph above were also considered in this master thesis (NATO 2014), (EASA 2009), (FAA - Federal Aviation Administration s.d.).

In terms of structural requirements, when referring to landing gears, it was found that the results between those legislations were quite similar. Requirements imposed by those legislations were considered during the design of the landing gear.

2.4.1. STANAG 4703 / NATO AEP83

Regarding the **loads applied to the landing gear**, this structure is considered a PSE (primary structure element) and according to this legislation, all maximum operational loads that the PSEs must withstand on the ground must be identified, considering external forces in equilibrium with inertial forces.

When designing the landing gear, it must be considered that the landing impact is at the maximum design weight (this is also what FAR 23 recommends).

Furthermore, bearing in mind the specific design usage, the worst combination of loads corresponding to all the possible scenarios of impact in the landing moment must be determined. The worst scenario for the nose landing gear occurs when the nose and main wheels contact the ground simultaneously (also considered in FAR 23 and CS-VLA) – these loads will be discussed in detail in chapter *3.1.1.1 Loads applied to nose landing gears*.

Moreover, the structure should not have detrimental deformation against the limit loads (maximum load that an aircraft is expected to handle during its service life (BATCHU S.D.)) obtained by multiplying the maximum operational loads by the limit load factors of safety. Also, there should be no rupture against the ultimate loads ((loads that could occur during unexpected event such as: severe gust load in a storm or an emergency landing or crash condition (BATCHU S.D.).). Since a landing gear is considered a PSE (primary structure element), an ultimate load factor of safety ≥1.5 should be used to determine the ultimate loads as the maximum operational loads multiplied by this factor (AVIATION GLOSSARY 2012).

As for the **material allowables**, they must be identified so that no structural part is under strength as a result of material variations or load concentration. The sources for material allowables determination must be declared and agreed by the Certifying Authority. Also, it's necessary to classify the material allowables that will be used for calculations (A or B allowable) – this issue will be discussed later, in chapter *3.1 Landing Gear Design Approach* and, when temperature and moisture have quite significance in typical operations, the allowable design values are considered in the worst conditions,

Finally, **instructions for continued airworthiness** for the UAS must be provided (which must include the information essential to the continued airworthiness of the UAS). This part might be consulted in chapter 2.5.4.

2.4.2. FAR 23

Since FAR23 presents a similar legislation to STANAG, only some special features will be recognized.

Regarding the **ground load conditions and assumptions,** the inertia load factor used for design purposes must be higher than 2.67, and the limit ground reaction load factor be higher than 2.0 at design maximum weight (unless these lower values will not be exceeded in taxiing at speeds up to take-off speed over terrain as rough as that expected in service.)

As for the **limit drop tests,** if drop tests are performed, these tests must be made on the complete airplane, or on units consisting of wheel, tire, and shock absorber, in their proper relation. Limit inertia load factor must be found in a rational/conservative manner using a landing gear attitude that represents the landing conditions.

2.4.3. CS-VLA

Again there are a lot of similarities of CS-VLA and FAR23 and STANAG legislations, thus, only some special features will be presented.

As for **strength and deformation,** the structure must be able to support ultimate loads without failure for at least 3 seconds. A drag component of not less than 25% of the maximum vertical ground reactions (neglecting wing lift) must be properly combined with the vertical reactions.

Regarding the **shock absorption tests,** it must be shown that the limit load factors selected for design in accordance will not be exceeded. And the landing gear may not fail, but may yield, in a test showing its reserved energy absorption capacity, simulating a descent velocity of 1.2 times the limit descent velocity, assuming wing lift equal to the weight of the aeroplane.

2.5. Manufacture

Manufacture process selection is usually made on the basis of lowest cost, which will produce the part to meet the specified requirements:

- Production rate
- Quality

2.5.1. Metals and carbon fiber compatibility

Galvanic corrosion is a common issue of metal-composite joints such as in plain steel or aluminium coupled with carbon fiber. In this work these types of joints exist and must be considered.

These type of corrosion is less evident in stainless steel (but it might exist in terms of localized corrosion (pitting and crevice) which is quite dangerous). An ideal metal to use with carbon-fiber is titanium but the price turns it out not suitable for the function of the nose landing gear of a small UAV/RPAS.

Corrosion is not just dangerous for the metal parts but also for the composite ones. Due to hydrogen gas evolution in defects sites of the composite (cracks or voids), hydrogen-filled blisters can be formed on the composite surface like it is shown in the next figure:
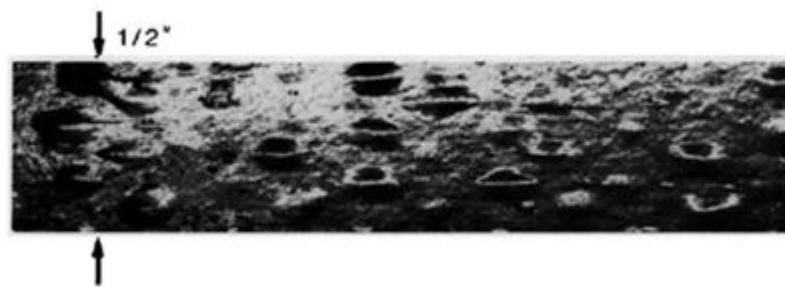
Figure 32 - Corrosion in carbon fiber - (Yari s.d.)

Some solutions can be presented for all these problems:

- Insulating electrically the joint between Metal and Composite, using for example glass fiber.
- Using epoxy resins without hydrolysable linkage (such as ester bonds) to mitigate water penetration into composite and then to decrease the real cathodic surface area (YARI S.D.).

2.5.2. Manufacture technologies – Composite parts

To manufacture this landing gear, metallic mould and vacuum bagging technology were used.

Vacuum bagging technique creates mechanical pressure along all the laminate during cure cycle. This technique can be checked in figure 33. It helps removing trapped air between the layers, it compacts the fiber layers for a good force transmission among fiber bundles but also prevents shifting of fiber orientation during cure process. It reduces humidity and most important, optimizes fiber-to-resin ratio in the composite part.

Besides these facts, vacuum bagging is not an expensive technology which makes it perfect for standard ends. (The expensive part is the mould tooling)

Fiber-to-resin is a very important parameter to get the best properties of a composite. Fibers in textile state are not particularly strong (except in the direction of the fibers). Resins (as for example epoxy or polyester polyester unsaturated) are brittle if cured without reinforcement (fibers).

So it's important that there is not excess of resin in the laminate (otherwise the laminate will behave more like a resin) but also cannot have lack of it (places where reinforcement is dry are weak spots). There is not a simple recipe to know which is the best value for fiber-to-resin ratio, each case is a complex engineering problem (usually 60% is a good target).

These vacuum systems are complex and require a good knowledge to operate them and to obtain good results.
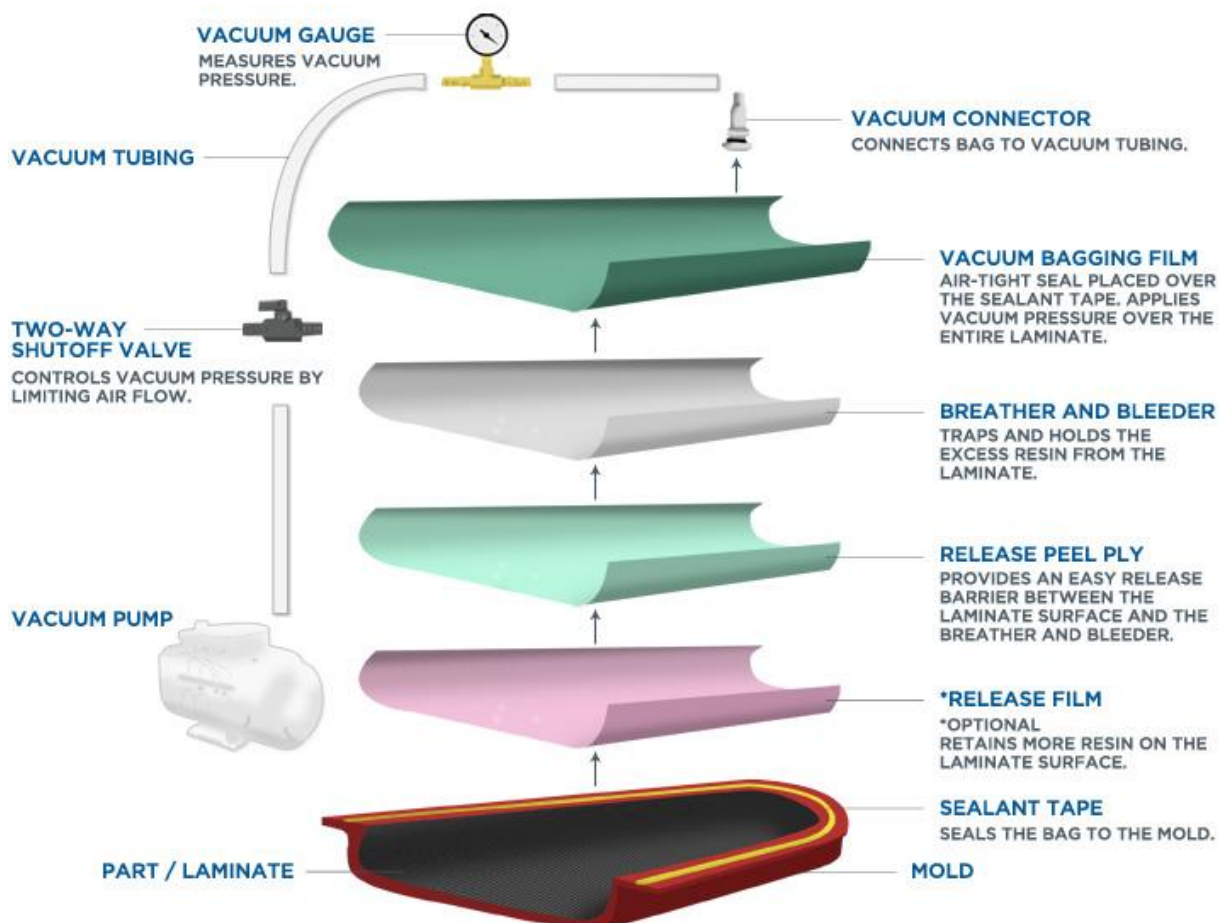
Figure 33 - Vacuum bagging system - (Net Composites s.d.)

Release film (Peel Ply)

The first layer that goes between the uncured laminate and subsequent bleeder/breather layers is the release film. It can be porous or not porous, depending on the resin bleed that is required. It usually extends beyond the edge of the layup and can be sealed/secured with tape (N. COMPOSITES 2017).

Bleeder layer

It is used for resin absorption from the laminate. It's a non-woven synthetic fiber material with different thicknesses. Bleeder layers can be combined in multiple layers for heavy resin bleed requirements. This layer also extends beyond the edge of the layup and is secured with tape.

Separator film layer

This layer is used between the bleeder and breather layer to restrict/prevent resin flow. Might be a solid or perforated release film that extends to the edge of the layup but stops inside the edge of the bleeder layer in order to allow gas to flow to the vacuum ports.

Breather layer

Used to maintain a breather path throughout the bag to the vacuum source so that air can escape and then continuous pressure might be applied to the laminate. Usually synthetic fibers or heavy fiberglass fabric is used for this situation.

Breather layer extends past the edges of the layout so that the edge-band makes contact with the bleeder ply around the separator film. Vacuum ports are connected to the breather layer directly or with strips.

Bag film

Bag film is the vacuum membrane that is sealed at the edges to the mold surface (or to itself in case of an envelope bag). The bag film usually is much larger than the area being bagged (because of typical folds at all of inside corners and about the periphery of the bag). Usually are made of Nylon, Kapton or polyvinyl alcohol materials.

2.5.3. Manufacture technologies – Metallic parts

To manufacture metallic parts (steel and aluminium) a CNC mill machine should be used for the upper plate and fork, CNC water jet cutting machine for the down plate. Round axle parts should be manufactured with a lathe.

2.5.4. Continuous airworthiness maintenance program

As prescribed in UL37.2 of (NATO 2014), a continuous airworthiness maintenance program must be presented.

UAS repair and replace instructions:

In case that:

- Tires should be inspected frequently for cuts, worn spots, bulges on the side walls, foreign bodies in the treads – If the tire is not in good conditions it must be substituted for a new one.

- Cracks were found in the leaf spring after a hard landing – Substitute for a new leaf spring.

- A metallic part was found deformed – if it is possible: Rectify the deformed metallic part, if not, substitute for a new one.

- Any broken metallic part must be substituted by a new one.

The setup: Wheel + landing gear must be cleaned after each flight in order to remove dust and other particles that might interfere with the operation of those parts.

For cleaning: neutral solutions must be used to ensure that no corrosive occurs due to the cleaning process.

Wear points, bushes, servo arm connector and wheel axle and its connecting parts must be lubricated after each cleaning process.

Prior each flight all bolts, pins and fittings should be checked for security and condition (FAA 2001).

After every maintenance or cleaning it must be ensured that wheel should roll freely and no vibrations were found during the roll of the wheel. (To ensure that the axle of the wheel is not deformed).

For each 50 flight hours, or considerable hard landing, the landing gear must be dismantled and checked for any cracks or deformation in each part.

Typical bolt cracks can be observed in Figure 34.Figure 35
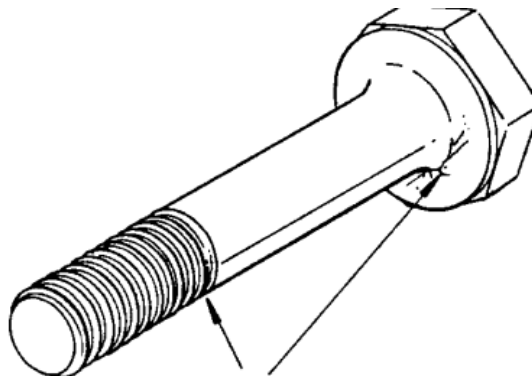
Figure 34 - Typical bolt cracks - (FAA 2001)

Typical cracks in landing gear fittings can be observed in Figure 35:
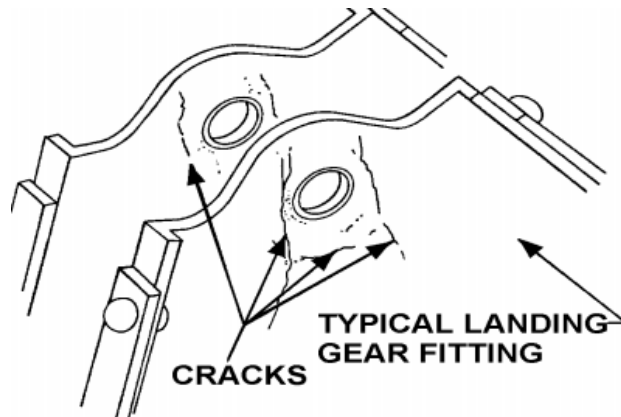
Figure 35 - Typical Cracks in landing gear fittings - (FAA 2001)

Another point that must be checked is the servo arm connector. Typically these types of parts generate cracks in the ends of the threaded parts, as can be seen in Figure 36.
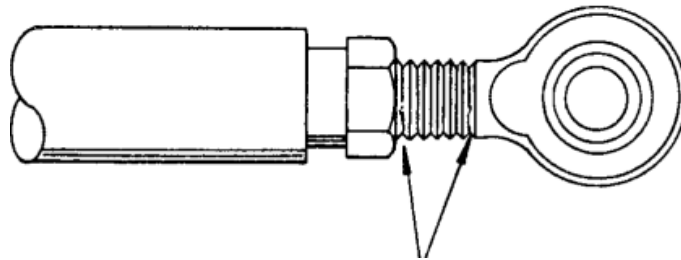
Figure 36 - Typical cracks in rod-end parts - (FAA 2001)

3. Theoretical Principles: Designing the front landing gear

3.1. Landing Gear Design Approach

The landing gear's purpose in an aircraft is to provide a suspension system during landing, take-off and taxi. It's designed to absorb shock and dynamic solicitations and therefore to reduce impact loads transmitted to the airframe.

It's important to remember that it was assumed initially that the nose landing gear would be (probably) a composite leaf spring.

Designing landing gears is an iterative process. The next scheme represents the approach that was decided to follow during this work:

```
                    ┌────────────────────────────────────┐
                    │   Identify landing gear requirements │
                    └────────────────────────────────────┘
                                      │
  ┌───────────────────────────────────────────────────────────────────────┐
  │ Conceptual                       ▼                                     │
  │ Design          ┌────────────────────────────────────┐                │
  │                 │   Select configurations and geometry │                │
  │                 └────────────────────────────────────┘                │
  │                                  │                                     │
  │                                  ▼                                     │
  │                 ┌────────────────────────────────────┐                │
  │                 │  Define geometry parameters and stacking │◄──────┐   │
  │                 └────────────────────────────────────┘        Failed │   │
  │                                  │                                   │   │
  │                                  ▼                                   │   │
  │                 ┌────────────────────────────────────┐              │   │
  │                 │          Preliminary FEM            ├──────────────┘   │
  │                 └────────────────────────────────────┘                  │
  └───────────────────────────────────────────────────────────────────────┘
                                     │  Sucessful
                                     ▼
  ┌───────────────────────────────────────────────────────────────────────┐
  │ Detailed        ┌────────────────────────────────────┐                │
  │ Design          │ Design of mechanical components to connect │◄─────┐  │
  │                 │      to wheels and aircraft          │      Failed │  │
  │                 └────────────────────────────────────┘             │  │
  │                                  │                                  │  │
  │              ┌───────────►       ▼                                  │  │
  │              │       ┌────────────────────┐                        │  │
  │              │       │     FEM tests       ├────────────────────────┘  │
  │              │       └────────────────────┘                           │
  └──────────────┼────────────────────────────────────────────────────────┘
           Failed │                  │  Sucessful
                  │                  ▼
                  │       ┌────────────────────┐
                  └───────┤     Drop-Test       │
                          └────────────────────┘
                                     │  Sucessful
                                     ▼
                 ┌────────────────────────────────────────┐
                 │ Correlation between numerical model (FEM) and test │
                 └────────────────────────────────────────┘
```
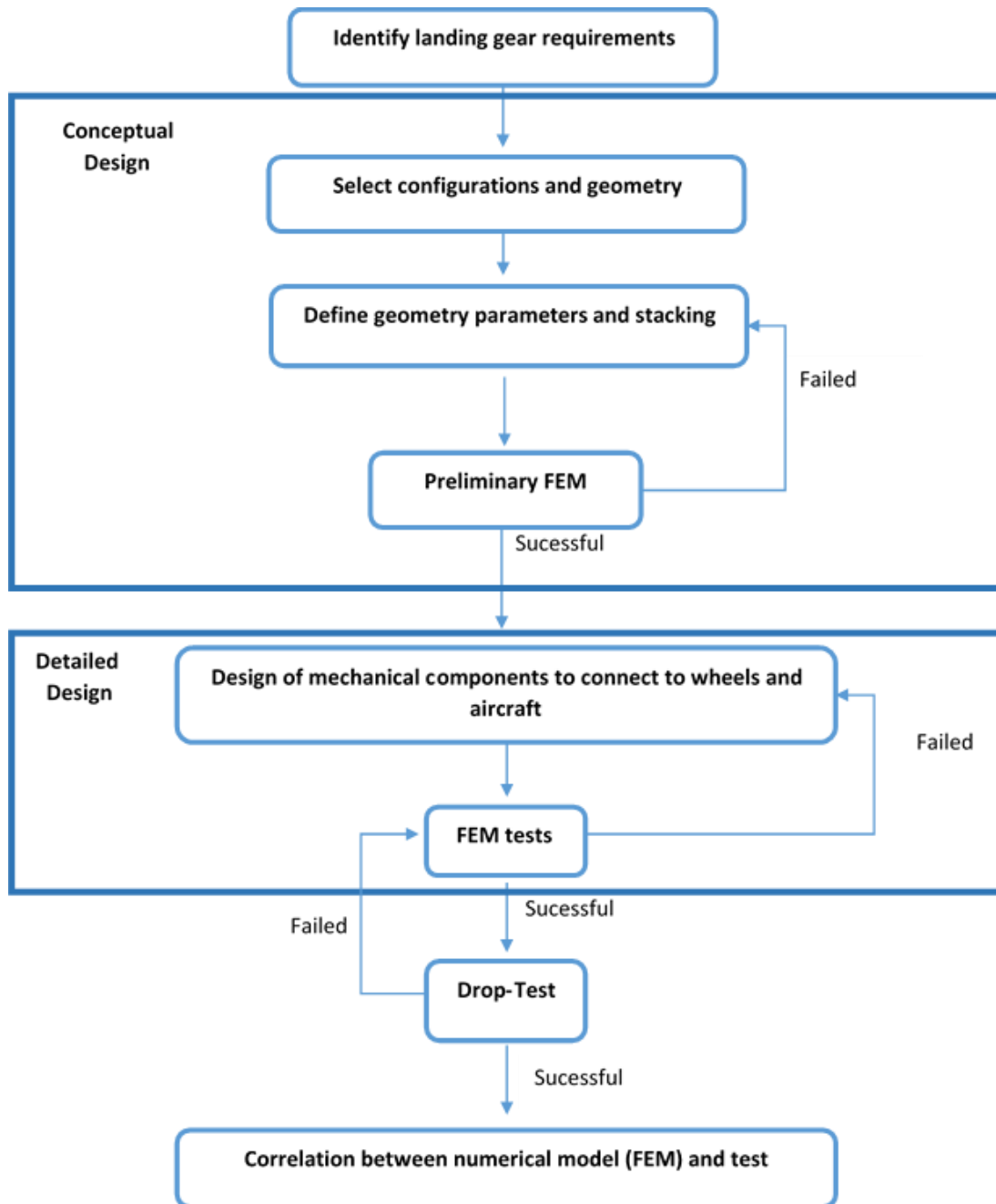
3.1.1. Identification of Landing Gear requirements

3.1.1.1 Loads applied to nose landing gears

As presented in chapter 2.4.1 STANAG 4703 / NATO AEP83, the most critical situation for the nose landing gear is at level landing condition with inclined reactions. In this case the aircraft performs a 3 point landing, which means that all the landing gears wheels hit the ground at the same moment.

According to (Currey 1988), the conservation law at the moment of impact:

$$E_{kinetic} + E_{potential} = E_{tire} + E_{Stroke}(=) \qquad (1)$$

$$(=)\frac{m(\Delta v)^2}{2} + (\text{mg} - \text{L m g}) \times (d_{stroke} + d_{tire}) = d_{tire}\, \eta_{tire}\, n_j\, m\, g + d_{stroke}\, \eta_{stroke}\, n_j\, m\, g \quad (2)$$

It was assumed while performing calculations that the composite leaf spring has a shock absorber behavior.

Where:

- $E_{kinetic}$ is the kinetic energy [J]
- $E_{potential}$ is the potential energy [J]
- $g = 9,81$ is the gravitational acceleration [m/s^2]
- d_{tire} – tire travel [m]
- d_{shock} – shock travel [m]
- $d = d_{shock} + d_{tire}$ – total shock absorber travel [m]
- η_{stroke} – shock efficiency [%]
- η_{tire} – Tire efficiency [%]
- m – Aircraft total maximum mass [kg]
- ΔV – Speed variation at impact [m/s]
- n_j – Reaction factor (load factor)
- L – Lift Weight ratio [L = 2/3] - ratio of assumed lift to the aircraft weight – "Wing lift not exceeding two-thirds of the weight of the airplane may be assumed to exist throughout the landing impact and to act through the center of gravity." (ADMINISTRATION 1967).

Considering a simple drop test to simulate a landing condition, $E_{kinetic} = E_{potential}$

$$\frac{1}{2}\, mv^2 = mg\, h(=)$$

$$(=)\ h = \frac{v^2}{2g}\ (=)\ \text{v} = \sqrt{2\, h\, g} \qquad (3)$$

Where h is the drop height ratio [m] for a drop test.

Replacing equation 3 in equation 2:

$$\frac{m\left(\sqrt{2hg}\right)^2}{2} + (mg - L\,m\,g) \times d = d\,\eta\,n_j\,m\,g \tag{4}$$

$$(=)\, h + (1 - L) \times d = d\,\eta\,n_j \tag{5}$$

$$(=)\, n_j = \frac{h + \dfrac{d}{3}}{\eta \times d} \tag{6}$$

Where:

- η – tire efficiency assumed equal to shock absorber efficiency [%], where $\eta = \eta_{tire} = \eta_{shock} = 0,5$ according to (NATO 2014)

A level landing example can be checked in Figure 37.
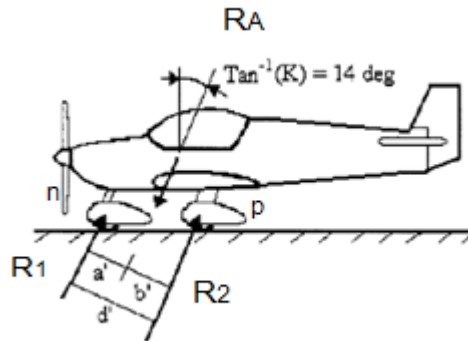
Figure 37 - Level landing with inclined reactions - (NATO 2014)

Initially it is necessary to assume that all the relations between F_x and F_y forces is given by:

$$F_x = k\,F_y \quad [N] \tag{7}$$

Where:

- $K = 0.25$ - is the assumed drag coefficient between the wheel and the ground.
- F_x represents all the horizontal force components existing in figure 37
- F_y represents all the vertical force components existing in figure 37

Considering that at the landing impact, the sum of all the forces involved in figure 37 and the moments on the nose landing gear (M_n) and main landing gear (M_p) are zero:

$$\begin{cases} \sum F = 0 \\ \sum M_n = 0 \\ \sum M_p = 0 \end{cases} \qquad (8)$$

Where:

- M_n − Moments on the nose landing gear
- M_p − Moments on the main landing gear

$$(=) \begin{cases} R_1 + R_2 - F_A = 0 \\ R_2 d' - R_A a' = 0 \\ -R_1 d' + R_A b' = 0 \end{cases} \qquad (9)$$

$$(=) \begin{cases} R_1 + R_2 = F_A \\ R_2 = F_A \dfrac{a'}{d'} \\ R_1 = F_A \dfrac{b'}{d'} \end{cases} \qquad (10)$$

Where:

- R_1 – is the reaction on the nose landing gear [N]
- R_2 – is the reaction on the main landing gear [N]
- F_A – Total load on the Center of Gravity [N]
- d' – distance between Nose and main landing gear considering an inclination of 14 degrees [m] (see Figure 37)
- b' – distance between C.G. and the main landing gear considering an inclination of 14 degrees [m] (see Figure 37)
- a' – distance between C.G. and the nose landing gear considering an inclination of 14 degrees [m] (see Figure 37)

Considering the relation between the horizontal and vertical forces it's possible to admit:

$$R_1^X = k \, F_A \frac{b'}{d'} \tag{11}$$

$$R_1^y = F_A \frac{b'}{d'} \tag{12}$$

Where the total load on the Center of Gravity is represented by:

$$\tag{13}$$

$$F_A = n_j \, W$$

Where n_j is the load factor.

These results can be easily verified by:

$$\tag{14}$$

$$R_1 = F_A * \frac{b'}{d'} \, , [N]$$

$$\tag{15}$$

$$R_2 = F_A * \frac{a'}{d'} \, , [N]$$

Considering the two components of R_1:

$$\tag{16}$$

$$R_1 = \sqrt{R_1^{X\,2} + R_1^{y\,2}}, [N]$$

$$R_1 = \sqrt{(K F_A \frac{b'}{d'})^2 + (F_A \frac{b'}{d'})^2}, [N]$$

Recalling that $F_A = n_j \, W$:

$$R_1 = \sqrt{(K \, n_j \, W \frac{b'}{d'})^2 + (n_j \, W \frac{b'}{d'})^2}, [N]$$

Considering the same for R_2: $\tag{17}$

$$R_2 = \sqrt{R_2^{X\,2} + R_2^{y\,2}}, [N]$$

$$R_2 = \sqrt{(K \, F_A \frac{a'}{d'})^2 + (F_A \frac{a'}{d'})^2}, [N]$$

Once again, recalling that $F_A = n_j\, W$:

$$R_2 = \sqrt{(K\, n_j\, W\, \frac{a'}{d'})^2 + (\, n_j\, W\, \frac{a'}{d'})^2}, [N]$$

Considering that:

$$F_A = R_1 + R_2 \quad , [N]$$

It's then possible to admit that:

(18)

$$F_A = \sqrt{(K\, n_j\, W\, \frac{b'}{d'})^2 + (\, n_j\, W\, \frac{b'}{d'})^2} + \sqrt{(K\, n_j\, W\, \frac{b'}{d'})^2 + (\, n_j\, W\, \frac{b'}{d'})^2} \quad , [N]$$

On the other hand, it's also possible to consider that:

$$F_A = \sqrt{(F_A{}^X)^2 + (F_A{}^Y)^2}$$

And regarding the relation established in equation 7:

(19)

$$F_A = \sqrt{(K\, n_j\, W\,)^2 + (\, n_j\, W\,)^2} = \sqrt{(\, n_j\, W\,)^2 (k^2 + 1)}$$

Equalling equation 19 and equation 18 we obtain:

(20)

$$\sqrt{(\, n_j\, W\,)^2 (k^2 + 1)} = \sqrt{(K\, n_j\, W\, \frac{b'}{d'})^2 + (\, n_j\, W\, \frac{b'}{d'})^2} + \sqrt{(K\, n_j\, W\, \frac{a'}{d'})^2 + (\, n_j\, W\, \frac{a'}{d'})^2}$$

(21)

$$(=) (\, n_j\, W\,)\sqrt{(k^2 + 1)} = \sqrt{(\, n_j\, W\,)^2 (k^2 + 1)\, \frac{b'^2}{d'^2}} + \sqrt{(\, n_j\, W\,)^2 (k^2 + 1)\, \frac{a'^2}{d'^2}}$$

(22)

$$(=) (\, n_j\, W\,)\sqrt{(k^2 + 1)} = n_j\, W\, \frac{b'}{d'}\sqrt{(k^2 + 1)} + n_j\, W\, \frac{a'}{d'}\sqrt{(k^2 + 1)}$$

(23)

$$n_j\, W = n_j\, W\, \frac{b'}{d'} + n_j\, W\, \frac{a'}{d'}$$

Note:

$$b' + a' = d'$$

$$\frac{b'}{d'} + \frac{a'}{d'} = 1$$

So it's easy to conclude that:

$$n_j\, W \ = n_j\, W \tag{24}$$

Nose landing gear vertical loading on a level landing - see Figure 37 - with inclined reactions due to inertia forces can be represented by:

$$Vnose = \frac{(n - L)\, b'\, W}{d'} \ , [N] \tag{25}$$

Where:

- Vnose – Nose landing gear vertical loading on a level landing [N]
- W – Maximum weight of the aircraft at the landing instant [N]
- L – Lift Weight ratio [L = 2/3]
- n - Load factor

$$tang\ \propto = \ k$$

Considering that k is 0.25,

$$\propto = 14^{\underline{o}}$$

Where:

- $\propto$ - Angle of the combined force of Vnose and Dnose with the vertical axis that crosses the C.G. of the aircraft

The load on the nose landing gear due to drag (spin-up forces) is:

$$Dnose = \frac{k\, n\, W\, b'}{d'} \ \ , [N] \tag{26}$$

Where:

- k – is the assumed drag coefficient between the wheel and the ground
- Dnose – Nose landing gear horizontal loading on a level landing [N]

Also for a level landing, the spin-up and spring-back situations must be considered when the nose wheel touches the ground.

Spin up is the moment when the wheel touches the pavement on landing. This is important in case of heavy wheels (because they go from 0 to airplane linear speed in one or two seconds).

Spring back is what follows spin-up situation. Drag force has pulled the gear assembly into the tail of the aircraft and as the wheel speed matches the speed of the aircraft, the nose gear assembly is pushed back to the front of the airplane.
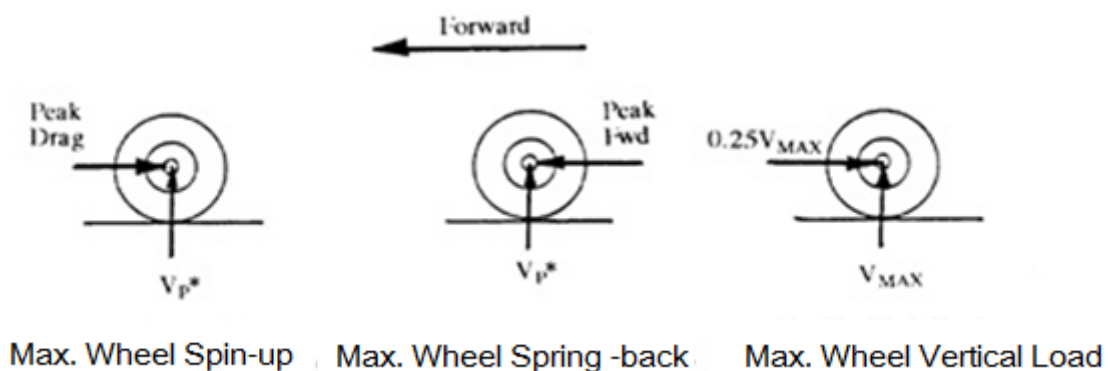
Figure 38 - Spin-up and Spring-back condition on a 3 point landing - Nose wheel in 3 different moments - (Ni 1992)

All this information can be found summed up in STANAG 4703/ NATO AEP-83, Annex B, UL.GL 1

Table 2 - Basic Landing Conditions for different types of landing gears - (NATO 2014)

Condition	Tail Wheel Type		Nose Wheel Type		
	Level Landing	Tail-down Landing	Level Landing with Inclined Reactions	Level Landing with Nose Wheel Just Clear of Ground	Tail-Down Landing
Vertical component at CG	nW	nW	nW	nW	nW
Fore and aft component at CG	KnW	0	KnW	KnW	0
Lateral component in either direction at CG	0	0	0	0	0
Shock absorber deflection (rubber or spring shock absorber), %	100 %	100 %	100 %	100 %	100 %
Tire deflection	Static	Static	Static	Static	Static
Main wheel loads (V_r)	(n-L)W	(n-L)Wb/d	(n–L)Wa'/d'	(n-L)W	(n-L)W
(both wheels) (D_r)	KnW	0	KnWa'/d'	KnW	0
Tail (nose) wheels (V_r)	0	(n-L)Wa/d	(n-L)W'/d'	0	0
Loads (D_r)	0	0	KnWb'/d'	0	0

Two mistakes were found in this table and that are indicated with red colour in the Table 3.

The first mistake is the letter "n" that must be corrected by "**nj**". The second mistake is the lack of the letter " **b'** " in the nose wheel vertical reaction.

Table 3 – Corrections of mistakes that were found in Table 2.

Condition	Tail Wheel Type		Nose Wheel Type		
	Level Landing	Tail-down Landing	Level Landing with Inclined Reactions	Level Landing with Nose Wheel Just Clear of Ground	Tail-Down Landing
Vertical component at CG	nW	nW	nW	nW	nW
Fore and aft component at CG	KnW	0	KnW	KnW	0
Lateral component in either direction at CG	0	0	0	0	0
Shock absorber deflection (rubber or spring shock absorber), %	100 %	100 %	100 %	100 %	100 %
Tire deflection	Static	Static	Static	Static	Static
Main wheel loads (V_r)	(n-L)W	(n-L)Wb/d	(n-L)Wa'/d'	(n-L)W	(n-L)W
(both wheels) (D_r)	KnW	0	Kn Wa'/d'	KnW	0
Tail (nose) wheels (V_r)	0	(n-L)Wa/d	(n-L)W b'/d'	0	0
Loads (D_r)	0	0	Kn Wb'/d'	0	0

nj

b'

Note:

- $L = \frac{2}{3}$ coefficient between lift and weight assumed at the landing moment

- N is the load factor ($n = n_j + 2/3$)

- n_j is the load factor on wheels

An email was sent to NATO, so that they acknowledge the errors and correct them – see Annex D: NATO Email contact.

Besides this situation, (NATO 2014) advises to consider three different supplementary conditions.

The static load of these is calculated considering that the aircraft is not moving and that the sum of forces and moments on C.G. is zero. (See Figure 39)
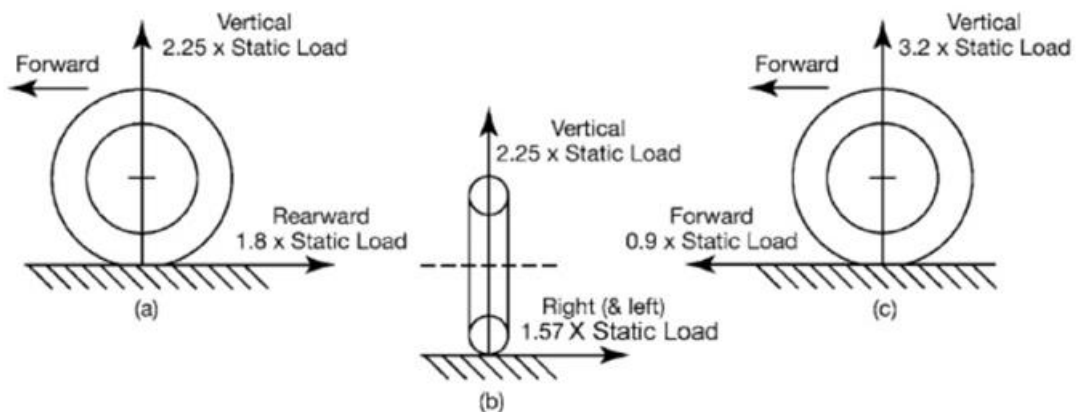
Figure 39 - Supplementary Conditions for nose wheel landing gear - (NATO 2014)

(a) – For aft loads, the limit force components at the axle must be:

- A vertical component of 2.25 times the static load on the wheel;
- A drag component of 1.8 times the vertical load.

(b) – For side loads, the limit force components at ground contact must be:

- A vertical component of 2.25 times the static load on the wheel;
- A side component of 1.57 times the static load on the wheel.

(c) – For forward loads, the limit force components at the axle must be:

- A vertical component of 3.20 times the static load on the wheel;
- A Forward component of 0.9 times the static load on the wheel;

Where, as explained in reference (FLUGZEUGBAU 2016):

- Aft loads are all type of forces that pushes the nose landing gear into the tail direction (for example an obstacle on the runway during taxiing)
- Side loads are all type of solicitations that produces a rotation of the nose landing gear around the aircraft longitudinal axis. (for example: Cross wind landing or turning fast during taxiing)
- Forward loads are all type of forces that pushes the nose landing gear to the front of the aircraft (for example when an airplane is parked in an inclined parkway and has a choke positioned behind the wheel as shown in the figure below).

Figure 40 - Landing gear with chokes - (Media Defense 2012)

Besides those supplementary conditions there are also others that will be considered during the landing gear tests:

1. Ground turning - In this case the nose landing gear should also account for a side load of 0.5 of the vertical load. The vertical load that was used was the static load, considering that the aircraft has landed and that there are no more vertical movements.
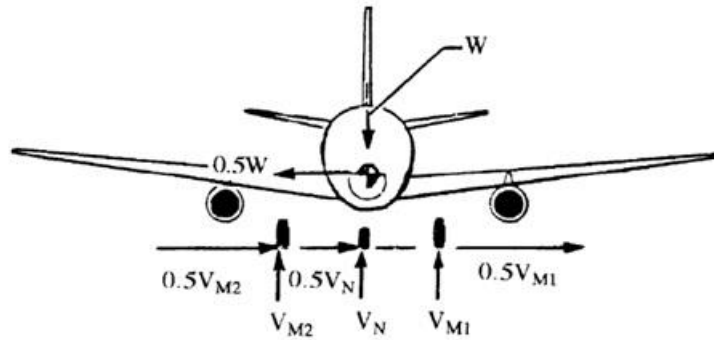
Figure 41 - Ground turning condition - (Ni 1992)

2. Exaggerated Ground turn – The nose wheel skids and results in a side load of 0.8 times the vertical load. As the situation before, the vertical load that was used was the static load, considering that the aircraft has landed and that there are no more vertical movements.
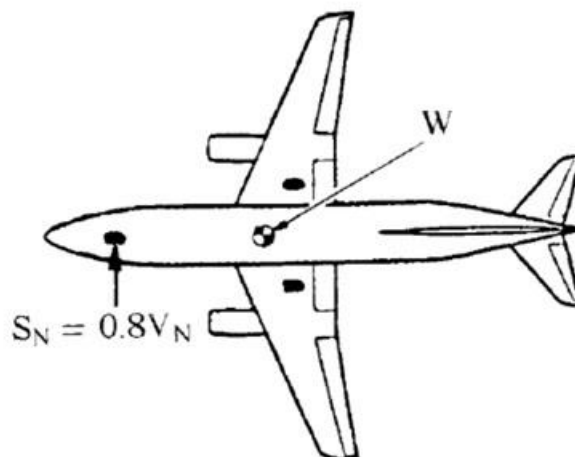
Figure 42 - Exaggerated ground turn condition - (Ni 1992)

Safety factors:

As a landing gear is considered a PSE, an ultimate load factor of safety ≥ 1.5 should be used to determine the ultimate loads (AVIATION GLOSSARY 2012).

In composite structures, if A or B allowable for hot and wet conditions are not statistically justified, the following special factors should be used: ≥ 1.2 for moisture conditioned specimen tested at maximum service temperature, providing that a well-established manufacturing and quality control procedure is used; or ≥ 1.5 for specimen tested with no specific allowance for moisture and temperature.

Note:

'A' values - value above which at least 99% of the population of values is expected to fall with a confidence of 95%

'B' values - value above which at least 90% of the population of values is expected to fall with a confidence of 95%

This means that only 1% (A' values) and 10% (B' values) of the material is likely to be below the strength values presented. See Figure 43 for an example of B' values. (MALLICK 1993)
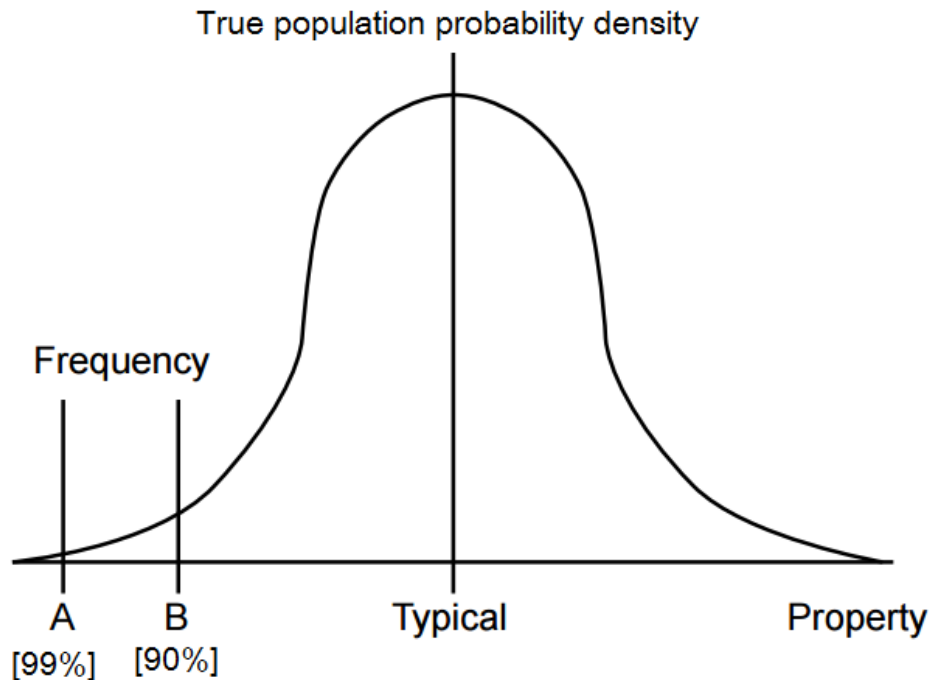
Figure 43 - Example of a normal distribution for 'A' and 'B' values (Montana State University s.d.)

The following criteria in choosing material allowable should be used.

Where applied loads are eventually distributed through a single member within an assembly, the failure of which would result in the loss of the structural integrity of the component involved, the guaranteed minimum design mechanical properties 'A' values should be met.

It was considered that properties of materials provided by CEiiA were statistically justified because previous considerations were already conservative. However, if certification must be obtained, tests that characterize the material according to recommended norms by aeronautical industry must be accomplished.

3.1.1.2 Drop height calculation

The drop height expression can be easily explained by the following considerations:

According to (EASA 2009) at the landing moment, the airplane has a certain vertical speed in meters per second, estimated by:

$$v_v = 0.51 \left(\frac{mg}{S} \right)^{\frac{1}{4}} , \quad 2.1 < v < 3 \; [\frac{m}{s}] \tag{27}$$

According to EASA, this equation was determined experimentally.

And equaling kinetic energy to potential energy and using equation 30:

$$E_{kinetic} = E_{potential}$$

$$(=)\ \frac{mv^2}{2} = m\,g\,h$$

$$(=)\ \frac{1}{2}m\,0.2601 * \sqrt{\frac{m\,g}{S}} = m\,g\,h$$

$$(=)\ \boldsymbol{h = 0.0132} * \sqrt{\frac{\mathbf{m\,g}}{\mathbf{S}}} \qquad (28)$$

Note: h should be larger than 0.235m according to reference (EASA 2009) and 0.229m according to reference (NATO 2014), thus, the later shall be considered.

Where:

- S – Aircraft wing surface Area [m^2]

3.1.2. Selection of landing gear configuration

Comparing different dispositions presented in Figure 29, it is possible to assume that the best option is the first one. The main reasons for this choice are presented in the next paragraphs.

Figure 44 presents the typical force diagram for a landing.

It is easy to assume that during the moment of the landing there are forces horizontal and vertical forces, even though vertical component being the largest one.
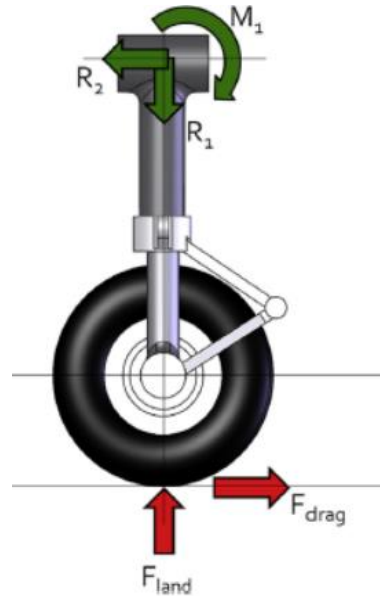
Figure 44 - Two dimensions' force diagram in a landing gear - (Gudmundsson 2014)

Now with this in mind, it is possible to compare those 4 shapes presented in Figure 29 (considering that are manufactured in composite materials).

The simplest configuration is the 3rd one. Taking into account the horizontal component of the force and the fact that composites have better performance with in-plane stresses, this landing gear configuration would probably have serious problems of delamination since the horizontal component has a 90º angle with the landing gear.

The 4th configuration has a better performance than the 3rd one because it has an angle that permits to absorb both horizontal and vertical components of those 2 forces.

The 2nd configuration is a mixture between number 4 and number 1. It has a bigger volume for the same frontal area that number 4 (turning out in a similar drag coefficient) which is an advantage because it permits to distribute the same load through more material without increasing drag in a significant way.

Furthermore, there is a significant issue: the stress concentration in configurations 2 and 4 as presented in Figure 45.
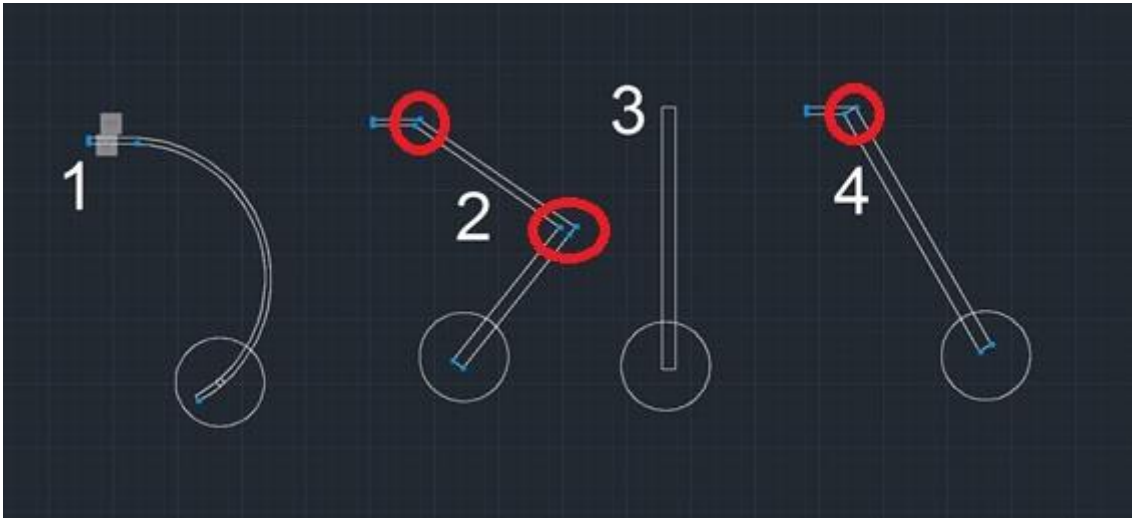
Figure 45 - Points of stress concentration

In order to eliminate this problem, it is important to design softer changes of direction: curves instead of abrupt change of geometry.

With this in mind, we can solve this problem by choosing configuration 1, or improving configuration 4 (see Figure 46).
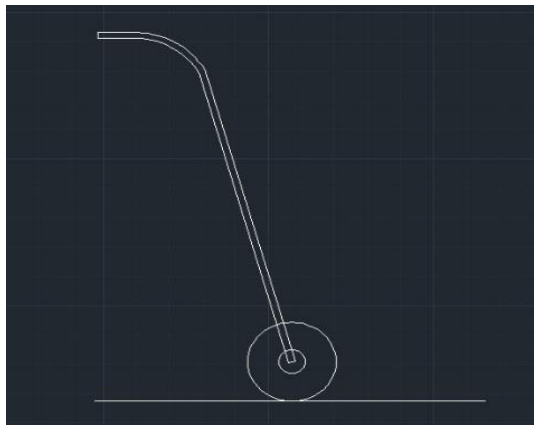
Figure 46 - Refined 4th configuration

3.2. Theoretical model of curved beams

3.2.1. Bending stresses in curved beams with rectangular cross sections

To determine the bending stresses in curved beams, a typical approach for straight beams is not applicable to all curved beams.

With this said it is necessary to use a different option and to assume the following (S.Timoshenko 1940):

•   Center line (line joining the centroids of the cross sections of the beam) of the bar is a plane curve and the cross section have an axis of symmetry in this plane

•   The bar is submitted to the action of forces lying in the plane of symmetry

•   Straight sections, originally plane and normal to the center line of the bar will remain so after the solicitation
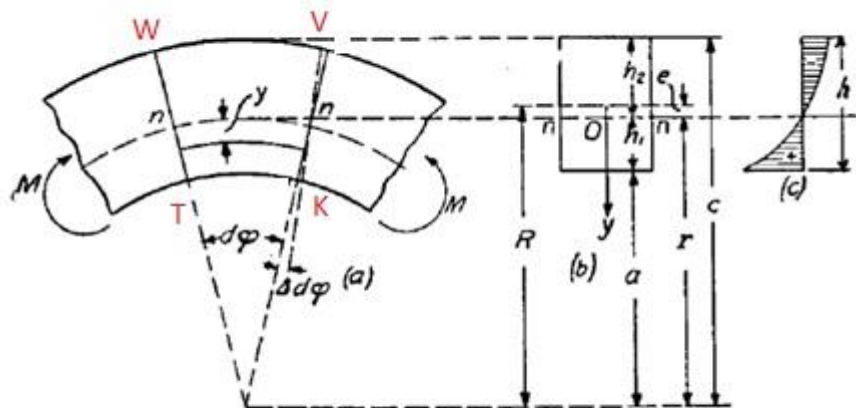
Figure 47 - Part of a bended curved beam - (S.Timoshenko, 1940)

Considering **_dφ_** a small angle between sections **_WT_** and **_VK_** them and **_Δdφ_** a small rotation (see Figure 47).

Due to this rotation the longitudinal fibers on the convex side of the bar are compressed and the fibers on the concave side are extended.

Note:

- n-n denotes the neutral axis;

- r denotes the radius of the neutral surface

- **_yΔdφ_** is the extension of any fiber a distance y from the neutral surface

- **_(r-y) dφ_** is the length of the fiber between the adjacent cross section before bending

- **_M_** - Moment applied at each side of the beam

The elongation (strain) is:

$$\varepsilon = \frac{y\Delta d\varphi}{(r-y)d\varphi} \tag{29}$$

Assuming a situation of no lateral pressure between the longitudinal fibers, the bending stress at a distance **y** from the neutral axis is:

$$\sigma_x = E\ \varepsilon \tag{30}$$

$$(=)\ \sigma_x = E\frac{y\Delta d\varphi}{(r-y)d\varphi} \tag{31}$$

Where:

- σ_x - Normal stress
- ε - Strain

Since the sum of the normal forces distributed over the cross section is zero, the neutral axis is displaced from the centroid of the cross section towards the center of curvature of the beam. Thus, in the case of a rectangular cross section, the area in tension must equal that in compression, therefore, the greatest bending stress acts on the concave side (see Figure 47).

In the last equation there are two unknowns: r and angle $\Delta d\varphi$. To determine them it is necessary to use two static equations:

1. The first is based on the condition that the sum of normal forces distributed over a cross section is equal to zero.

$$\Sigma F = 0 \tag{32}$$

$$(=)\ \int \sigma_x dA = 0 \tag{33}$$

$$(=)\frac{E\Delta d\varphi}{d\varphi}\int \frac{ydA}{r-y} = 0 \tag{34}$$

$$(=)\ \int \frac{ydA}{r-y} = 0 \tag{35}$$

Where:

A – Area of the cross section

2. The second equation is based on the condition that the moment of these normal forces is equal to the bending moment M.

$$\Sigma M_{Fn} = M \tag{36}$$

$$(=) \int \sigma_x y dA = M \tag{37}$$

$$(=) \frac{E\Delta d\varphi}{d\varphi} \int \frac{y^2 dA}{r-y} = M \tag{38}$$

Simplifying the integral of equation 38 and replacing equation 35 into this simplification, it's possible to obtain:

$$\int \frac{y^2 dA}{r-y} = -\int \left(y - \frac{ry}{r-y} \right) dA \tag{39}$$

$$(=) \int \frac{y^2 dA}{r-y} = -\int y \, dA + r \int \frac{y \, dA}{r-y} \tag{40}$$

$$(=) \int \frac{y^2 dA}{r-y} = -\int y \, dA \tag{41}$$

$$(=) \int \frac{y^2 dA}{r-y} = -\int_0^{-e} y \, dA \tag{42}$$

$$(=) \int \frac{y^2 dA}{r-y} = eA \tag{43}$$

here:

e – Distance of the neutral axis from the centroid of the cross section

The above equation represents the moment of cross sectional area with respect to the neutral axis.

So, equation 38 becomes:

$$\frac{E \Delta d\varphi}{d\varphi} = \frac{M}{A\,e} \tag{44}$$

And finally, replacing equation 44 into equation 31:

$$\sigma_x = \frac{M\,y}{(r-y)\,A\,e} \tag{45}$$

Thus, the largest bending stresses in the bar are:

$$(\sigma_x)_{max} = \frac{M h_1}{A e a} \tag{46}$$

$$(\sigma_x)_{min} = \frac{-M h_2}{A e c} \tag{47}$$

Note:

- **h₁** and **h₂** are the distances from the neutral axis to the most remote fibers.
- **a** and **c** are the inner and outer radius of the bar.

Typically, **if the depth of the cross section is small in comparison with the radius R of the center**, y may be neglected in comparison with r and then we obtain from equation 34:

$$\frac{E \Delta d\varphi}{d\varphi} \int \frac{y\,dA}{r-y} = 0 \underset{y \ll r}{\Longrightarrow} \int y\,dA = 0 \tag{48}$$

Which means that the neutral axis passes through the centroid of the cross section.

Furthermore, from equation 37,

$$\frac{E\Delta d\varphi}{d\varphi} \int \frac{y^2 dA}{r - y} = M \underset{y \ll r}{\Longrightarrow} \frac{E\ \Delta d\varphi}{d\varphi} \frac{I_z}{R} = M \tag{49}$$

Where:

- I_z - Second moment of area, also known as moment of inertia of a plane area. [mm^2]
- R – Radius of the center line of the beam [mm]

Substituting the equation 49 into equation 31:

$$\sigma_x = \frac{Ey\Delta d\varphi}{(r - y)d\varphi} (=) \sigma_x = \frac{MRy}{I_z(r - y)} \underset{y \ll r}{\Longrightarrow} \sigma_x = \frac{MRy}{I_z R} (=)\sigma_x = \frac{My}{I_z} \tag{50}$$

An alternative approach to determine the bending stress of a curved beam is to consider a linear distribution and then apply a correction factor as suggests (PIKEY, W, 1997).

$$\sigma = K_t \frac{M}{I/c} \tag{51}$$

Where **K$_t$** factor is obtained using the Figure 48:
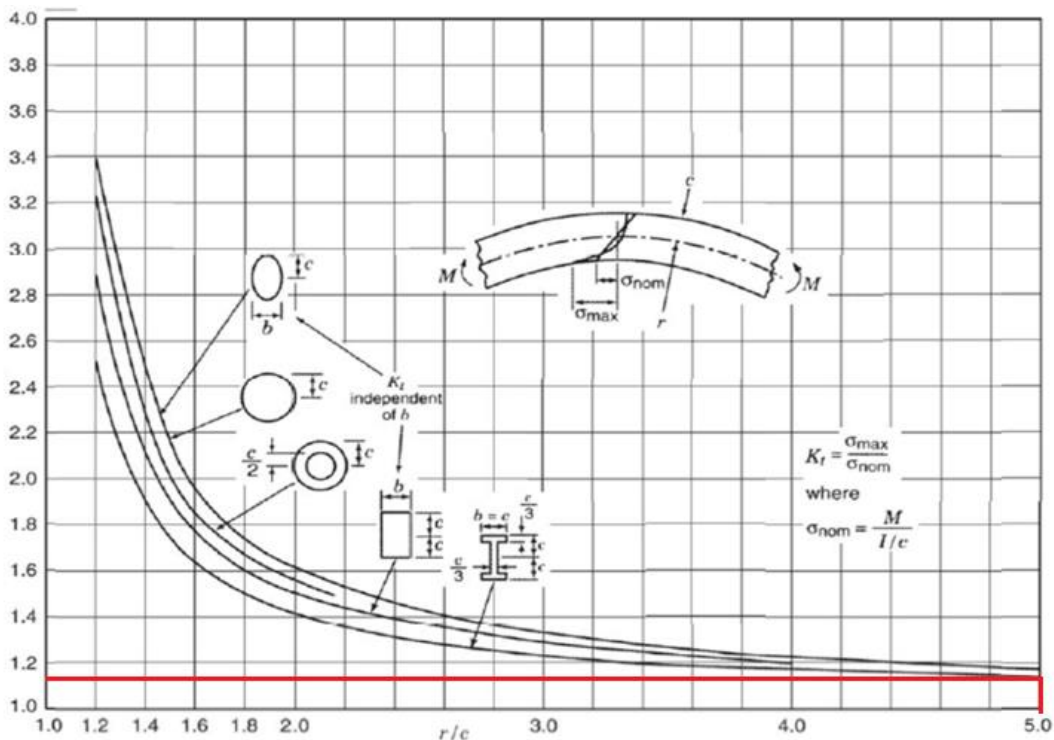
Figure 48 - Max. Stress of a straight section in a curved beam with flexion - (Pikey, W, 1997)

Where:

- c – geometric property (depending on the shape of the section)
- I – Moment of inertia

3.2.2. Vertical displacement of a curved beam whose center line is half of a circle
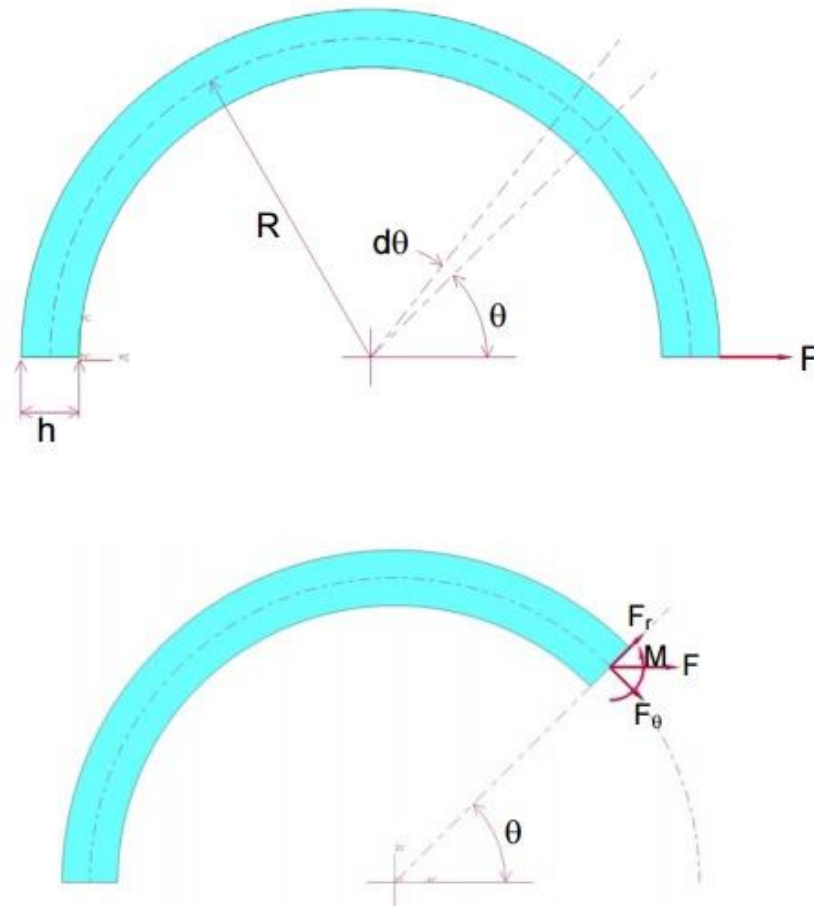
Figure 49 - Curved beam - (University of Washington 2016)

Remind that the strain energy in the element defined by the angle dθ, moment M and the force F, that can be resolved into components F_r and F_Θ (University of Washington 2016).

There are 3 components of the strain energy:

1. Axial Force:

   The energy stored for tension during strain is:

$$U_1 = F_\Theta \frac{\delta}{2}$$

$$\varepsilon = \frac{\delta}{l} = \frac{\sigma}{E} = \frac{F_\theta}{AE}$$

Then,

$$U_1 = \frac{F_\theta{}^2 l}{2AE} \tag{52}$$

Where:
- F_θ – Tangencial Force
- l – Length of a beam
- A – Sectional Area
- E – Young Modulus

The internal energy stored in an element of the beam of length dx is:

$$dU_1 = \frac{F_\theta{}^2 dx}{2AE} \tag{53}$$

Considering a curved beam, it's possible to affirm that:

$$dx = R\, d\theta \tag{54}$$

Then, replacing equation 54 into equation 53:

$$\boldsymbol{dU_1 = \frac{F_\theta{}^2 R\, d\theta}{2AE}} \tag{55}$$

2. Transverse Force:

The elastic strain energy stored when force F_r is applied is:

$$U_2 = \frac{F_r \delta}{2} \tag{56}$$

And remembering that:

$$\frac{\delta}{l} = \varepsilon = \frac{\tau}{G} = \frac{F_r}{AG} \tag{57}$$

Where

- F_r − Radial force
- G − Transverse Modulus
- δ – Displacement of the beam along its axis

Replacing equation 57 into equation 56 it's possible to obtain:

$$U_2 = \frac{F_r^2 l}{2AG} \tag{58}$$

The internal energy stored in an element of the beam of length dx is:

$$dU_2 = \frac{F_r^2 dx}{2AG} \tag{59}$$

Considering a curved beam whose center line is half of a circle it's possible to affirm that:

$$dx = R \, d\theta \tag{60}$$

Thus, replacing equation 60 into equation 59:

$$dU_2 = \frac{F_r^2 R \, d\theta}{2AG} \tag{61}$$

But it's necessary to consider a correction factor (C = 1.5 – for rectangular cross section in shear). This correction factor exists because in pure bending it's considered that all the cross sections will remain plane and perpendicular to the longitudinal axis. This assumption doesn't deliberate the effect of shear strains that creates a warping effect in those sections. This correction factor is dependent upon the shape of the cross section. (S.Timoshenko 1940)

$$\boldsymbol{dU_2 = \frac{C \, Fr^2 R \, d\theta}{2AG}} \tag{62}$$

3. Bending force:

Recalling bending force for straight beams:

$$U_3 = \frac{M\varphi}{2} \tag{63}$$

$$\varphi = \frac{Ml}{EI_z} \tag{64}$$

Where:

- I_Z – Sectional Inertia

$$U_3 = \frac{M^2 l}{2EI_z} \tag{65}$$

The internal energy stored in an element of the beam of length dx is:

$$dU_3 = \frac{M^2 dx}{2EI_z} \tag{66}$$

Considering a curved beam whose center line is half of a circle it's possible to affirm that:

$$dx = R \, d\theta \tag{67}$$

Therefore, replacing equation 67 into equation 66:

$$\boldsymbol{dU_3} = \frac{\boldsymbol{M^2 \, R \, d\theta}}{\boldsymbol{2 \, E \, I}}, \textbf{for R/h > 10} \tag{68}$$

Combining equations: 55, 62 and 68 the total Strain is:

$$\boldsymbol{U} = \int \frac{\boldsymbol{F_\theta^2 \, R \, d\theta}}{\boldsymbol{2 \, A \, E}} + \int \frac{\boldsymbol{C \, F_r^2 R \, d\theta}}{\boldsymbol{2 \, A \, G}} + \int \frac{\boldsymbol{M^2 \, R \, d\theta}}{\boldsymbol{2 \, E \, I}} \tag{69}$$

Recalling Castigliano's theorem:

"The displacement corresponding to any force applied to an elastic structure and collinear with that force is equal to the partial derivative of the total strain energy with respect to that force."

$$\delta_i = \frac{\partial U}{\partial F_i} \tag{70}$$

Replacing equation 69 to 70:

$$\delta_v = \frac{\partial u}{\partial F} = \int_0^\pi \frac{F_\theta\, R}{A\, E} \left(\frac{\partial F_\theta}{\partial F}\right) d\Theta + \int_0^\pi \frac{C\, F_r\, R}{A\, G} \left(\frac{\partial F_r}{\partial F}\right) d\Theta + \int_0^\pi \frac{M\, R}{E\, I} \left(\frac{\partial M}{\partial F}\right) d\Theta \tag{71}$$

From Figure 49:

- $M = FR\, sin\Theta$
- $F_\theta = F\, sin\Theta$
- $F_r = F\, cos\Theta$

Then:

$$\delta_v = \frac{F\, R}{A\, E} \int_0^\pi (sin\Theta)^2\ d\Theta + \frac{C\, F\, R}{A\, G} \int_0^\pi (cos\Theta)^2\ d\Theta + \frac{F\, R^3}{E\, I} \int_0^\pi (sin\Theta)^2\ d\Theta \tag{72}$$

$$(=)\ \delta_v = \frac{\pi\, F\, R}{2\, A\, E} + \frac{\pi\, C\, F\, R}{2\, A\, G} + \frac{\pi\, F\, R^3}{2\, E\, I} \tag{73}$$

Considering that R/h is large, the two first terms will be small, then the vertical displacement is:

$$\boldsymbol{\delta_v = \frac{\pi\, F\, R^3}{2\, E\, I}} \tag{74}$$

55

3.2.3. Horizontal displacement of a curved beam whose center line is half of a circle
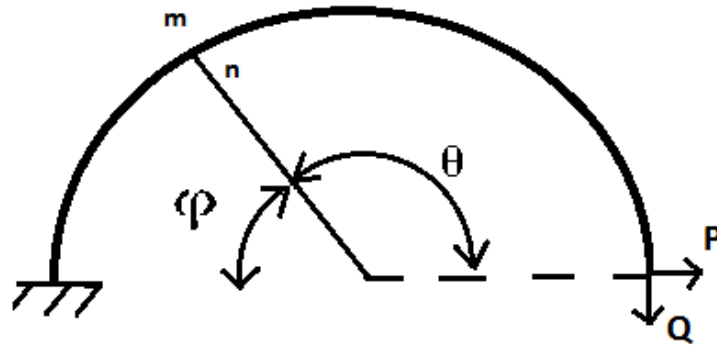
Figure 50 - Half circle

The bending moment caused by forces P and Q in *m-n* section is:

$$M_b = P\,R\,\sin\varphi + Q\,(R + R\,cos\varphi) \tag{75}$$

Considering:

1. Q – It is a virtual force
2. $\Theta = \pi - \varphi$

Replacing this into equation 75:

$$M = P\,R\,\sin\,(\pi - \theta) + Q\,R\,(1 + \cos(\pi - \theta)) \tag{76}$$

Considering:

1. $\sin\,(\pi - \theta) = sin\varphi = sin\theta$
2. $\cos\,(\pi - \theta) = -cos\theta$

   Then, replacing this into equation 76:

$$M = P \, R \, \sin \theta + Q \, R \, (1 - \cos \theta) \tag{77}$$

Recalling Castigliano theorem to calculate horizontal displacement caused by force P:

$$\delta_h = \left. \frac{\partial U}{\partial Q} \right|_{Q=0} \tag{78}$$

From equation 68:

$$dU_3 = \frac{M^2 \, R \, d\theta}{2 \, E \, I} \;(=)\; U = \int_0^\pi \frac{M^2 \, R}{2EI} d\theta \tag{79}$$

Replacing equation 79 into 78:

$$\delta_h = \frac{\partial}{\partial Q} \int_0^\pi \left. \frac{M^2 R}{2EI} \right|_{Q=0} d\theta \tag{80}$$

$$= \frac{R}{2EI} \int_0^\pi \left. \frac{\partial M^2}{\partial Q} \right|_{Q=0} d\theta \tag{81}$$

Note:

$$\frac{\partial M^2}{\partial Q} = \frac{\partial (MM)}{\partial Q} = \frac{M \, \partial M}{\partial Q} + \frac{\partial M \, M}{\partial Q} = \frac{2 \, M \, \partial M}{\partial Q}$$

Then, using these relations, equation 81 becomes:

$$\delta_h = \frac{R}{2EI} \int_0^\pi \left. \frac{2 \, M \, \partial M}{\partial Q} \right|_{Q=0} d\theta \tag{82}$$

$$(=)\; \delta_h = \frac{R}{EI} \int_0^\pi \left. \left(P \, R \, sin\theta + Q \, R \, (1 - cos\theta) \right) R(1 - cos\theta) \right|_{Q=0} d\theta$$

$$(=)\; \delta_h = \frac{R^3}{EI} \int_0^\pi (P \, sin\theta) \, (1 - cos\theta) d\theta$$

$$(=)\; \boldsymbol{\delta_h = 2 \, \frac{P \, R^3}{EI}} \tag{83}$$

3.2.4. Stress in an curved beam whose center line is half of an ellipse

Stress was calculated the same way than circular beam because it's considered curved beam (S.Timoshenko 1940) (Pikey 1997).

$$\sigma = k_t \frac{My}{I}$$
<div align="right">(84)</div>

3.2.5. Vertical displacement of curved beam whose center line is half of an ellipse

The bending moment caused by forces P and Q in m-n section is:

$$M = P \, b \, \sin\theta + Q \, (a - a \cos\theta)$$
<div align="right">(85)</div>
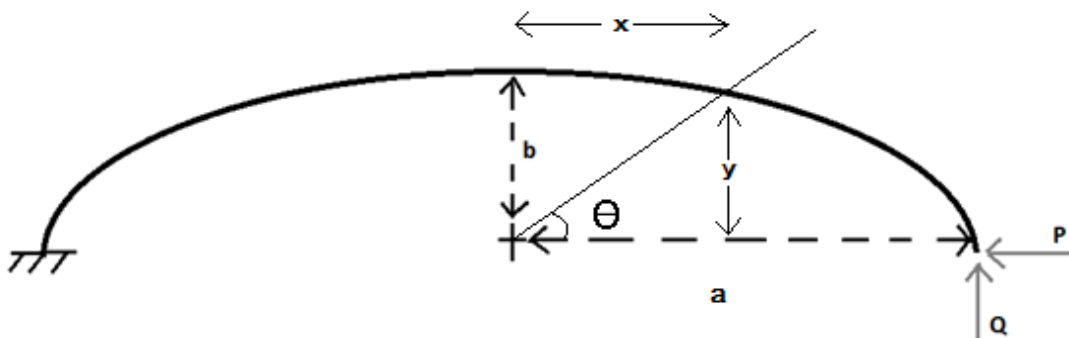
Figure 51 - Half circle beam

Considering:

1. Q – It is a virtual force

 From reference (Tadashi Horibe 2015):

Considering the equation of an ellipse:

$$\frac{x^2}{a^2} + \frac{x^2}{b^2} = 1$$
<div align="right">(86)</div>

Introducing the parameter Θ:

$$x = a\cos\Theta, \qquad y = b\sin\Theta \tag{87}$$

The infinitesimal arc length ds on the ellipse is:

$$ds = \sqrt{dx^2 + dy^2} = \sqrt{(\tfrac{dx}{d\Theta})^2 + \left(\tfrac{dy}{d\Theta}\right)^2} = a\sqrt{1 - e^2 \cos^2\Theta}\, d\Theta \tag{88}$$

Where $e = \sqrt{1 - (\tfrac{b}{a})^2}$ is the eccentricity.

Again, recalling Castigliano theorem, the vertical displacement caused by force P:

$$\delta_v = \frac{\partial U}{\partial P} \tag{89}$$

From equation 79,

$$dU_3 = \frac{M^2 dx}{2EI_z}$$

For the ellipse, dx = ds, thus, using equation 88,

$$U = \int_0^\pi \frac{M^2}{2EI}\, a\, \sqrt{1 - e^2 \cos^2\Theta}\, \Bigg|_{Q=0} d\theta \tag{90}$$

Using equation 71,

$$\delta_v = \frac{\partial}{\partial P} \int_0^\pi \frac{M^2}{2EI}\, a\, \sqrt{1 - e^2 \cos^2\Theta}\, \Bigg|_{Q=0} d\theta \tag{91}$$

$$(=)\delta_v = \frac{a}{2EI} \int_0^\pi \frac{\partial M^2}{\partial P}\, \sqrt{1 - e^2 \cos^2\Theta}\, \Bigg|_{Q=0} d\theta \tag{92}$$

Note:

$$\frac{\partial M^2}{\partial P} = \frac{\partial (MM)}{\partial P} = \frac{M\, \partial M}{\partial P} + \frac{\partial M\, M}{\partial P} = \frac{2\, M\, \partial M}{\partial P}$$

Then replacing these relations into equation 92,

$$\delta_v = \frac{a}{2EI} \int_0^\pi \frac{2\,M\,\partial M}{\partial P} * \sqrt{1 - e^2 cos^2\Theta}\bigg|_{Q=0} d\theta$$

$$(=) \; \delta_v = \frac{a}{2EI} \int_0^\pi 2\,P\,b\,sin\theta\,b\,sin\theta\,\sqrt{1 - e^2\,cos^2\Theta}\,d\theta$$

$$(=) \; \boldsymbol{\delta_v = \frac{P\,a\,b^2}{EI} \int_0^\pi (sin\theta)^2\,\sqrt{1 - e^2\,cos^2\Theta}\,d\theta} \tag{93}$$

This part is solved using a Matlab® function as explained in chapter 5.2.1.

3.2.6. *Horizontal displacement of a curved beam whose center line is half of an ellipse*

Once again, considering:

1. Q – It is a virtual force

And, recalling Castigliano theorem, to the horizontal displacement caused by force P:

$$\delta_h = \frac{\partial U}{\partial Q}\bigg|_{Q=0}$$

Using equation 90:

$$U = \int_0^\pi \frac{M^2}{2EI}\,a\,\sqrt{1 - e^2cos^2\Theta}\,\bigg|_{Q=0} d\theta \tag{94}$$

$$\delta_h = \frac{\partial}{\partial Q} \int_0^\pi \frac{M^2}{2EI}\, a\, \sqrt{1 - e^2 cos^2\Theta}\bigg|_{Q=0} d\theta$$

$$(=)\ \delta_h = \frac{a}{2EI} \int_0^\pi \frac{\partial M^2}{\partial Q} \sqrt{1 - e^2 cos^2\Theta}\bigg|_{Q=0} d\theta \tag{95}$$

Note:

$$\frac{\partial M^2}{\partial Q} = \frac{\partial(MM)}{\partial Q} = \frac{M\partial M}{\partial Q} + \frac{\partial MM}{\partial Q} = \frac{2\,M\,\partial M}{\partial Q} \tag{96}$$

Then, using these relations, equation 95 becomes,

$$(=)\delta_h = \frac{a}{2EI} \int_0^\pi \frac{2\,M\,\partial M}{\partial Q} \sqrt{1 - e^2\, cos^2\Theta}\, d\theta \tag{97}$$

$$(=)\delta_h = \frac{a}{2EI} \int_0^\pi 2P\, b\, sin\theta\, (a - acos\theta)\sqrt{1 - e^2 cos^2\Theta}\, d\theta$$

$$(=)\boldsymbol{\delta_h} = \frac{\boldsymbol{P\,b\,a^2}}{\boldsymbol{EI}} \int_0^\pi (\boldsymbol{sin\theta})^2\sqrt{\boldsymbol{1 - e^2 cos^2\Theta}}\, d\theta \tag{98}$$

This part is solved using a Matlab® function as explaned in chapter 5.2.1.

3.3. Composite materials

3.3.1. General characteristics of composite materials

The materials used to manufacture the landing gear should have high elastic strain energy storage capacity (MOHAMMED IMRAN 2014).

Most typical resins can be summed up in Table 4. The most used composites matrices in aircraft and aerospace structures are epoxy resins, which are thermoset resins (NI 1992).

Table 4 - Matrix characteristics - Composite Airframe Structures - (Ni 1992)

Epoxy	Bismaleimide	Polyimide
• Best structural characteristics • Maximum temperature of 93ºC • Easy to process • Toughened versions available	• Maximum temperature of 180ºC • Easy to process • Toughened versions available	• Variety of matrix types • Maximum temperature of 320ºC • Difficult to process • Expensive
Polyester	**Phenolic**	**Thermoplastics**
• Poor structural characteristics • Easy to process	• Poor structural characteristics • More difficult to process • Higher use of temperature than Epoxy and Polyester resins • Low smoke generation	• Greater improved toughness • Unique process capabilities • Have process difficulties • Shorter fabrication time than thermoset resins • No refrigeration required for storage • Low moisture sensitivity • No need for a chemical cure

Materials specifications are presented in Table 5:

Table 5 - Materials specification - Composite Airframe Structures - (Ni 1992)

	Graphite / Epoxy (unidirectional)		Kevlar/Epoxy (Woven Cloth)	Glass/Epoxy (Woven Cloth)	Boron/Epoxy	Aluminium	Beryllium	Titanium
	High Strength	High Modulus						
Specific Strength 10^6 m	0.14	0.05	0.03	0.02	0.08	0.02	0.03	0,02
Specific Stiffness 10^6 m	10.22	17.81	203.21	2.03	11.61	2.54	17.8	2.54
Density, Specific Strength Kg/m^3	1550	1743.8	1384.1	1799.1	1937.5	2767.9	1937.5	4428.6

To design composite aircraft structures (NI 1992) advises for some important details that must noted:

- Increased fiber rupture strain
- Good matrix shear strength
- Moderate inter-laminar fracture toughness
- Moderate matrix fracture toughness
- Good fiber/matrix interfacial adhesion
- Composite high in 0º compressive strength
- High post-impact compressive strength
- High matrix modulus
- Good-dependent properties: fatigue, creep
- Melt-process able matrices
- Solvent-resistant matrices
- Thermo-oxidative stability

Impact

Delamination

Compression

Processing
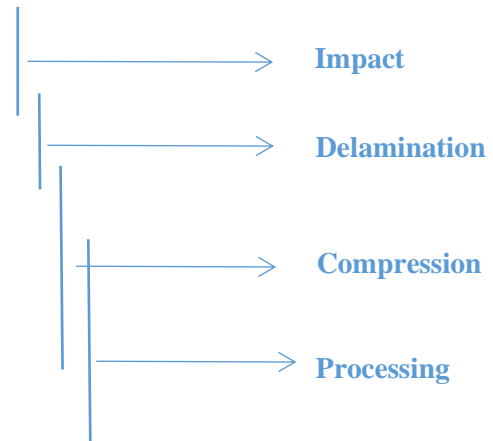
Analyzing different materials with an evaluation matrix – (see Table 6)

Table 6 - Relative Advantages of different material types - (Ni, 1992)

Material Properties	Relative Advantages		
	Thermoplastics	Thermosets	Metal
Corrosion resistance	xxx	xxx	x
Creep	xxx	xxx	x
Damage resistance	xx	x	xxx
Design Flexibility	xxx	xxx	x
Fabrication	xx	xx	x
Fabrication time	xxx	xx	x
Final Part Cost	xxx	xx	x
Moisture Resistance	xx	x	xxx
Physical Properties	xxx	xxx	xxx
Processing cost	xxx	xx	x
Raw material cost	x	xx	xx
Reusable Scrap	xx	X	xxx
Shelf Life	xxx	X	xxx
Solvent Resistance	xxx	xx	x
Specific Strength	xxx	xxx	x
Strength	xxx	xxx	x
Weight Saving	xxx	xx	0

According to (NI 1992) the **advantages** of composites over metals are:

• Light weight

• Resistance to corrosion

• Reduced machining

• Tapered sections and compound contours easily accomplished

• Can orientate fibers in direction of strength/stiffness needed

• Reduced number of assemblies and reduced fastener count when co-cure or consolidation is used

• Absorb radar microwaves (stealth capability)

• Thermal expansion near zero reduces thermal problems in outer space applications

• Higher resistance in tension fatigue loads (high performance composites)

And the **disadvantage**s of composites over metals are:

• Expensive materials (generally)

• Lack of established design allowables

• Corrosion problems can result from improper coupling with metals (when Carbon or Graphite is used)

• Degradation of structural properties under temperature extremes and wet conditions

• Poor energy absorption and impact damage

• May require lightning strike protection

- Expensive and complicated inspection methods

- Reliable detection of substandard bonds is difficult

- Defects can be known to exist but precise location cannot be determined

The most **used composites** for nose landing gears are:

- Carbon Fiber and epoxy resin

- Glass Fiber and epoxy resin

3.3.2. Materials selection criteria

Materials selection is generally a compromise that involves various considerations. Frequently the most **important considerations** are associated with **mechanical properties** (NI 1992).

Other considerations might be:
- Corrosion
- Environmental stability
- Availability and Productivity
- Costs
- Fabrication Characteristics
- Compatibility with other materials
- Thermal/electrical characteristics
- Wear characteristics

3.3.3. Laminate stacking sequence

To choose the laminate stacking sequence (LSS), (DEFENSE S.D.) provides some recommendations:

• Homogeneous LSS are recommended for strength controlled designs.

• A LSS should have at least four distinct ply angles (e.g. 0º, +- θº, 90º) with a minimum of 10% of the plies oriented at each angle.

• Minimize groupings of plies with the same orientation. For tape plies, stack no more than 4 plies of the same orientation together.

• If possible, LSS should be balanced and symmetric about the mid-plane.

• Alternate + θº and - θº plies through the LSS except for the closest ply either side of the symmetry plane.

• Shield primary load carrying plies from exposed surfaces.

• Avoid LSS that create high inter-laminar tension stresses at free edges. Analyses to predict free edge stress and delamination strain levels are recommended to help select LSS.

3.3.4. Composites typical damages

3.3.4.1 Fatigue

Carbon composites are known to have a good fatigue resistance. Significant crack growth typically doesn't develop under 60% of static failure stress. But, under certain conditions fatigue growth can occur and lead to a catastrophic in-service failure. The main factors that can cause fatigue to the structures are:

• Environment

• Faulty design

• Type of stress (mainly compression and shear)

• Manufacturing defects

Under static load and fatigue, composites have higher resistance in tensile stress than compression stress.

A metallic material under loading will, generally, have a crack that initiates from a specific point and then propagates and leads to failure. However, in composite materials this case it is completely different. A large number of microscopic events will occur very gradually over a large volume of the material (because there is heterogeneity at macroscopic scale – matrix and reinforcement have different behaviors) (JOLLIVET, PEYRAC E LEFEBVRE 2013).

The first type of damages in laminates is usually matrix micro-cracks. The most common observation of micro cracking is cracking in 90º plies during axial loading in the 0º directions (YE 2010).

3.3.4.2 Delamination

Delamination is a type of damage that occurs through-thickness of the composite caused by inter-laminar stresses. It is not necessarily the ultimate structural failure, but it may result in fiber-matrix de-bonding and fiber rupture, which will eventually lead to the loss of structural integrity (YE 2010).

Figure 52 - Delamination during tensile test due to differences of stiffness of plies - (Jollivet, Peyrac e Lefebvre 2013)

3.3.4.3 Fibers fail

This situation is observed in metal matrix composites or thermoplastic polymer composites. Plastic deformation in the matrix causes the failure strain of the fiber to be a smaller value.

If a composite has an elastic strain to failure of the fibers which is smaller than the strain to failure of the matrix, the fibers will be the first component of the composite to fail. Then the "working strength" of the composite is just the stiffness of the composite times the strain to failure of the fibers (MICHIGAN TECH 2017).

3.3.4.4 Matrix fail

This situation is common in polymer matrix composites with low strength brittle matrix Such as Polyester, Epoxy and Bismelamides. For this case, the matrix fails at lower strain than fibers.

Strain is the significant factor in finding the failure strength of the composite when testing parallel to the fibers because both the fiber and the matrix experience the same strain (MICHIGAN TECH 2017).

When the strain in the composite reaches the fracture strain of the matrix, the matrix will fail.

3.3.4.5 Transverse Cracking fail

Transverse cracking is the most common damage mode in composite materials. An immediate effect of transverse cracking is to cause stiffness degradations of the laminate.

(Ye 2010) refers that "… cracks formed in a direction parallel to the transverse reinforcement and the thickness of the 90° plies had significant effect on the cracking process."
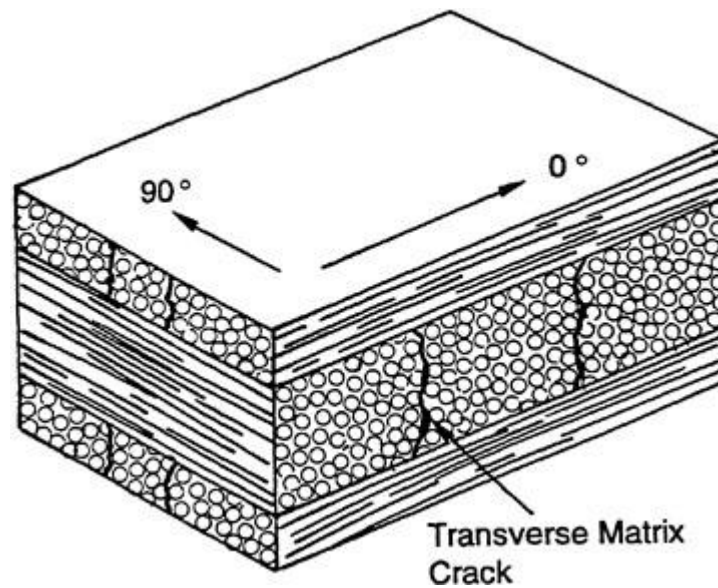
Figure 53 - Transverse matrix Cracking - (Division on Engineering and Physical Sciences; National Materials Advisory Board 1996)

3.3.4.6 Bolted Joint Failure Modes

Composite elements are usually joined through bolted connections, adhesive binding, or by adhesive/bolted hybrid joints.

With laminates joined with bolted connections, failure modes under tensile loads might happen following four different basic modes:

- cleavage
- net-tension,
- shear-out
- bearing

For these, the activation is strongly due to geometric (laminate width and thickness, end-distance, diameter of the bolt) and material properties such as: matrix and fiber type, fiber-to-load angle, laminate stacking sequence.

Bearing failure is typically present in large width and end-distance of bolted laminates. It's a laminate compressive failure caused by the movement of the bolt to crush the composite material (occurring matrix cracks) (NERILLI, MICHELE E VAIRO 2015).

Those type of failures can be observed in Figure 35:

(a) *Shearout failure* (b) *Tension failure* (c) *Bearing failure*

(d) *Cleavage — tension failure* (e) *Bolt pulling through laminate* (f) *Bolt failure*
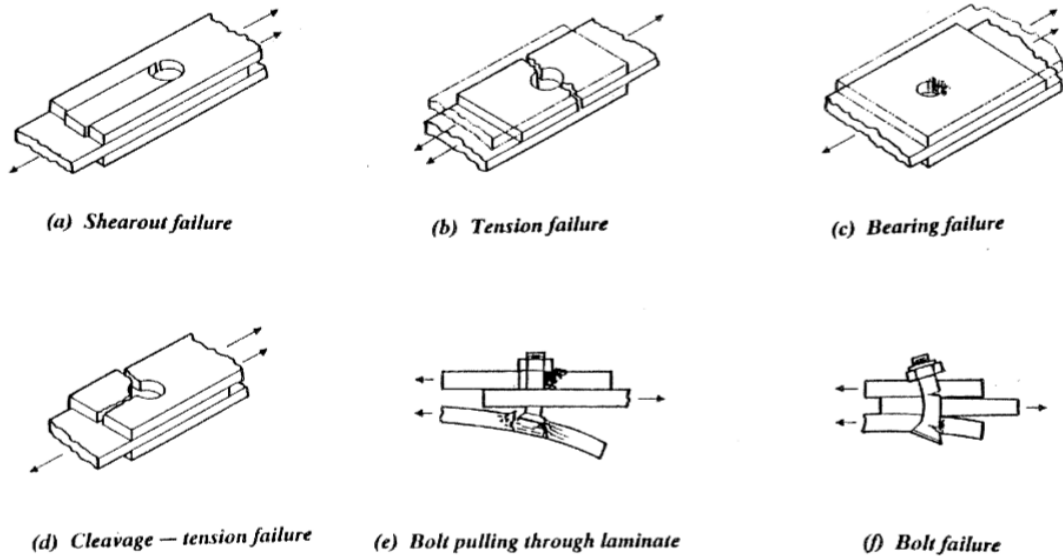
Figure 54 - Composite materials - Bolted Joint failure modes - Matthews, B. (n.d.)

Bearing stress is a compressive normal stress. The average bearing stress is the force pushing against a structure divided by an area (diameter of the hole multiplied by the the thickness of the plate).

Exact bearing stress is more complicated but for most applications, the following equation is used:

$$\sigma_b = \frac{F_b}{A_b}$$

Where:

F_b – Compressive load

A_b – Area perpendicular to F_b
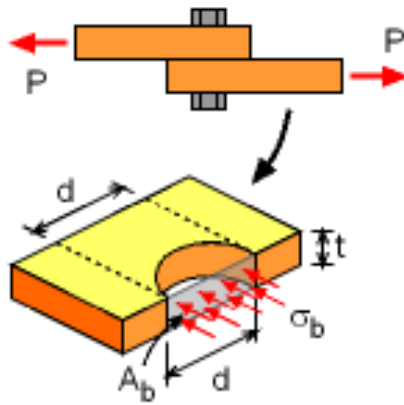
σ_b – Bearing Stress

Figure 55 - Bearing Stress - (Gramoll s.d.)
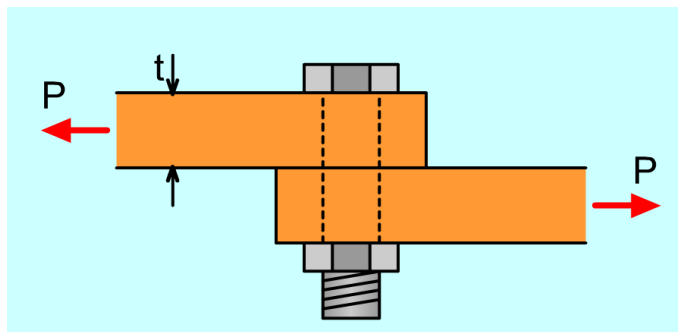
Figure 56 - Example of a screw being pulled out by 2 different surfaces - (Gramoll s.d.)

It's admitted that bearing stress is uniform but in fact, by means of experiments, the stress has an elliptical shape as shown in Figure 57:
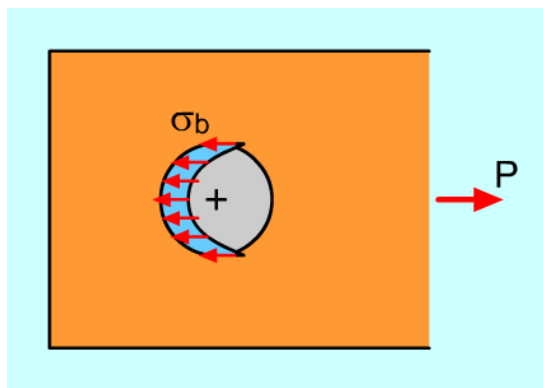
Figure 57 - Bearing Stress - Ellipse representation (Gramoll s.d.)

There is also bearing when double shear forces act on the structure. (See Figure 58 and Figure 59).
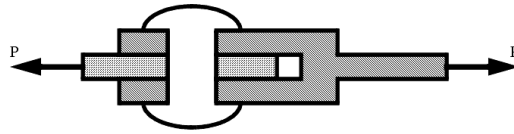
Figure 58 - Double shear - (Engineer on a disk s.d.)
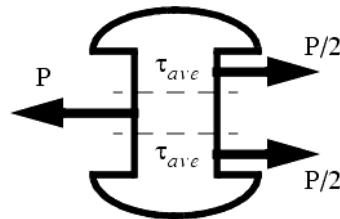
Figure 59 – Present forces in double shear - (Engineer on a disk s.d.)

For single shear forces (recalling Figure 56) the calculation of bearing stress is given by equation 99:

$$\sigma_{bearing} = \frac{Shear\ Force}{hole\ diameter\ \times\ thickness\ of\ plate} \tag{99}$$

All the bearing stress results must respect the following condition:

$$1.5\ \sigma_{Bearing} < \sigma_{allowable\ Bearing}$$

Note:

In sandwich structures, the thickness that is considered for the calculation must be the outer skin's thickness. Core thickness is not considered because bearing strength is considerably low when compared with outer skins strength.

3.3.5. Prepreg carbon fiber

As (AZOM MATERIALS) refers, prepreg carbon fiber is an adequate material for small scale production and has the following characteristics:

• It's easy to use

• It has low void content

• Good fatigue resistance

- It's easy to control the laminate thickness and of fiber volume fraction

- It has good environmental and corrosion resistance

- It's a clean process

- Better conformity and quality

- High specific modulus and strength

- Very low thermal expansion coefficient

- Enhanced vibration damping characteristic

- Low number of fabricated pieces (don't require complex machines or facilities)

Carbon fiber, compared to glass or aramid fibers, is lighter, has better behaviour when subjected to compression loads than aramid fibers and has better mechanical performances than glass fibers, even though it could have better characteristics regarding impact behaviour.

A disadvantage of prepreg process is the high material cost and labour cost if the process used is not automated (hand lay-up). This process can be easily explained taking account Figure 60.
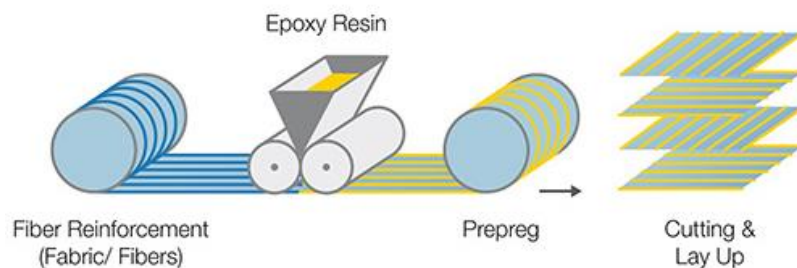
Figure 60 - Prepreg Process - (Hexion s.d.)

Fibers are impregnated with resins (generally epoxy resins) and then are stored in a certain temperature (depending on the set temperature of the resin used). Fibers of this high quality material are wetted uniformly in a resin bath.

3.3.6. Laminated plate theories

According to (J. Reddy 2004) equivalent single layer (ESL) laminated plate theories have an heterogeneous laminated plate that is treated as a statically equivalent single layer having a complex constitutive behavior, turning out to be a 2D problem.

ESL theories are developed by assuming the form of the displacement field or stress field as a linear combination of unknown functions and thickness coordinate:

$$\varphi_i(x, y, z, t) = \sum_{j=0}^{N} (z)^i \varphi_i^j(x, y, t)$$

(100)

Where:

- φ_i is the ith component of displacement or stress.

- t is time

- φ_i^j are functions to be determined

When φ_i are displacements, the equations governing φ_i^j are determined by principle of virtual displacements:

$$0 = \int_0^T (\delta U + \delta V - \delta K) dt$$

(101)

Where:

- δU is the virtual strain energy

- δV is the virtual work (related to external forces)

- δK is the virtual kinetic energy

For plate structures, the integration over the domain of the plate is represented as the product of integration over the plane of the plate and integration over the thickness of the plate. Due to the explicit nature of the assumed displacement field in the thickness coordinate:

$$\int_{vol} (.) \, dV = \int_{-h_p/2}^{h_p/2} \int_{\Omega_0} (.) \, d\Omega \, dz$$

(102)

Where:

- h_p is the total thickness of the plate

- Ω_0 is the undeformed mid-plane of the plate (chosen as reference plane)

As all functions are explicit in the thickness coordinate, the integration over the plate is also explicit, turning the problem to a 2D one. Then Euler-Lagrange equations of the principle of virtual displacements are differential equations involving dependent variables ($\varphi_i^j(x,y,t)$) and thickness-average stress resultants $\left(R_{ij}^{(m)}\right)$ that are represented by:

$$R_{ij}^{(m)} = \int_{-h_p/2}^{h_p/2} \int_{\Omega 0} (z)^m \sigma_{ij}\, dz \tag{103}$$

The classical laminated plate theory that is an extension of the Kirchhoff plate theory to laminated composite plates is the simplest ESL laminated plate theory.

It's based on the displacement field: (x, y, z, t)

$$u(x,y,z,t) = u_0(x,y,t) - z\frac{\partial w_0}{\partial x} \tag{104}$$

$$v(x,y,z,t) = v_0(x,y,t) - z\frac{\partial w_0}{\partial y} \tag{105}$$

$$w(x,y,z,t) = w_0(x,y,t) \tag{106}$$

Where:

- (u_0, v_0, w_0) are displacements along (x,y,z) coordinate directions of a point on the mid-plane (z = 0)

The displacement field infers that straight lines normal to x-y plane continue straight and normal to the mid surface after deformation. Kirchhoff assumption disregards both transverse shear and transverse normal effects (basically assuming that deformation is due to bending and in-plane stretching).

It's very important to note that ESL models have limitations that inhibit them from being used to solve the whole spectrum of composite laminate problems.

1. The accuracy of the global response predicted, deteriorates as the laminate increases its thickness.

2. They are often unable of describing with accuracy the state of stress and strain at the ply level near geometric and material discontinuities or near regions of high loading. (Areas where accurate results are needed).

3.3.6.1 Classical laminated plate theory

Assumptions

According to (REDDY 2004) in the classical laminated plate theory (CLPT) it is presumed that the Kirchhoff assumption holds:

1. Straight lines perpendicular to the midsurface before deformation remain straight after deformation.

2. Transverse normals do not elongate.

3. Transverse normal will rotate in order to stay normal to the midsurface after deformation.

Displacements and Strains

Studying a plate of total thickness h, with N orthotropic layers and the principal material coordinates $(x1^k, x2^k, x3^k)$ of the Kth lamina oriented at an angle Θ_k to the laminate coordinate: x.

It's appropriate to take xy-plane of the problem in the non-deformed mid-plane Ω_0 of the laminate (see Figure 61).
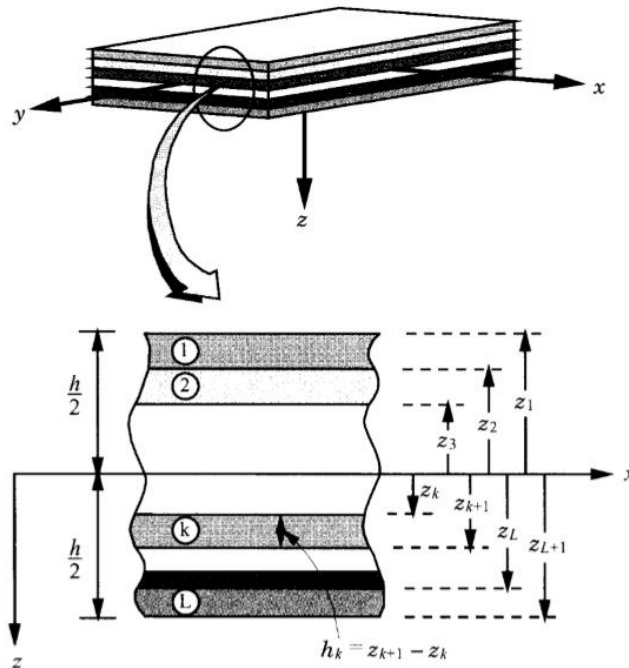
Figure 61 - Coordinate system and layer numbering used for a laminated plate - (Reddy 2004)

The K_{th} layer is positioned among the points $z = z_k$ and $z = z_{k+1}$ in the thickness direction.

Total domain of $\bar{\Omega}_0$ of the laminate is the tensor product of $\Omega_0 \times (-\frac{h}{2}, \frac{h}{2})$

The boundary of $\bar{\Omega}_0$ consists of up surface S_t $(z = -\frac{h}{2})$ and low surface S_b $(z = \frac{h}{2})$ and the edge $\bar{\Gamma} = \Gamma \times (-\frac{h}{2}, \frac{h}{2})$ of the laminate. In general, Γ is a curved surface, with outward normal $\hat{n} = n_x \hat{e}_x + n_y \hat{e}_y$. Boundary $\bar{\Gamma}$ is exposed to a mixture of generalized forces and displacements.

Certain assumptions and restrictions are made when formulating the theory:

1. Layers are perfectly bonded together - Assumption

2. Material of each layer is linearly elastic and has 3 planes of material symmetry. (orthotropic) – Restriction

3. Each Layer has uniform thickness – Restriction

4. Strains and displacement are considered small – Restriction

5. Transverse shear stresses on top and bottom surfaces of laminate are null – Restriction

Considering a material point in (x,y,z), in the undeformed laminate, that moves to point (x+u,y+v,z+w) in the deformed laminate where (u,v,w) is the vector of total displacement u, along (x,y,z) coordinates.

Then:

$$u = u\hat{e}_x + v\hat{e}_y + w\hat{e}_z \tag{107}$$

Where $(\hat{e}_x, \hat{e}_y, \hat{e}_z)$ are unit vectors along the (x,y,z) system.

Kirchhoff hypothesis requires the displacements (u,v,w) to be:

$$u(x,y,z,t) = u_0(x,y,t) - z\,\frac{\partial w0}{\partial x} \tag{108}$$

$$v(x,y,z,t) = v_0(x,y,t) - z\,\frac{\partial w0}{\partial y} \tag{109}$$

$$w(x,y,z,t) = w_0\,(x,y,t) \tag{110}$$

Where (u_0,v_0,w_0) are movements on the coordinate lines of a material point on the xy-plane. Note that the form of displacement field (u) permits a reduction of the 3D problem to a problem of a single membrane at z=0 (mid-plane). (See Figure 62)

As soon as the mid-plane displacements (u_0,v_0,w_0) are known, the displacements of any point (x,y,z) in the 3D continuum can be determined using the above equations.
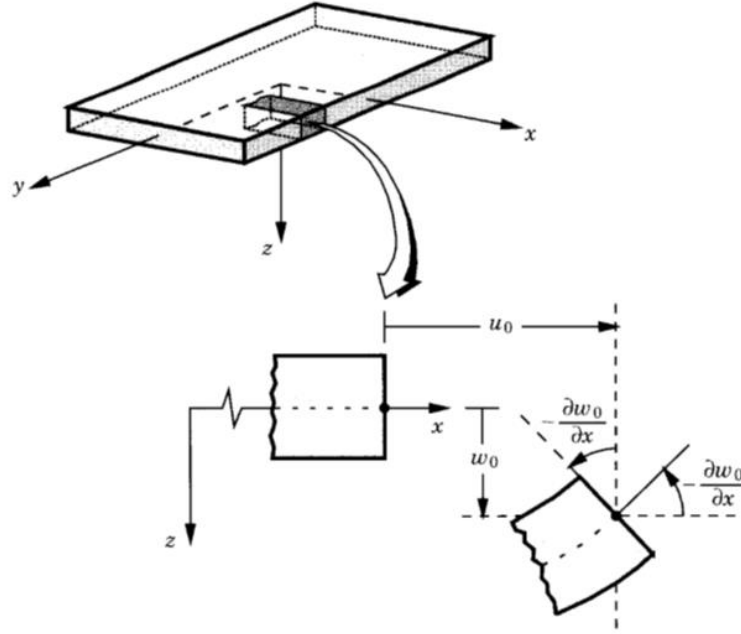
Figure 62 – Un-deformed and deformed geometries of an edge of a plate under Kirchhoff assumptions - (Reddy 2004)

Strains related with displacement field might be calculated using nonlinear strain-displacement or linear strain-displacement relations.

Nonlinear strains are given by:

$$E_{xx} = \frac{\partial u}{\partial x} + \frac{1}{2}\left[\left(\frac{\partial u}{\partial x}\right)^2 + \left(\frac{\partial v}{\partial x}\right)^2 + \left(\frac{\partial w}{\partial x}\right)^2\right]$$

$$E_{yy} = \frac{\partial v}{\partial y} + \frac{1}{2}\left[\left(\frac{\partial u}{\partial y}\right)^2 + \left(\frac{\partial v}{\partial y}\right)^2 + \left(\frac{\partial w}{\partial y}\right)^2\right]$$

$$E_{zz} = \frac{\partial w}{\partial z} + \frac{1}{2}\left[\left(\frac{\partial u}{\partial z}\right)^2 + \left(\frac{\partial v}{\partial z}\right)^2 + \left(\frac{\partial w}{\partial z}\right)^2\right]$$

$$E_{xy} = \frac{1}{2}\left(\frac{\partial u}{\partial y} + \frac{\partial v}{\partial x} + \frac{\partial u}{\partial x}\frac{\partial u}{\partial y} + \frac{\partial v}{\partial x}\frac{\partial v}{\partial y} + \frac{\partial w}{\partial x}\frac{\partial w}{\partial y}\right)$$

$$E_{xz} = \frac{1}{2}\left(\frac{\partial u}{\partial z} + \frac{\partial v}{\partial x} + \frac{\partial u}{\partial x}\frac{\partial u}{\partial z} + \frac{\partial v}{\partial x}\frac{\partial v}{\partial z} + \frac{\partial w}{\partial x}\frac{\partial w}{\partial z}\right)$$

$$E_{yz} = \frac{1}{2}\left(\frac{\partial u}{\partial z} + \frac{\partial v}{\partial y} + \frac{\partial u}{\partial y}\frac{\partial u}{\partial z} + \frac{\partial v}{\partial y}\frac{\partial v}{\partial z} + \frac{\partial w}{\partial y}\frac{\partial w}{\partial z}\right)$$

If the constituents of displacement gradients are of the order ϵ:

$$\frac{\partial u}{\partial x}, \frac{\partial u}{\partial y}, \frac{\partial v}{\partial x}, \frac{\partial v}{\partial y}, \frac{\partial w}{\partial z} = O(\epsilon) \tag{111}$$

With the small strain assumption it's possible to imply that terms of the order ϵ^2 are insignificant in the strains.

Terms of order $\epsilon^{2:}$ are:

$$\left(\frac{\partial u}{\partial x}\right)^2, \left(\frac{\partial u}{\partial y}\right)^2, \left(\frac{\partial u}{\partial z}\right)^2, \left(\frac{\partial u}{\partial x}\right)\left(\frac{\partial u}{\partial y}\right), \left(\frac{\partial u}{\partial x}\right)\left(\frac{\partial u}{\partial z}\right), \left(\frac{\partial u}{\partial y}\right)\left(\frac{\partial u}{\partial z}\right),$$

$$\left(\frac{\partial v}{\partial x}\right)^2, \left(\frac{\partial v}{\partial y}\right)^2, \left(\frac{\partial v}{\partial z}\right)^2, \left(\frac{\partial v}{\partial x}\right)\left(\frac{\partial v}{\partial y}\right), \left(\frac{\partial v}{\partial x}\right)\left(\frac{\partial v}{\partial z}\right), \left(\frac{\partial v}{\partial y}\right)\left(\frac{\partial v}{\partial z}\right),$$

$$\left(\frac{\partial w}{\partial x}\right)\left(\frac{\partial w}{\partial z}\right), \left(\frac{\partial w}{\partial y}\right)\left(\frac{\partial w}{\partial z}\right), \left(\frac{\partial w}{\partial z}\right)^2$$

If the rotations $\frac{\partial w0}{\partial x}$ and $\frac{\partial w0}{\partial y}$ of transverse normal are small (10/15°), then the next terms are smaller (but not insignificant when compared to ϵ).

$$\left(\frac{\partial w}{\partial x}\right)^2, \left(\frac{\partial w}{\partial y}\right)^2, \left(\frac{\partial w}{\partial x}\right)\left(\frac{\partial w}{\partial y}\right) \tag{112}$$

And they should be incorporated in strain-displacement relations.

For small strains and medium rotation (10/15°), strain-displacement relations take the shape:

$$\varepsilon_{xx} = \frac{\partial u}{\partial x} + \frac{1}{2}\left(\frac{\partial w}{\partial x}\right)^2 \tag{113}$$

$$\varepsilon_{xy} = \frac{1}{2}\left(\frac{\partial u}{\partial y} + \frac{\partial v}{\partial x} + \frac{\partial w}{\partial x}\frac{\partial w}{\partial y}\right) \tag{114}$$

$$\varepsilon_{xz} = \frac{1}{2}\left(\frac{\partial u}{\partial z} + \frac{\partial w}{\partial x}\right) \tag{115}$$

$$\varepsilon_{yy} = \frac{\partial v}{\partial y} + \frac{1}{2}\left(\frac{\partial w}{\partial y}\right)^2 \tag{116}$$

$$\varepsilon_{yz} = \frac{1}{2}\left(\frac{\partial v}{\partial z} + \frac{\partial w}{\partial y}\right) \tag{117}$$

$$\varepsilon_{zz} = \frac{\partial w}{\partial z} \tag{118}$$

Where for this distinct case of geometric nonlinearity (small strains but moderate rotations), notation ε_{ij} is used instead of E_{ij} and correspondent stresses will be symbolised by σ_{ij}.

For the displacement field defined in equation 110. $\frac{\partial w}{\partial z} = 0$. Regarding assumptions in equations 111 to 112 the strains in equations 113 to 118 reduce to:

$$\varepsilon_{xx} = \frac{\partial u_0}{\partial x} + \frac{1}{2}\left(\frac{\partial w_0}{\partial x}\right)^2 - z\left(\frac{\partial^2 w_0}{\partial x^2}\right) \tag{119}$$

$$\varepsilon_{xy} = \frac{1}{2}\left(\frac{\partial u_0}{\partial y} + \frac{\partial v_0}{\partial x} + \frac{\partial w_0}{\partial x}\frac{\partial w_0}{\partial y}\right) - z\left(\frac{\partial^2 w_0}{\partial x \partial y}\right) \tag{120}$$

$$\varepsilon_{yy} = \frac{\partial v_0}{\partial y} + \frac{1}{2}\left(\frac{\partial w_0}{\partial y}\right)^2 - z\left(\frac{\partial^2 w_0}{\partial y^2}\right) \tag{121}$$

$$\varepsilon_{xz} = \frac{1}{2}\left(-\frac{\partial w_0}{\partial x} + \frac{\partial w_0}{\partial x}\right) = 0 \tag{122}$$

$$\varepsilon_{yz} = \frac{1}{2}\left(-\frac{\partial w_0}{\partial y} + \frac{\partial w_0}{\partial y}\right) = 0 \tag{123}$$

$$\varepsilon_{zz} = 0 \tag{124}$$

Note: this strains are referred as Von Kármán Strains, and the associated plate theory is termed the von Kármán plate theory. Like in the classical plate theory, $(\varepsilon_{xz}, \varepsilon_{yz}, \varepsilon_{zz}) = 0$.

First three strains (equations 119 to 121) have the form:

$$\begin{Bmatrix} \varepsilon_{xx} \\ \varepsilon_{yy} \\ \gamma_{xy} \end{Bmatrix} = \begin{Bmatrix} \varepsilon_{xx}^{(0)} \\ \varepsilon_{yy}^{(0)} \\ \gamma_{xy}^{(0)} \end{Bmatrix} + z \begin{Bmatrix} \varepsilon_{xx}^{(1)} \\ \varepsilon_{yy}^{(1)} \\ \gamma_{xy}^{(1)} \end{Bmatrix} \tag{125}$$

$$\{\varepsilon^0\} = \begin{Bmatrix} \varepsilon_{xx}^{(0)} \\ \varepsilon_{yy}^{(0)} \\ \gamma_{xy}^{(0)} \end{Bmatrix} = \begin{Bmatrix} \dfrac{\partial u_0}{\partial x} + \dfrac{1}{2}\left(\dfrac{\partial w_0}{\partial x}\right)^2 \\ \dfrac{\partial v_0}{\partial y} + \dfrac{1}{2}\left(\dfrac{\partial w_0}{\partial y}\right)^2 \\ \dfrac{\partial v_0}{\partial y} + \dfrac{\partial v_0}{\partial x} + \dfrac{\partial w_0}{\partial x}\dfrac{\partial w_0}{\partial y} \end{Bmatrix} \tag{126}$$

$$\{\varepsilon^1\} = \begin{Bmatrix} \varepsilon_{xx}^{(1)} \\ \varepsilon_{yy}^{(1)} \\ \gamma_{xy}^{(1)} \end{Bmatrix} = \begin{Bmatrix} -\left(\dfrac{\partial^2 w_0}{\partial x^2}\right) \\ -\left(\dfrac{\partial^2 w_0}{\partial y^2}\right) \\ -z\dfrac{\partial^2 w_0}{\partial x \partial y} \end{Bmatrix} \tag{127}$$

Where:

- $(\varepsilon_{xx}{}^{(0)}, \varepsilon_{yy}{}^{(0)}, \gamma_{xy}{}^{(0)})$ are membrane strains

- $(\varepsilon_{xx}{}^{(1)}, \varepsilon_{yy}{}^{(1)}, \gamma_{xy}{}^{(1)})$ are flexural (bending) strains – Curvatures

When displacements (u_0, v_0, w_0) of the mid-plane are identified, strains at any point (x,y,z) in the plate can be calculated using equations: 125 to 127.

From equation 125, all strain components vary linearly through the laminate thickness and they are independent of the material variations through the laminate thickness.

Lamina constitutive relations

For a laminate composed of orthotropic layers with their $x_1 x_2$ – plane oriented arbitrarily with respect to the xy-plane $(x_3 = z)$, the transverse shear stresses $(\sigma_{xz}, \sigma_{yz})$ are also zero.

Since $\varepsilon_{zz} = 0$, transverse normal stress σ_{zz}, even though not zero, doesn't appear in virtual work part and hence in the equations of motion. Therefore it amounts to ignore the transverse normal stress (REDDY 2004).
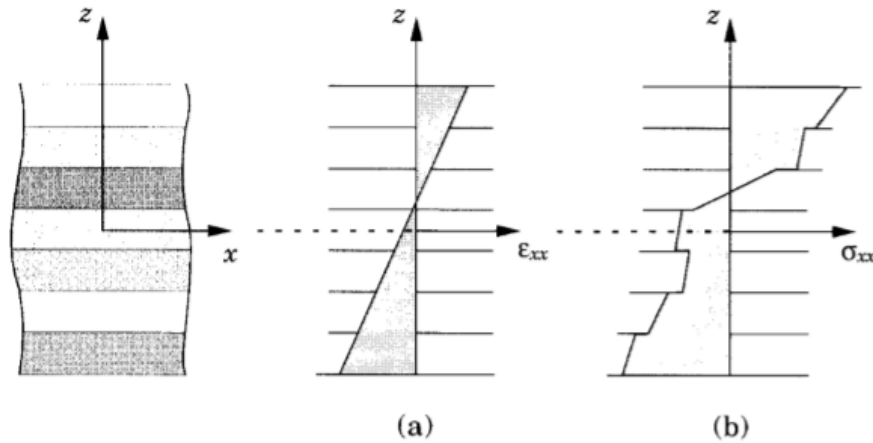
Figure 63 - Variations of strains and stresses through layer and laminate thicknesses. (a) Variation of typical in-plane strain. (b) Variation of corresponding stress - (Reddy 2004)

Strain varies linearly across the thickness but stiffness properties are discontinuous from one layer to the next (KUMAR 1998).

Hence, it's a case (in theory) of both plane strain and plane stress. Nevertheless, a thin or moderately thick plate is in a state of plane stress since the thickness is insignificant compared to the in-plane dimensions.

Linear constitutive relations for the kth orthotropic lamina in the principal material coordinates of a lamina are represented by:

$$\begin{Bmatrix} \sigma_1 \\ \sigma_2 \\ \sigma_6 \end{Bmatrix}^k = \begin{bmatrix} Q_{11} & Q_{12} & 0 \\ Q_{12} & Q_{22} & 0 \\ 0 & 0 & Q_{66} \end{bmatrix}^{(k)} \begin{Bmatrix} \varepsilon_1 - \alpha_1 \Delta T \\ \varepsilon_2 - \alpha_2 \Delta T \\ \varepsilon_6 \end{Bmatrix} - \begin{bmatrix} 0 & 0 & e_{31} \\ 0 & 0 & e_{32} \\ 0 & 0 & 0 \end{bmatrix}^{(k)} \begin{Bmatrix} \dot{\varepsilon}_1 \\ \dot{\varepsilon}_2 \\ \dot{\varepsilon}_3 \end{Bmatrix}^{(k)} \tag{128}$$

Where:

- $Q_{ij}^{(k)}$ are the plane stress-reduced stiffness

- $e_{ij}^{(k)}$ are piezoelectric moduli of the kth lamina

- $(\sigma_1, \varepsilon_1, \dot{\varepsilon})$ are the stress, strain and electric field components (referred to the coordinate system (x_1, x_2, x_3)

- α_1 and α_2 are the coefficients of thermal expansion along x_1 and x_2 directions

- ΔT is the temperature increment for a reference state

Note: "Piezoelectric Effect is the ability of certain materials to generate an electric charge in response to applied mechanical stress." (Nano Motion s.d.)

If piezoelectric effects are not existent, the part that contains piezoelectric moduli e_{ij} should be omitted.

$$Q_{11} = \frac{E_1}{1 - \nu_{12}\nu_{21}} \qquad Q_{12} = \frac{\nu_{12}E_2}{1 - \nu_{12}\nu_{21}} = \frac{\nu_{21}E_1}{1 - \nu_{12}\nu_{21}} \qquad Q_{22} = \frac{E_2}{1 - \nu_{12}\nu_{21}} \qquad Q_{66} = G_{12}$$

Where:

E₁ E₂ - Young's modulus in 1 and 2 directions

ν_{12} – Poisson's ratio for transverse strain in the j-direction when stressed in the *i*-direction.

G₁₂ – Shear modulus in the 1-2 plane

Reminding the fact that the laminate has several orthotropic layers, with their material axis oriented randomly with respect to the laminate coordinates, the constitutive equations of each layer must be converted from the principal material coordinates of a layer (x_1, x_2, x_3) to the laminate coordinates (x, y, z). Considering that z axis and x_3 are coincident, the relations of the two coordinate systems are:

$$\begin{Bmatrix} x_1 \\ x_2 \\ x_3 \end{Bmatrix} = \begin{bmatrix} \cos\theta & \sin\theta & 0 \\ -\sin\theta & \cos\theta & 0 \\ 0 & 0 & 1 \end{bmatrix} \begin{Bmatrix} x \\ y \\ z \end{Bmatrix} = [L] \begin{Bmatrix} x \\ y \\ z \end{Bmatrix} \tag{129}$$

$$\begin{Bmatrix} x \\ y \\ z \end{Bmatrix} = \begin{bmatrix} \cos\theta & -\sin\theta & 0 \\ \sin\theta & \cos\theta & 0 \\ 0 & 0 & 1 \end{bmatrix} \begin{Bmatrix} x_1 \\ x_2 \\ x_3 \end{Bmatrix} = [L]^T \begin{Bmatrix} x_1 \\ x_2 \\ x_3 \end{Bmatrix} \tag{130}$$
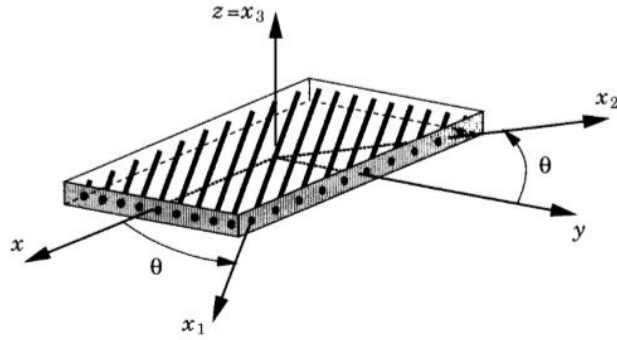
Figure 64 - Lamina with material and problem coordinate systems - (Reddy 2004)

Proceeding with the same idea, relating stresses with different coordinate system can be expressed as follows:

$$
\begin{Bmatrix} \sigma_{xx} \\ \sigma_{yy} \\ \sigma_{zz} \\ \sigma_{yz} \\ \sigma_{xz} \\ \sigma_{xy} \end{Bmatrix} = \begin{bmatrix} \cos^2\theta & \sin^2\theta & 0 & 0 & 0 & -\sin2\theta \\ \sin^2\theta & \cos^2\theta & 0 & 0 & 0 & \sin2\theta \\ 0 & 0 & 1 & 0 & 0 & 0 \\ 0 & 0 & 0 & \cos\theta & \sin\theta & 0 \\ 0 & 0 & 0 & -\sin\theta & \cos\theta & 0 \\ \sin\theta\cos\theta & -\sin\theta\cos\theta & 0 & 0 & 0 & \cos^2\theta - \sin^2\theta \end{bmatrix} \begin{Bmatrix} \sigma_1 \\ \sigma_2 \\ \sigma_3 \\ \sigma_4 \\ \sigma_5 \\ \sigma_6 \end{Bmatrix} \quad (131)
$$

Inverse relation:

$$
\begin{Bmatrix} \sigma_1 \\ \sigma_2 \\ \sigma_3 \\ \sigma_4 \\ \sigma_5 \\ \sigma_6 \end{Bmatrix} = \begin{bmatrix} \cos^2\theta & \sin^2\theta & 0 & 0 & 0 & \sin2\theta \\ \sin^2\theta & \cos^2\theta & 0 & 0 & 0 & -\sin2\theta \\ 0 & 0 & 1 & 0 & 0 & 0 \\ 0 & 0 & 0 & \cos\theta & -\sin\theta & 0 \\ 0 & 0 & 0 & \sin\theta & \cos\theta & 0 \\ -\sin\theta\cos\theta & \sin\theta\cos\theta & 0 & 0 & 0 & \cos^2\theta - \sin^2\theta \end{bmatrix} \begin{Bmatrix} \sigma_{xx} \\ \sigma_{yy} \\ \sigma_{zz} \\ \sigma_{yz} \\ \sigma_{xz} \\ \sigma_{xy} \end{Bmatrix} \quad (132)
$$

And now for strains:

$$
\begin{Bmatrix} \varepsilon_{xx} \\ \varepsilon_{yy} \\ \varepsilon_{zz} \\ 2\varepsilon_{yz} \\ 2\varepsilon_{xz} \\ 2\varepsilon_{xy} \end{Bmatrix} = \begin{bmatrix} \cos^2\theta & \sin^2\theta & 0 & 0 & 0 & -\sin\theta\cos\theta \\ \sin^2\theta & \cos^2\theta & 0 & 0 & 0 & \sin2\theta\cos\theta \\ 0 & 0 & 1 & 0 & 0 & 0 \\ 0 & 0 & 0 & \cos\theta & \sin\theta & 0 \\ 0 & 0 & 0 & -\sin\theta & \cos\theta & 0 \\ \sin2\theta & -\sin2\theta & 0 & 0 & 0 & \cos^2\theta - \sin^2\theta \end{bmatrix} \begin{Bmatrix} \varepsilon_1 \\ \varepsilon_2 \\ \varepsilon_3 \\ \varepsilon_4 \\ \varepsilon_5 \\ \varepsilon_6 \end{Bmatrix} \quad (133)
$$

Inverse relation:

$$\begin{Bmatrix} \varepsilon_1 \\ \varepsilon_2 \\ \varepsilon_3 \\ \varepsilon_4 \\ \varepsilon_5 \\ \varepsilon_6 \end{Bmatrix} = \begin{bmatrix} \cos^2\theta & \sin^2\theta & 0 & 0 & 0 & \sin\theta\cos\theta \\ \sin^2\theta & \cos^2\theta & 0 & 0 & 0 & -\sin2\theta\cos\theta \\ 0 & 0 & 1 & 0 & 0 & 0 \\ 0 & 0 & 0 & \cos\theta & -\sin\theta & 0 \\ 0 & 0 & 0 & \sin\theta & \cos\theta & 0 \\ -\sin2\theta & \sin2\theta & 0 & 0 & 0 & \cos^2\theta-\sin^2\theta \end{bmatrix} \begin{Bmatrix} \varepsilon_{xx} \\ \varepsilon_{yy} \\ \varepsilon_{zz} \\ 2\varepsilon_{yz} \\ 2\varepsilon_{xz} \\ 2\varepsilon_{xy} \end{Bmatrix} \qquad (134)$$

If electric field vector and temperature increment is not considered, stress-strain relations for (x,y,z) coordinate system are:

$$\begin{Bmatrix} \sigma_{xx} \\ \sigma_{yy} \\ \sigma_{xy} \end{Bmatrix}^{k} = \begin{bmatrix} \overline{Q_{11}} & \overline{Q_{12}} & \overline{Q_{16}} \\ \overline{Q_{12}} & \overline{Q_{22}} & \overline{Q_{26}} \\ \overline{Q_{16}} & \overline{Q_{26}} & \overline{Q_{66}} \end{bmatrix}^{(k)} \begin{Bmatrix} \varepsilon_{xx} \\ \varepsilon_{yy} \\ \gamma_{xy} \end{Bmatrix} \qquad (135)$$

Where:

- $\overline{Q_{11}} = Q_{11}cos^4\theta + 2(Q_{12} + 2Q_{66})sin^2\theta cos^2\theta + Q_{22}sin^4\theta$
- $\overline{Q_{12}} = (Q_{11} + Q_{22} - 4Q_{66})\sin^2\theta cos^2\theta + Q_{12}(cos^4\theta + sin^4\theta)$
- $\overline{Q_{22}} = Q_{11}sin^4\theta + 2(Q_{12} + 2Q_{66})\sin^2\theta cos^2\theta + Q_{22}(cos^4\theta)$
- $\overline{Q_{16}} = (Q_{11} - Q_{12} - 2Q_{66})\cos^3\theta sin\theta + (Q_{12} - Q_{22} + 2Q_{66})\sin^3\theta cos\theta$
- $\overline{Q_{26}} = (Q_{11} - Q_{12} - 2Q_{66})\sin^3\theta cos\theta + (Q_{12} - Q_{22} + 2Q_{66})\cos^3\theta sin\theta$
- $\overline{Q_{66}} = (Q_{11} + Q_{22} - 2Q_{12} - 2Q_{66})\sin^2\theta cos^2\theta + Q_{66}(sin^4\theta + cos^4\theta)$
- θ is the angle measured counter clockwise from x-coordinate to the x_1 coordinate.

Laminate constitutive equations

In this part, constitutive equations that relate the force and moment resultants to the strains of a laminate are derived – see Figure 65 (REDDY 2004).
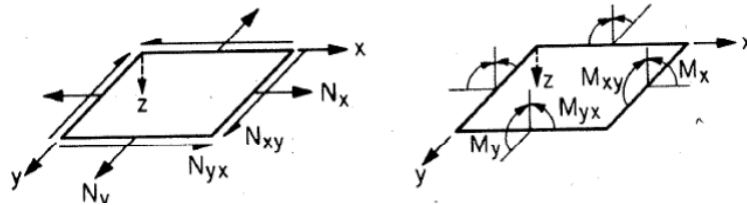
Figure 65 – Resultant forces and moments (Active Structures Laboratory s.d.)

$$\begin{Bmatrix} N_{xx} \\ N_{yy} \\ N_{xy} \end{Bmatrix} = \int_{-h/2}^{h/2} \begin{Bmatrix} \sigma_{xx} \\ \sigma_{yy} \\ \sigma_{xy} \end{Bmatrix} dz, \quad \begin{Bmatrix} M_{xx} \\ M_{yy} \\ M_{xy} \end{Bmatrix} = \int_{-h/2}^{h/2} \begin{Bmatrix} \sigma_{xx} \\ \sigma_{yy} \\ \sigma_{xy} \end{Bmatrix} zdz \qquad (136)$$

Once again, piezoelectric and temperature effects are not considered. Strains are continuous through the thickness but stresses are not, as the material coefficients change through the thickness. (Each lamina).

Then, the integration of stresses through the laminate thickness requires lamina-wise integration.

Force Resultants are given by:

$$
\begin{Bmatrix} N_{xx} \\ N_{yy} \\ N_{xy} \end{Bmatrix} = \begin{bmatrix} A_{11} & A_{12} & A_{16} \\ A_{12} & A_{22} & A_{26} \\ A_{16} & A_{26} & A_{66} \end{bmatrix} \begin{Bmatrix} \varepsilon_{xx}^{(0)} \\ \varepsilon_{yy}^{(0)} \\ \gamma_{xy}^{(0)} \end{Bmatrix} + \begin{bmatrix} B_{11} & B_{12} & B_{16} \\ B_{12} & B_{22} & B_{26} \\ B_{16} & B_{26} & B_{66} \end{bmatrix} \begin{Bmatrix} \varepsilon_{xx}^{(1)} \\ \varepsilon_{yy}^{(1)} \\ \gamma_{xy}^{(1)} \end{Bmatrix}
\tag{137}
$$

$$
\begin{Bmatrix} M_{xx} \\ M_{yy} \\ M_{xy} \end{Bmatrix} = \sum_{k=1}^{N} \int_{z_k}^{z_{k+1}} \begin{Bmatrix} \sigma_{xx} \\ \sigma_{yy} \\ \sigma_{xy} \end{Bmatrix} z \, dz = \sum_{k=1}^{N} \int_{z_k}^{z_{k+1}} \begin{bmatrix} \overline{Q}_{11} & \overline{Q}_{12} & \overline{Q}_{16} \\ \overline{Q}_{12} & \overline{Q}_{22} & \overline{Q}_{26} \\ \overline{Q}_{16} & \overline{Q}_{26} & \overline{Q}_{66} \end{bmatrix}^{(k)} \begin{Bmatrix} \varepsilon_{xx}^{(0)} + z\varepsilon_{xx}^{(1)} \\ \varepsilon_{yy}^{(0)} + z\varepsilon_{yy}^{(1)} \\ \gamma_{xy}^{(0)} + z\gamma_{xy}^{(1)} \end{Bmatrix} z \, dz
\tag{138}
$$

$$
\begin{Bmatrix} M_{xx} \\ M_{yy} \\ M_{xy} \end{Bmatrix} = \begin{bmatrix} B_{11} & B_{12} & B_{16} \\ B_{12} & B_{22} & B_{26} \\ B_{16} & B_{26} & B_{66} \end{bmatrix} \begin{Bmatrix} \varepsilon_{xx}^{(0)} \\ \varepsilon_{yy}^{(0)} \\ \gamma_{xy}^{(0)} \end{Bmatrix} + \begin{bmatrix} D_{11} & D_{12} & D_{16} \\ D_{12} & D_{22} & D_{26} \\ D_{16} & D_{26} & D_{66} \end{bmatrix} \begin{Bmatrix} \varepsilon_{xx}^{(1)} \\ \varepsilon_{yy}^{(1)} \\ \gamma_{xy}^{(1)} \end{Bmatrix}
\tag{139}
$$

Where:

- A_{ij} are extensional stiffnesses
- D_{ij} are bending stiffnesses
- B_{ij} are bending-extensional coupling stiffnesses
- M_{kk} are moments applied (see Figure 65)
- N_{kk} are normal forces applied (see Figure 65)

$$
(A_{ij}, B_{ij}, D_{ij}) = \int_{-h/2}^{h/2} \overline{Q}_{ij}(1, z, z^2) dz = \sum_{k=1}^{N} \int_{z_k}^{z_{k+1}} \overline{Q}_{ij}^{(k)}(1, z, z^2) dz
\tag{140}
$$

$$
A_{ij} = \sum_{k=1}^{N} \overline{Q}_{ij}^{(k)}(z_{k+1} - z_k)
\tag{141}
$$

$$\text{Bij} = \frac{1}{2} \sum_{k=1}^{N} \bar{Q}_{ij}^{(k)} \left(z_{k+1}^{2} - z_{k}^{2} \right) \tag{142}$$

$$\text{Dij} = \frac{1}{3} \sum_{k=1}^{N} \bar{Q}_{ij}^{(k)} \left(z_{k+1}^{3} - z_{k}^{3} \right) \tag{143}$$

Where z_i is the thickness considered from the middle plane to the extreme of zth layer – see Figure 66.
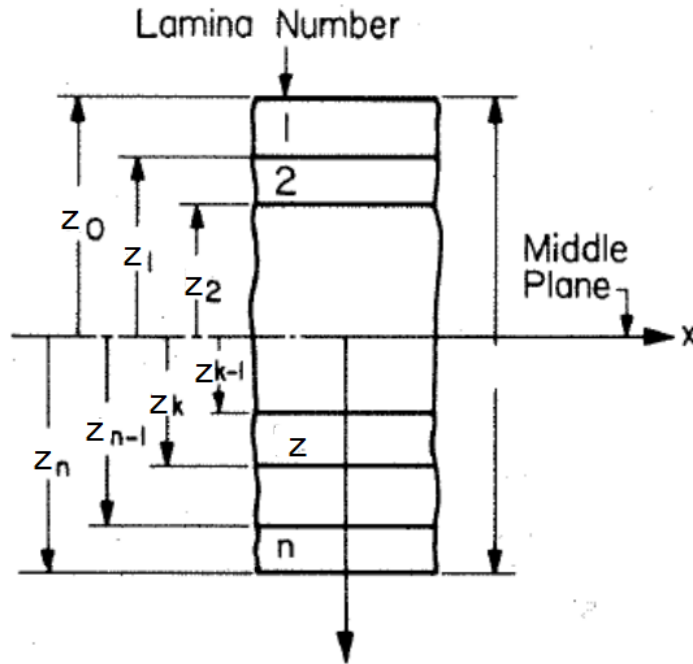
Figure 66 – Laminate numeration - (Active Structures Laboratory s.d.)

These equations can be arranged in a more compact form:

$$\begin{Bmatrix} \{N\} \\ \{M\} \end{Bmatrix} = \begin{bmatrix} [A] & [B] \\ [B] & [D] \end{bmatrix} \begin{Bmatrix} \{\varepsilon^0\} \\ \{\varepsilon^1\} \end{Bmatrix}$$

Where:

- $\{\varepsilon^0\}$ and $\{\varepsilon^1\}$ are vectors of the membrane and bending strains
- $[A], [B]$ and $[D]$ are 3x3 symmetric matrices of laminate coefficients

Single layer orthotropic laminate – Membrane properties

The main objective of this sub-chapter is to obtain values of E_1, E_2, v_{yx}, v_{xy} and G_{xy} for membrane and bending that will be later used in MATLAB software to calculate deflections and stresses – see chapter 5.2.1.

In these cases, the laminate constituted by several orthotropic layers is then considered as a single layer orthotropic laminate.

Membrane properties are related with deformations in the plane of the plate.

Recalling that:

$$Q_{12} = \frac{v_{12}E_2}{1 - v_{12}v_{21}} \tag{144}$$

And

$$Q_{22} = \frac{E_2}{1 - v_{12}v_{21}} \tag{145}$$

Then, inverting above equations we obtain:

$$E_2 = \frac{Q_{12}\,(1 - v_{12}v_{21})}{v_{12}} \tag{146}$$

$$E_2 = Q_{22}(1 - v_{12}v_{21}) \tag{147}$$

Equalling both equations:

$$\frac{Q_{12}\,(1 - v_{12}v_{21})}{v_{12}} = Q_{22}(1 - v_{12}v_{21}) \tag{148}$$

From equations 141 to 143, for a single specially orthotropic layer of thickness h the laminate stiffnesses are:

$$A_{11} = Q_{11}h \qquad\qquad A_{22} = Q_{22}h \qquad\qquad A_{12} = Q_{12}h$$

$$A_{66} = Q_{66}h \qquad\qquad A_{44} = Q_{44}h \qquad\qquad A_{55} = Q_{55}h$$

$$D_{11} = \frac{Q_{11}h^3}{12} \qquad\qquad D_{12} = \frac{Q_{12}h^3}{12} \qquad\qquad D_{22} = \frac{Q_{22}h^3}{12}$$

$$D_{66} = \frac{Q_{66}h^3}{12} \qquad\qquad A_{16} = A_{26} = 0 \qquad\qquad B_{ij} = 0$$

Note: For symmetric laminates **B$_{ij}$** (bending-extensional coupling stiffnesses) are zero.

If we substitute in equation 148, $\boldsymbol{Q_{12}}$ and $\boldsymbol{Q_{22}}$ by the following equations:

$$Q_{12} = \frac{A_{12}}{h} \qquad\qquad\qquad\qquad Q_{22} = \frac{A_{22}}{h}$$

We obtain:

$$\frac{Q_{12}\,(1 - \nu_{12}\nu_{21})}{\nu_{12}} = Q_{22}(1 - \nu_{12}\nu_{21}) \tag{149}$$

$$\frac{A_{12}(1 - \nu_{12}\nu_{21})}{h\,\nu_{12}} = \frac{A_{22}}{h}(1 - \nu_{12}\nu_{21}) \tag{150}$$

Simplifying:

$$\frac{A_{12}}{\nu_{12}} = A_{22}$$

$$\boldsymbol{\nu_{12}} = \frac{\boldsymbol{A_{12}}}{\boldsymbol{A_{22}}} \tag{151}$$

.

Using the same logic but for E1:

$$Q_{11} = \frac{E_1}{1 - \nu_{12}\nu_{21}} \qquad\qquad Q_{12} = \frac{\nu_{21}E_1}{1 - \nu_{12}\nu_{21}}$$

$$E_1 = Q_{11}(1 - \nu_{12}\nu_{21}) \tag{152}$$

$$E_1 = \frac{1 - \nu_{12}\nu_{21}}{\nu_{21}} Q_{12} \tag{154}$$

Equalling both equations:

$$\frac{1 - v_{12}v_{21}}{v_{21}} Q_{12} = Q_{11}(1 - v_{12}v_{21})$$

If we substitute Q_{12} and Q_{22} by the following equations:

$$Q_{12} = \frac{A_{12}}{h} \qquad\qquad Q_{22} = \frac{A_{22}}{h}$$

We obtain:

$$\frac{1 - v_{12}v_{21}}{v_{21}} \frac{A_{12}}{h} = \frac{A_{11}}{h} (1 - v_{12}v_{21})$$

Simplifying:

$$A_{12} = A_{11}v_{21} \tag{155}$$

$$v_{21} = \frac{A_{12}}{A_{11}} \tag{156}$$

Note: $A_{12} = A_{21}$

Remembering that:

$$A_{11} = Q_{11}h$$

Then:

$$Q_{11} = \frac{A_{11}}{h}$$

Substituting Q_{11}, v_{21} and v_{12} in eq. 152:

$$E_1 = \frac{A_{11}}{h}(1 - \frac{A_{12}}{A_{22}}\frac{A_{12}}{A_{11}})$$

$$E_1 = \frac{A_{11}}{h} - \frac{A_{11}A_{12}^2}{A_{11}A_{22}h}$$

Lastly:

$$E_1 = \frac{A_{22}A_{11} - A_{12}^2}{A_{22}h} \tag{157}$$

Using the same thoughts to calculate E_2:

$$E_2 = Q_{22}(1 - \nu_{12}\nu_{21})$$

$$= \frac{A_{22}}{h}\left(1 - \frac{A_{12}}{A_{22}}\frac{A_{12}}{A_{11}}\right)$$

$$E_2 = \frac{A_{22}A_{11} - A_{12}^2}{A_{11}h} \tag{158}$$

At last, recalling that:

$$Q_{66} = \frac{A_{66}}{h}$$

$$G_{12} = Q_{66}$$

We obtain:

$$G_{12} = \frac{A_{66}}{h}$$

And summing up, all the homogenised membrane properties are:

$$E_1 = \frac{A_{22}A_{11} - A_{12}^2}{A_{22}h} \qquad E_2 = \frac{A_{22}A_{11} - A_{12}^2}{A_{11}h} \qquad \nu_{12} = \frac{A_{12}}{A_{11}} \qquad \nu_{12} = \frac{A_{12}}{A_{22}} \qquad G_{12} = \frac{A_{66}}{h}$$

Single layer orthotropic laminate – Bending properties

Bending properties are related with flexural (bending) strains or curvature of laminates.

Using the same logic that was used for membrane properties but now using bending relative coefficients (D_{ij}):

$$\frac{Q_{12}\,(1 - v_{12}v_{21})}{v_{12}} = Q_{22}(1 - v_{12}v_{21}) \tag{159}$$

$$D_{12} = \frac{Q_{12}h^3}{12} (=)\ \ Q_{12} = 12\frac{D_{12}}{h^3} \qquad\qquad D_{22} = \frac{Q_{22}h^3}{12}\ (=)\ \ Q_{22} = 12\frac{D_{22}}{h^3}$$

Replacing Q_{12} and Q_{22} for the above two equations in equation 159, we obtain:

$$\frac{D_{12}}{v_{12}} = D_{22}$$

Inverting the equation:

$$\boldsymbol{v_{12} = \frac{D_{12}}{D_{22}}\ \ and\ \ v_{21} = \frac{D_{12}}{D_{11}}} \tag{160}$$

To calculate E_1 we recall that:

$$Q_{12} = \frac{v_{21}E_1}{1 - v_{12}v_{21}} \tag{161}$$

Inverting equation 161:

$$E_1 = \frac{Q_{12}(1 - v_{12}v_{21})}{v_{21}}$$

And replacing $Q_{12}\ v_{21}$ and v_{12}:

$$E_1 = \frac{12\frac{D_{12}}{h^3}\left(1 - \frac{D_{12}}{D_{22}}\frac{D_{12}}{D_{11}}\right)}{\frac{D_{12}}{D_{11}}}$$

We finally obtain:

$$E_1 = 12\frac{D_{11}\,D_{22} - D_{12}^2}{D_{22}h^3} \tag{162}$$

Following the same thought for E_2:

$$E_2 = 12\frac{D_{11}\,D_{22} - D_{12}^2}{D_{11}h^3} \tag{163}$$

At last, recalling that:

$$Q_{66} = 12\frac{D_{66}}{h^3}$$

$$G_{12} = Q_{66}$$

We obtain:

$$G_{12} = 12\frac{D_{66}}{h^3}$$

And summing up, the homogenised bending properties are:

$$E_1 = 12\frac{D_{11}\,D_{22} - D_{12}^2}{D_{22}h^3} \qquad E_2 = 12\frac{D_{11}\,D_{22} - D_{12}^2}{D_{11}h^3} \qquad \nu_{12} = \frac{D_{12}}{D_{22}}$$

$$\nu_{21} = \frac{D_{12}}{D_{11}} \qquad\qquad G_{12} = 12\frac{D_{66}}{h^3}$$

3.3.6.2 Failure criteria

Several failure criterions are available for composite materials (ex: Max Stress, max. Strain, Tsai-wu, Hoffman, Tsai-hill, etc). Max Stress criterion was not adequate because it assumes that there is no interaction between the modes of failure (Critical stress for one mode is unaffected by the stresses tending to cause the other modes). (Failure of laminates and the Tsai–Hill criterion s.d.).

Comparatively, Tsai-Hill criterion is slightly more conservative for compressive failure and Tsai-Wu criterion is slightly more conservative for tensile failure (Zafer Gürdal s.d.).

Both were then used for validating composite parts. It is important to note that both Tsai-hill and Tsai-Wu criterions allow quadratic stress interactions (see Figure 67).

If the stress state is contained within the area imposed by the ply failure envelope, no failure is predicted (HTT 2016).
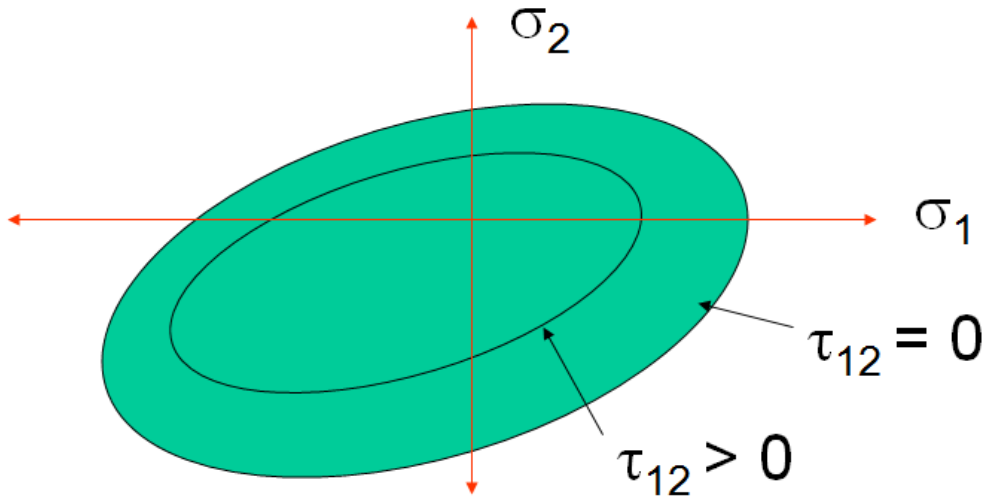
Figure 67 – Envelope for a quadratic ply failure theory - (Plymouth University s.d.)

Tsai-Hill Failure Criteria

Tsai-Hill criterion is an adaption of Von Mises criterion (a typical yield criteria for metals) as is referred by (University of Cambridge s.d.).

Von Mises Criterion for metals is given by:

$$(\sigma_1 - \sigma_2)^2 + (\sigma_2 - \sigma_3)^2 + (\sigma_3 - \sigma_1)^2 = 2\sigma_Y{}^2$$

(164)

Where σ_Y is the metal yield stress.

For in-plane Stress States ($\sigma_3 = 0$) the last equation can be reduced to

$$\left(\frac{\sigma_1}{\sigma_Y}\right)^2 + \left(\frac{\sigma_2}{\sigma_Y}\right)^2 + \frac{\sigma_1\sigma_2}{\sigma_Y{}^2} = 1$$

(165)

Modifying to take into account the anisotropy of composites and different failure mechanisms to give the following expression:

$$\left(\frac{\sigma_1}{\sigma_{1Y}}\right)^2 + \left(\frac{\sigma_2}{\sigma_{2Y}}\right)^2 - \frac{\sigma_1\sigma_2}{\sigma^2_{1Y}} - \frac{\sigma_1\sigma_2}{\sigma^2_{2Y}} + \frac{\sigma_1\sigma_2}{\sigma^2_{3Y}} + \left(\frac{\tau_{12}}{\tau_{12Y}}\right)^2 = 1 \qquad (166)$$

Metal yield stresses can be regarded as composite failure stresses and since composites are transversely isotropic ($\sigma_{2u} = \sigma_{3u}$), Tsai-Hill Criterion for composites is:

$$\left(\frac{\sigma_1}{\sigma_{1u}}\right)^2 + \left(\frac{\sigma_2}{\sigma_{2u}}\right)^2 - \frac{\sigma_1\sigma_2}{\sigma^2_{1u}} + \left(\frac{\tau_{12}}{\tau_{12u}}\right)^2 = 1 \qquad (167)$$

Note: This analysis is only applied for single isolated plies (lamina failure, not laminate failure).

Tsai-Wu Failure Criteria

Tsai-Wu criteria is a simplification of Gol'denblat and Kapnov's generalized theory for failure of anisotropic materials.

$$f_i\sigma_i + f_{ij}\sigma_i\sigma_j = 1 \qquad i,j = 1,2,3,4,5,6 \qquad (168)$$

For plane-stress condition:

$$f_1\sigma_1 + f_2\sigma_2 + f_6\tau_6 + f_{11}\sigma_1^2 + f_{22}\sigma_2^2 + f_{66}\tau_6^2 + 2f_{12}\sigma_1\sigma_2 + 2f_{16}\sigma_1\tau_6 + 2f_{26}\sigma_2\tau_6 = 1 \qquad (169)$$

Shear strength is independent of the sign of shear stress, so all linear shear stress terms might be removed. With this we obtain: (Dassault Systemes 2007)

$$f_1\sigma_1 + f_2\sigma_2 + 2f_{12}\sigma_1\sigma_2 + f_{11}\sigma_1^2 + f_{22}\sigma_2^2 + f_{66}\tau_6^2 = 1 \qquad (170)$$

Where:

$$f_1 = \frac{1}{X_T} - \frac{1}{X_C} \qquad\qquad f_2 = \frac{1}{Y} - \frac{1}{Y'} \qquad\qquad f_{11} = \frac{1}{X \times X'}$$

$$f_{22} = \frac{1}{Y \times Y'} \qquad\qquad f_{66} = \frac{1}{S \times S'} \qquad\qquad f_{12} = -0.5\sqrt{f11\,f22}$$

$$f_6 = \frac{1}{S} - \frac{1}{S'}$$

- X_T - Tensile Strength of the laminate in the direction of the fiber

- X_C - Compressive Strength of the laminate in the direction of the fiber

- Y - Tensile Strength of the laminate in the transverse direction of the fiber

- Y'- Compressive Strength of the laminate in the transverse direction of the fiber

- S - Positive shear strength

- S'- Negative shear strength (the solver considers it equal to the positive shear strength)

- σ_1 - Stress in the direction of the fiber

- σ_2 - Stress transversal to the direction of the fiber

- τ_{12} - Shear stress

4. Numerical methods: Finite Element Model

Finite Element Method (FEM) is a numerical method for field problems (used for structural, thermal, fluid and electrostatic problems). It has a great value in industry because it allows faster development of products since some physical/real simple tests don't need to be performed, saving time and money.

It has a finite number of degrees of freedom (DOFs) opposing to a continuous field which has infinite number of DOFs. The main idea is to divide a structure into several parcels (elements). The collection of elements is named finite element mesh. Each element has a certain number and location of nodes (depending on the type of the element used, the degree of the polynomial approximation and the weighted-integral form of the equations). It sets a number of simultaneous algebraic equations at those nodes that later permits finding the behavior of materials when subjected to certain actions (J.N.REDDY 2006).
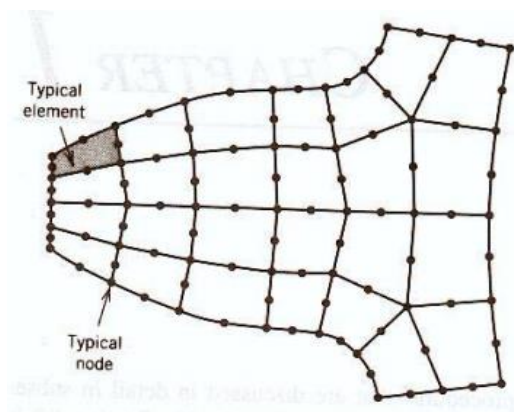
Figure 68 - Elements and nodes in a geometry - (J.N.Reddy 2006)

Finally is very important to mention that those solutions are approximated because FEM has inherent errors (for example: geometry simplification, field quantity is assumed as being polynomial, not using adequate elements) that sometimes can be fatal (KIM 2004).

For static analysis of structures, the matrix form of the equations of motion is:

$$[K]\{u\} = \{F\} \tag{171}$$

Where:

- [K] –Stiffness matrix (Property)

- {u} –Displacement vector (Behaviour)

- {F} –Force vector (Action)

Considering that the behaviour is the unknown field, the objective is to find it:

$$\{u\} = [K]^{-1}\{F\} \tag{172}$$

4.1. Basic features

This method has three distinct features that turns it out superior over other competing methods (for example Rayleigh-Ritz, Galerkin or Least Squares methods).

First, a geometrically complex domain of the problems is represented as collection of geometrically simple subdomains called finite elements. Each one is viewed as an independent domain by itself. (Domain – Geometric region over which the equations are solved).

Second, for each finite element, algebraic equations among the quantities of interest are developed using the governing equations of the problem.

Third, the relationships from all the elements are assembled using certain inter-element relationships. If elements are of the same length, the mesh is said to be uniform, otherwise it is called a non-uniform mesh.

The division of the whole domain into finite elements sometimes is not exact. This fact introduces error in the domain being modelled.

Generally, the dependent unknowns of the problem are approximated using the basic idea that any continuous function can be represented by a linear combination of known functions and undetermined coefficients.

Algebraic relations among the undetermined coefficients are obtained by satisfying the governing equations, in a weighted-integral sense, over each element. The approximation functions are often polynomial functions and they are derived using concepts of interpolation theory (that is why they are usually designated "Interpolation Functions")

Often, the error is not zero, which yields an approximated solution and not an exact solution.

Convergence and error estimate is a very important step of FEM studies. The main goal is that the approximated solution converges to an exact value when the number of elements approaches infinite. The error is the difference between real and approximated value.

4.2. Fundamental steps

According to (J.N.REDDY 2006), the fundamental steps of finite elements method are:

1. Discretize the geometry of the domain into a mesh. Depending on the shape of the geometry it might have more than one type of element (shape or order).

2. Seek an approximation to the solution as a linear combination of nodal values and approximation functions, and derive the algebraic relations among the nodal values of the solution over each part.

3. The number and location of the nodes in an element depend on:

       a) Geometry of the element

       b) Degree of the polynomial approximation

       c) Weighted-integral form of the equations

4. Assemble the parts and obtain the solution to the whole. The assembly of the elements is based on the idea that the solution is continuous at the inter-element boundaries.

5. The assemblage is subjected to boundary and/or initial conditions.

6. Estimation of error may not be simple sometimes, however under certain conditions it can be estimated for an element and problem.

7. The accuracy and convergence of the finite element solution depends on the differential equation, its integral form and element used. Accuracy stands for the difference between the exact solution and the finite element solution. Convergence refers to the accuracy as the number of elements in the mesh is increased.

In finite element method, an approximation of u_h of u (an analytical function) in the form (J. N. Reddy 1993)

$$u \approx u_h = \sum_{j=1}^{n} u_j \Psi_j + \sum_{j=1}^{m} c_j \phi_j \tag{173}$$

is sought.

Where:

- u_j are the values of u_h

- Ψ_j are the interpolation functions

- c_j are coefficients that are not associated with nodes

- Φ_j are the associated approximation functions

4.3. Software

The next three software were used for FEM simulations:

- *HyperMesh®*

This software is a pre-processor application. It allows to mesh, define constraints, properties, materials, and apply forces, moments, pressure and other type of solicitations.

- *MSC NASTRAN®*

MSC NASTRAN® is a solver to perform analysis such as static, dynamic and thermal with linear and non-linear domains. It is based on numerical methods such as Finite Element Method (FEM).

- *HyperView®*

This software is a post-processor application and helps visualizing the results obtained in a solver such as NASTRAN®.

MSC PATRAN

Pre and post processor

4.3.1. Elements

Connector elements

RBE2 and RBE3

In Figure 69 it's possible to compare differences between RBE2 and RBE3 elements that were used in this thesis. RBE stands for Rigid Body Elements. They are both multi point constraint elements (MPC) (SESTRUCUTRES 2016).

- RBE2 - "Define rigid connections between GRID points using different specifications of the dependent DOF." (UNIVERSAL ANALYTICS 1999)

- RBE3 are used to uniformly distribute a load from a reference point to other GRID points. (UNIVERSAL ANALYTICS 1999)
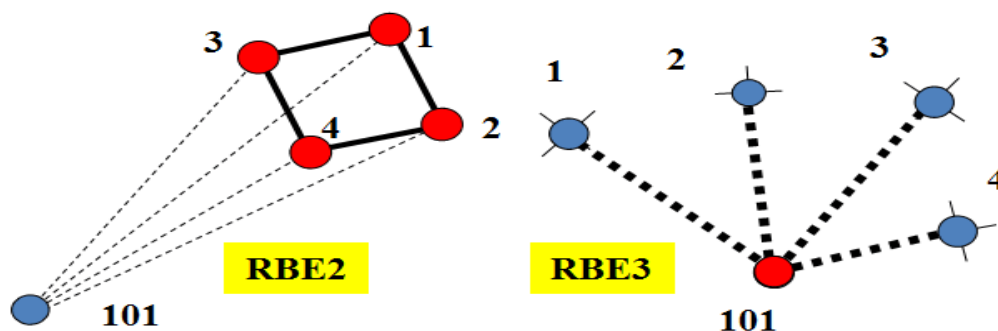
Figure 69 - RBE2 and RBE3 element differences - (Hart s.d.)

CBUSH

The Bush element is a combination of a scalar element (CELAS), that consists of six components (six independent springs and six independent dampers). These dampers and springs are located at the center, between the grids that are geometrically coincident – see Figure 70 (UNIVERSAL ANALYTICS 1999).
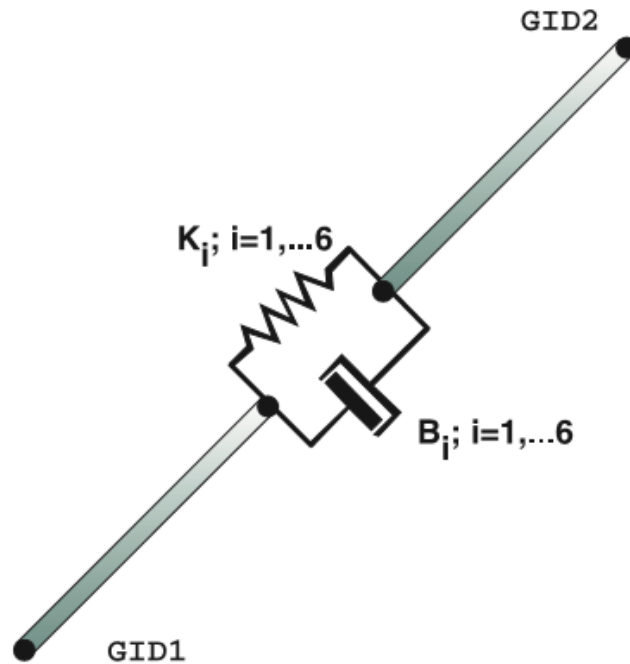
Figure 70 – Bush element geometry

Where:

- K_i – Stiffness coefficient for the *i* direction
- B_i – Damping coefficient for the *i* direction

1D Elements

They are used when one dimension is very large in comparison to the other two. Such as long-shafts, beams, pin joint and connection elements.

Usually they are elements of types: Rod, bar, pipe, axi-symmetric shell.

Bar Element – CBAR

It is an uni-axial element that supports traction, compression and torsion stress and even flexure moments. These elements are used for meshing beams. CBAR can provide stiffness to all six DOFs of each grid point. It has a constant cross sectional geometry along its length.

Solid models are complex and time-consuming and expensive and therefore shell models are preferred for interacting with fastener connections. These connections can be modelled by CBAR (node to node connection) (FE-MODELING OF BOLTED JOINTS IN STRUCTURES 2012).

The CBAR element can only be constituted of isotropic material. For each CBAR element, it is possible to obtain forces, stresses and strain energy. Tensile stresses are positive and compressive stresses are negative.

Shear center and neutral axis must coincide.

If shear deformations are involved in the element, reference axes (Planes 1 and 2) and the principal axes must coincide (UNIVERSAL ANALYTICS 1999).

Positive directions for element forces are shown in Figure 71 and Figure 72.
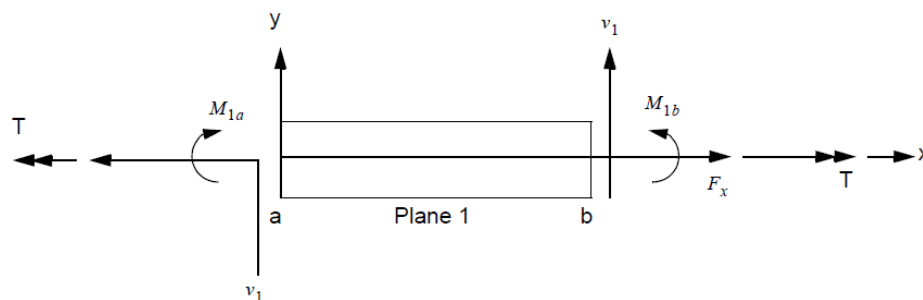
Figure 71 – CBAR element internal forces and moments (x-y Plane) - (UNIVERSAL ANALYTICS 1999)
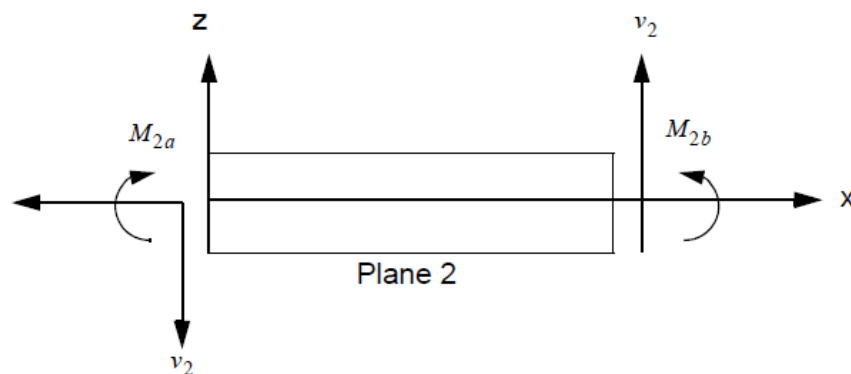
Figure 72 - CBAR element internal forces and moments (x-z Plane) - (UNIVERSAL ANALYTICS 1999)

A very important aspect related with CBARs is the definition of an orientation vector. This vector defines the orientation of an element in space. (Basically it specifies a local element coordinate system). Geometric properties of the element are entered in the element coordinate system. The orientation vector $\vec{v}$ defines plane 1 that contains the elemental **x** and **y** axes as can be observed in Figure 73 (UNIVERSAL ANALYTICS 1999).
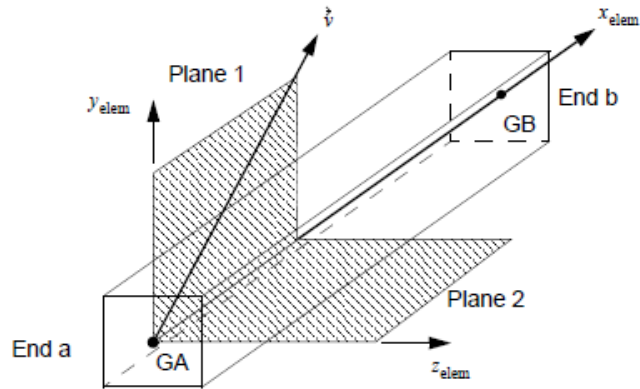
Figure 73- CBAR element coordinate system (UNIVERSAL ANALYTICS 1999).

Plane 1 must be defined by the user and contains the element x-axis and the orientation vector $\vec{v}$. Plane 2 contains element x and z axes. This vector can be defined by entering its components (X1, X2, X3).

Stresses can be obtained at four points on the cross section of the CBAR. The coordinates of these recovery points are defined on the PBAR Bulk Data entry. (UNIVERSAL ANALYTICS 1999)

As an example, Figure 74 presents the stress recovery point SA1, SA2, SA3 and SA4 for a beam with a circular cross section (ROD).
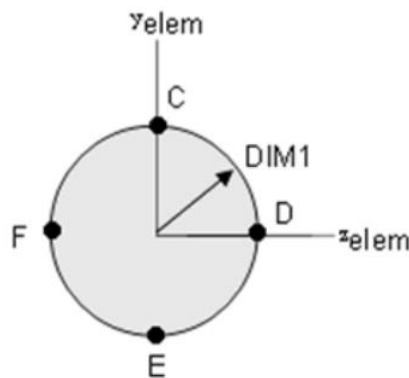
Figure 74 - Cross sectional of a ROD and its Stress recovery points (UNIVERSAL ANALYTICS 1999)

2D Elements

They are used when two of the dimensions are considerably large in comparison to the third dimension.

The element shape can be Quad or Tria.
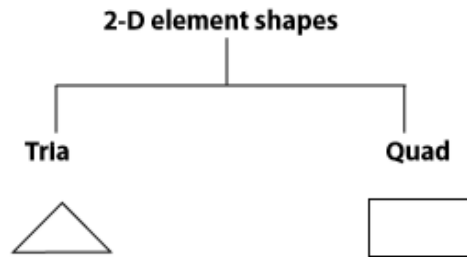
Figure 75 - 2-D Element shapes - © Altair Engineering, I. (2011)

As for the element type, it can be thin shell, membrane, plane stress, plane strain, axi-symmetric solid.

Shell Type Element

Shells are 2D elements that represent 3D space so they are categorized as 2.5D elements.

They are used for thin 3D structures (body panels, sheet metal and injection moulded plastic). Deflections are given at the nodes, but stresses can be found at the upper and lower surfaces as well as in the mid-plane - this deflections might be observed in Figure 76 (© ALTAIR ENGINEERING 2011).
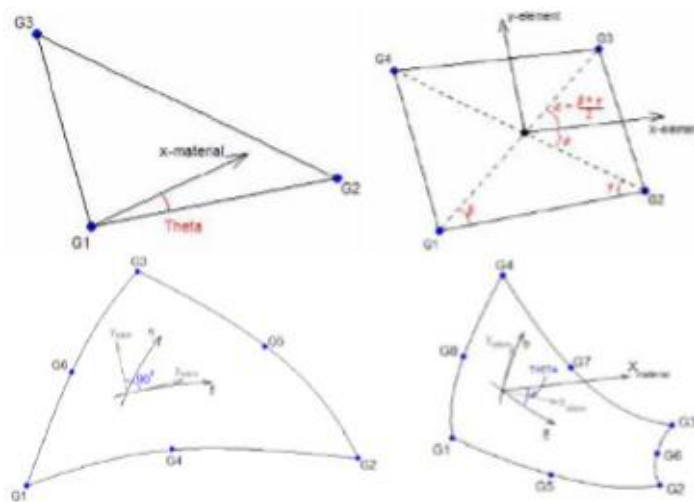
Figure 76 - Example of Shell elements (Ctria, CQuad, CTria6 and CQuad8) - (© Altair Engineering 2011)

QUAD4 and TRIA3 elements are constant strain iso-parametric elements and might be used to model bending and membrane behaviour. If the material and stress systems are not defined, the software assumes that they coincide with external element system. (UNIVERSAL ANALYTICS 1999)
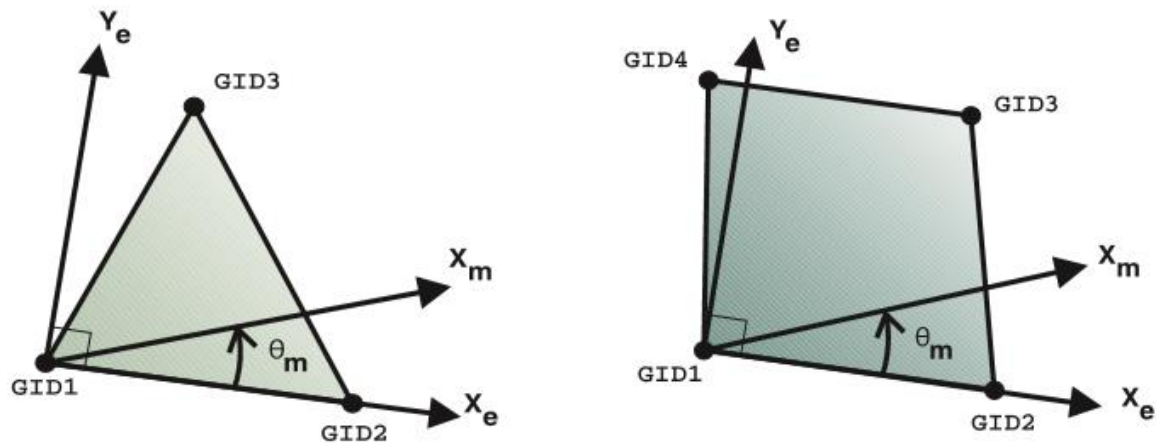
Figure 77 – TRIA3 and QUAD4 elements (UNIVERSAL ANALYTICS 1999)

Stress results include normal stresses, in-plane shear stresses, major and minor principal stresses, maximum shear stress (MAXSHEAR), Von Mises Stress (VONMISES).

Von Mises Stress is given by:

$$\sigma_{vm} = \sqrt{(\sigma_x^2 - \sigma_x \sigma_y + \sigma_y^2 + 3\tau_{xy}^2)}$$

Strain values also include: the normal strains in the x and y directions, in-plane shear strains, major and minor principal strains; and also the maximum shear strain or the von Mises equivalent strain (UNIVERSAL ANALYTICS 1999).

4.3.2. Properties

For 1D - property values can be assigned using HyperBeam (that is integrated in HyperMesh®) in certain type of elements or manually using Card Images.

For 2D and 3D elements the property collector will then be assigned to the element directly or to the elements component selector.

Property collectors

1D Elements

- PBARL

With PBARL there are some pre-defined cross-section shapes that can be used (ROD, TUBE, HEXA…) and that makes PBARL easy to use.

An important difference between PBARL and PBAR entries is that stress recovery points aren't defined by the user to obtain stress output for the PBARL entry. Stress Recovery points are automatically calculated at the locations shown in Figure 78 - Cross sectional of a ROD and its Stress recovery points (MSC Software 2013).

"Actually, the stress recovery points are automatically calculated at specific locations to give the maximum stress for the cross-section." (Altair s.d.).
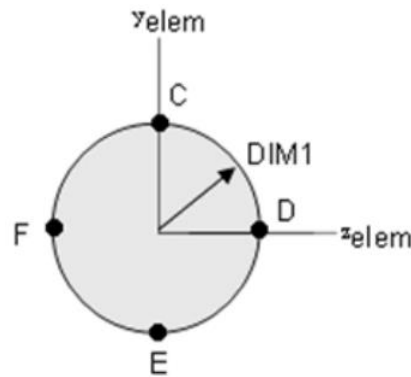
Figure 78 - Cross sectional of a ROD and its Stress recovery points (MSC Software 2013).

2D Elements

- PSHELL

Defines the properties of a shell elements; It is best used for isotropic materials, but can also be assumed for orthotropic materials

- PCOMP

Defines the structure and properties of a composite lay-up which is then assigned to an element. Plies are only defined for that particular property and there is no relationship of plies that reach across several properties.

Connector Elements

Pbush – Defines the nominal property values for generalized spring-and-damper structural element.

4.3.3. Materials

Defining a material is a very important step during FEM procedures. A reliable source of data must be used and attention is needed when different unit systems are being used.

Materials are stored in material collectors. Initially, it's crucial to define if the material is isotropic or orthotropic. Then, it's necessary to select a card image to represent that material. At last, it's necessary to introduce material properties on the card image.

MAT 1 - Linear, elastic, homogeneous, isotropic materials are modelled in MSC.Nastran with the MAT1 Bulk Data entry (UNIVERSAL ANALYTICS 1999).

MAT 8 - Orthotropic material for two-dimensional elements. This entry is used to define a two dimensional orthotropic stress relationship. It can only be used with plate and shell elements.

5. Analysis

5.1. Functional requirements

A Composite Leaf Spring was chosen for this prototype of landing gear. The main reasons were the lower weight, the reduced number of pieces, being easy to inspect visually and easy to replace in case of damage

All the requisites imposed by actual legislation and described in chapter 3 were respected.

The requirements imposed by CEiiA were:

- Maximum weight of the leaf spring: 180g

- Maximum width of the leaf spring: 45mm

- Height: 190 mm (approximately)

- Maximum vertical displacement: 95mm

It is crucial to respect designing requirements beyond those established by CEiiA:

Table 7 - Functional requirements (Sadraey, 2012)

1	Ground distance	Wing, engine, fuselage, propeller
2	Controlability during taxi	Max load on nose-wheel must be imposed
3	Taxi ground rotation	Must be possible to taxi the aircraft on the ground in a minimum space
4	Distance between the aircraft and ground during rotation	Tail and back zone of fuselage must not touch the ground during take-off
5	Permanent down tail situation	Preventing the down tail situation during taxi and take off
6	Roll-Over	Side angle must prevent the roll over situation while taxing in a tight space
7	Landing	Strut and wheel must stand and dissipate imposed loads
8	Static and dynamic loads	Landing gear must resist while static or dynamic load cases
9	Lateral Stability	Aircraft must not roll over during crosswind manoeuvres

5.2. Conceptual Design

5.2.1. MATLAB software function

A MATLAB function was computed in order to reduce the studying time for each stacking sequence and geometry.

This function can be divided in two parts:

1. Membrane and bending properties
2. Displacement and Stress values

The first part is related with the theoretical principles of composites explained in chapter 3.3 while the second part is related with the theoretical model of a curved beam explained in chapter 3.2.

Part 1 – Membrane and bending properties

Inputs

The inputs for the first part of the function are:

- **E1** – Young Modulus in direction 1
- **E2** – Young Modulus in direction 2
- **G12** – In-plane Shear modulus
- **N12** – Poison coefficient in direction 1
- **N21** – Poison coefficient in direction 2
- **Esp** – thickness of each layer
- **Matrix of stackings[2]** – each line is one stacking
- **numeroplies** – is a vector where each row is the number of plies of each laminate

The software code can be found in the attachments of this study.

Note: This software is restricted to use layers of the same material – only tolerates changes of direction between layers.

---

[2] Each line of the matrix must have 40 elements, independently if each laminate has 40 or less layers. If a laminate has less than 40 layers, the line of that laminate in the matrix must be filled firstly from the left and then after the last layer, the line must be filled with number 1 for each row as can be seen in the next example:

[45 -45 0 0 45 -45 0 0 0 -45 45 90 -45 45 0 0 45 -45 90 45 -45 0 0 0 -45 45 0 0 -45 45 1 1 1 1 1 1 1 1 1 1;]

Methodology

Firstly the software reads the matrix of stackings and then applies a transformation for radians angle. After that, it computes Q11, Q12, Q22 and Q66 with data from the inputs.

Then it computes $\overline{Q_{ij}}$ for each plie of each laminate. With this it can finally compute A_{ij}, B_{ij}, D_{ij} coefficients and also matrix: [A], [B] and [D]. With these coefficients it is finally possible to obtain the equivalent properties for each laminate.

Outputs

For **membrane** properties:

Exx, Eyy, Gxy, NuXY, NuYX.

For **bending** properties:

Exx_B, Eyy_B, Gxy_B, NuXY_B, NuYX_B.

Part 2 – Displacement and stress values

Inputs

The inputs for the second part of the function are:

- **p** – vertical force applied [N]
- **larg** - width of the beam [mm]
- Geometry parameters (typically an ellipse beam is defined by two coefficients: a and b; if it's a circle beam: a=b)
  - ➤ **a** is a single value for this case of study corresponding to half the height of the landing gear, 95mm (imposed by CEiiA requirements, 190mm – see chapter 5.1)
  - ➤ **b** is varied with the purpose of finding a good relation between geometry and stress/displacement results [mm]

The software calculates for each laminate its respective thickness. Using theoretical models for curved beams it can calculate the horizontal and vertical displacement and stresses.

The output of this software is then exported automatically for an Microsoft Excel file and it's composed by a table as can be observed in Figure 79:

4	4	4	4
b	v	h	s
50	1	3	59.13
52	2	3	61.50
54	2	4	63.87
56	2	4	66.23
58	2	4	68.60
60	2	4	70.96
62	2	4	73.33
64	2	4	75.69
66	3	5	78.06
68	3	5	80.42
70	3	5	82.79
72	3	5	85.15

Figure 79 – Example of the output file obtained in Excel

Where:

- The numbers in the first line are the identification of the stack (for this exemple, we are observing the results for the 4th stacking sequence introduced as an input)

- The first column presents the variable **b** (the input as explained in the previous paragraphs) [mm]

- The second column presents the variable **v** that contains each value of vertical displacement for each value of variable **b** (one of the outputs) [mm]

- The third column presents the variable **h** that contains each value of horizontal displacement for each value of variable **b** (one of the outputs) [mm]

- The fourth column presents the variable **s** that contains each value of stress for each value of variable **b** (one of the outputs) [MPa]

5.2.2. FEM validation of MATLAB function

Modeling approach (inputs to the FEM models)

Initially for FEM validation, an isotropic material (aeronautical aluminium) was considered for simplicity reasons. Afterwards, an orthotropic material (aeronautical CFRP – *Carbon Fiber Reinforced Polymer*) was considered.

For the **isotropic material,** three values for the input variable **b** were considered (since this was only a software test, the requirements were taken into account, thus the variable a presents a higher value than the requirement explain in chapter 5.2.1). Two modelling approaches were considered:

1) 1D finite elements_*CBAR* with the property _*PBAR*_ and the material _*MAT1*_. For each approach, the following geometries were considered:

    1. b = 94 mm

    2. b = a = 127.5 mm

    3. b = 140 mm

2) 2D finite elements_*CQUAD4/CTRIA3* with the property _*PSHELL*_ and the material _*MAT1*_. For each approach, the following geometries were considered:

    1. b = 94 mm

    2. b = a = 127.5 mm

    3. b = 140 mm

Table 8 presents the material properties considered. It was considered a thickness of 4mm.

Table 8 – Properties of the used isotropic material for MATLAB function validation

Material	E (GPa)	ν
Aluminium	70	0.33

For the **orthotropic material**, two modelling approaches were considered[3]:

1) 2D finite elements *CQUAD4/CTRIA3* with the property _*PCOMP*_ and the material _*MAT8*_, where all plies are modelled using the FEM software:

    1.   b = 94 mm

    2.   b = a = 127.5 mm

    3.   b = 140 mm

2) 2D finite elements *CQUAD4/CTRIA3* with thewith property _*PSHELL*_ and the material _*MAT8*_ (a=b=127.5mm), where equivalent properties are modelled as a single orthotropic layer using the FEM software (Hypermesh).

    1.   b = 94 mm

    2.   b = a = 127.5 mm

    3.   b = 140 mm

---

[3] It is not possible to represent a composite structure with 1D FEM.

For both isotropic and orthotropic cases was considered:

- Width: 45mm
- Thickness: 4mm
- Vertical force: 548 N

The properties of the test composite material can be checked in Table 9.

Table 9 – Properties of the used orthotropic material for MATLAB function validation

Material	Thickness [mm]	Elastic Properties				Allowables [MPa]				
		Exx [MPa]	Eyy [MPa]	Gxy [MPa]	ν_{xy}	Xt	Yt	Xc	Yc	S
Carbon Fiber	0.66	248312.4	47934.6	6048.64	0.196	389	280	389	271	50

For each situation the following outputs were considered in order to compare them to the outputs of the MATLAB software:

- Vertical displacement
- Horizontal displacement
- Stresses

It was introduced a fixed constraint at the top of the circular beam and a vertical force applied at the extreme of the down part of the beam as can be checked in Figure 80.

Figure 80 – Scheme of the MATLAB test load case

The element size considered was 10mm for all the cases.

Figure 81 demonstrates and example of how displacement data is analysed on HyperView Software.

Magnitude displacement:
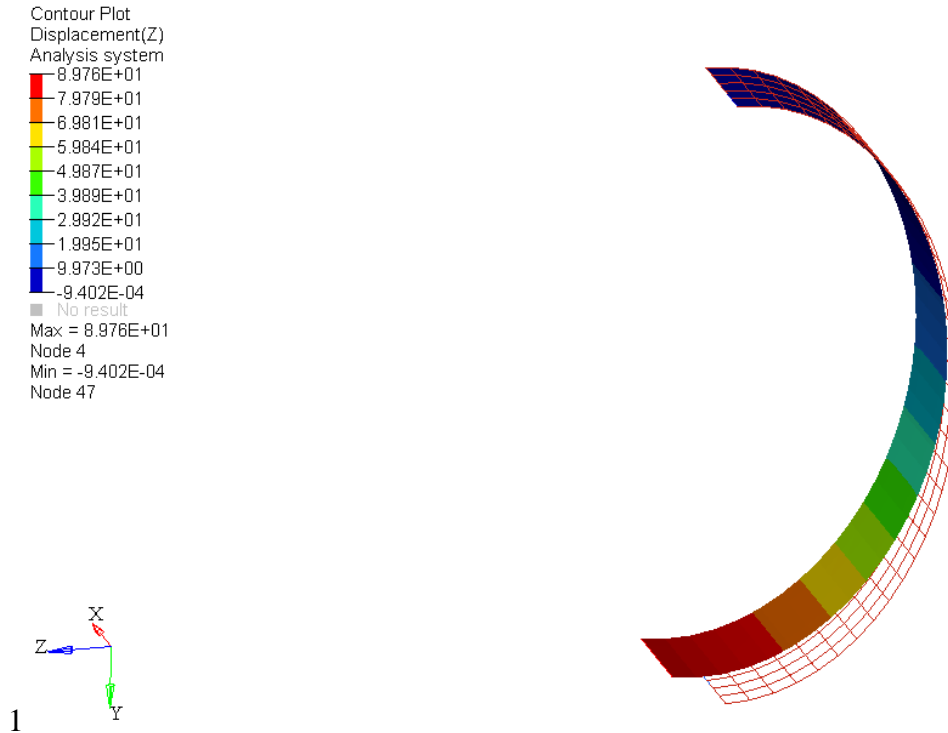
Figure 81 – Example of displacement data shown on HyperView software using 2D finite elements

Figure 82 demonstrates how stress data is analysed on HyperView Software.
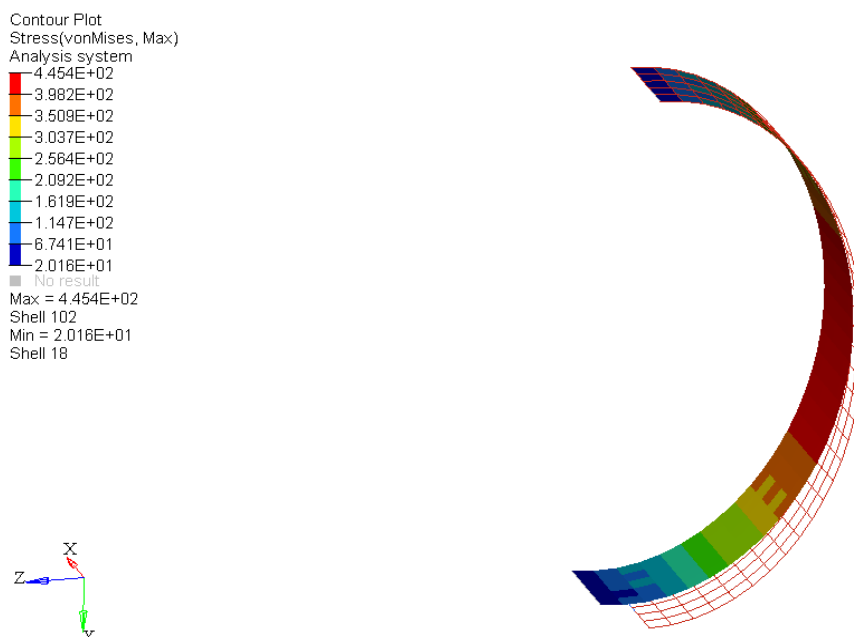
Figure 82 –Example of stress data shown on HyperView software using 2D finite elements

Data analysis (outputs of the FEM models)

The results can be checked in the following figures.

Graphical results of isotropic curved beam for displacements (1D and 2D) can be checked in Figure 83.
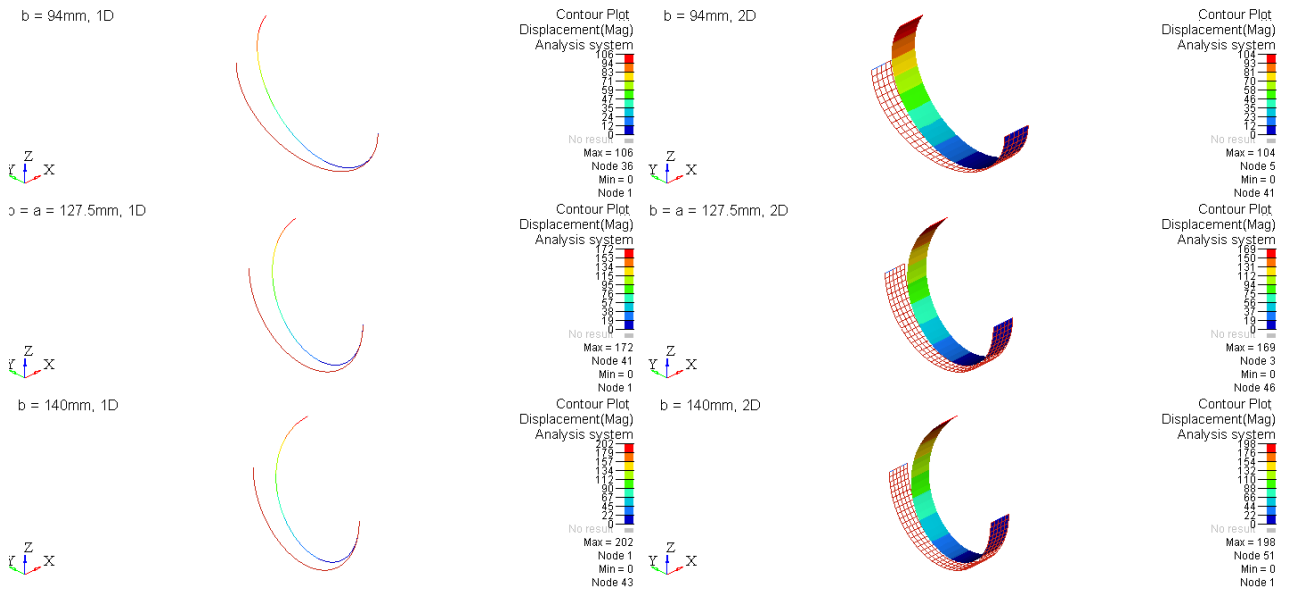
Figure 83 – Graphical Displacement results for an isotropic curved beam (1D and 2D) - Hyperview®

Graphical results of orthotropic curved beam for displacements (PCOMP and PSHELL) can be checked in Figure 84.
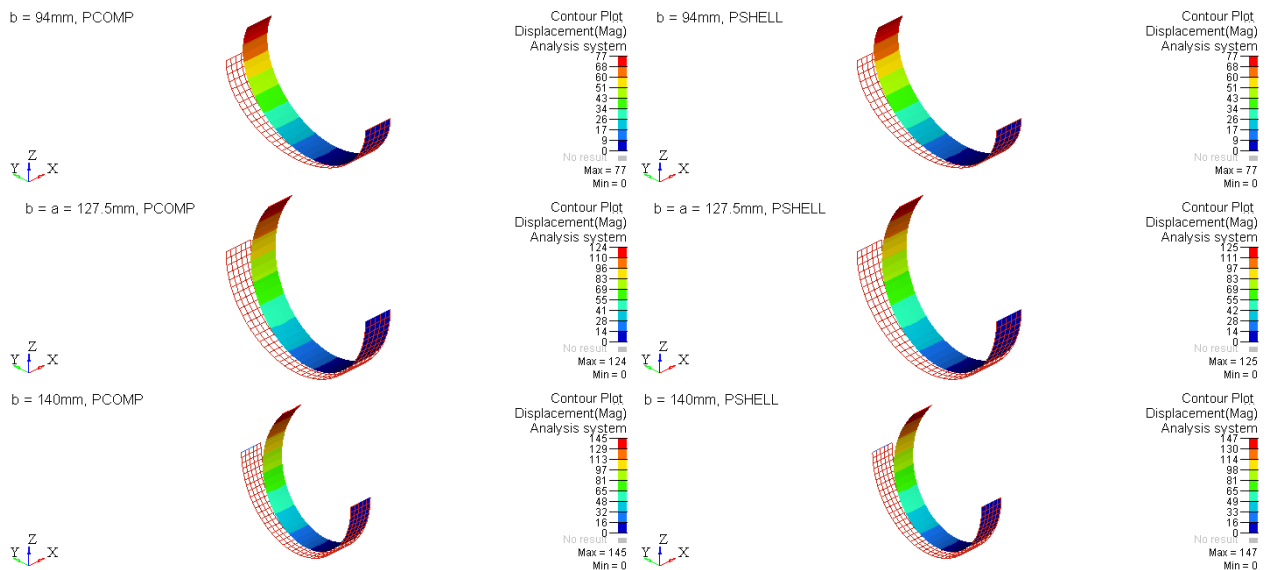
Figure 84 – Graphical Displacement results for an orthotropic curved beam (PCOMP and PSHELL properties) - Hyperview®

Graphical results of isotropic curved beam for stresses (1D and 2D) can be checked in Figure 85.
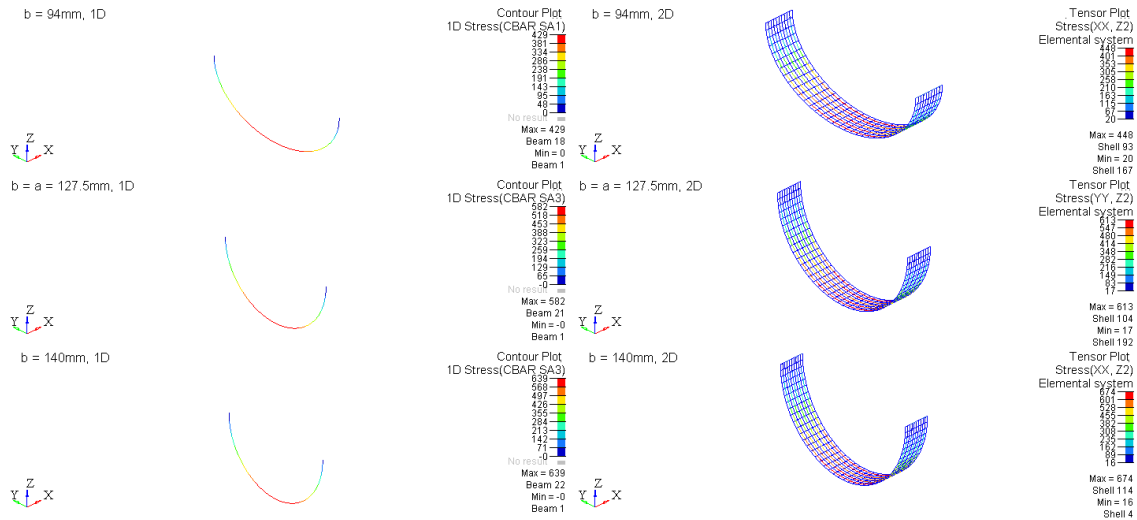
Figure 85 - Graphical stresses results for an Isotropic curved beam (1D and 2D) - Hyperview®

To obtain stress results of composite parts with PCOMP property it was necessary to use another software: MSC PATRAN®.

Stress result for a composite curved beam with b = 94mm, analysed with property PCOMP can be found in Figure 86.
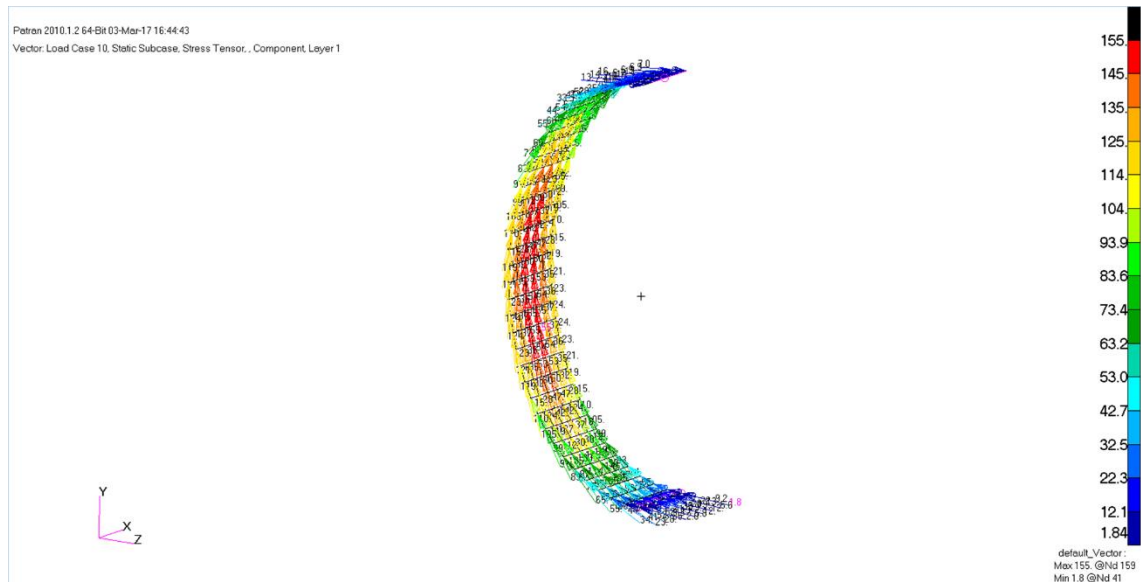
Figure 86 - Stress results for a composite curved beam (b = 94mm) , analysed with property PCOMP - obtained with MSC PATRAN®

Stress result for a composite curved beam with b = 127.5 mm, analysed with property PCOMP, can be found in Figure 87.
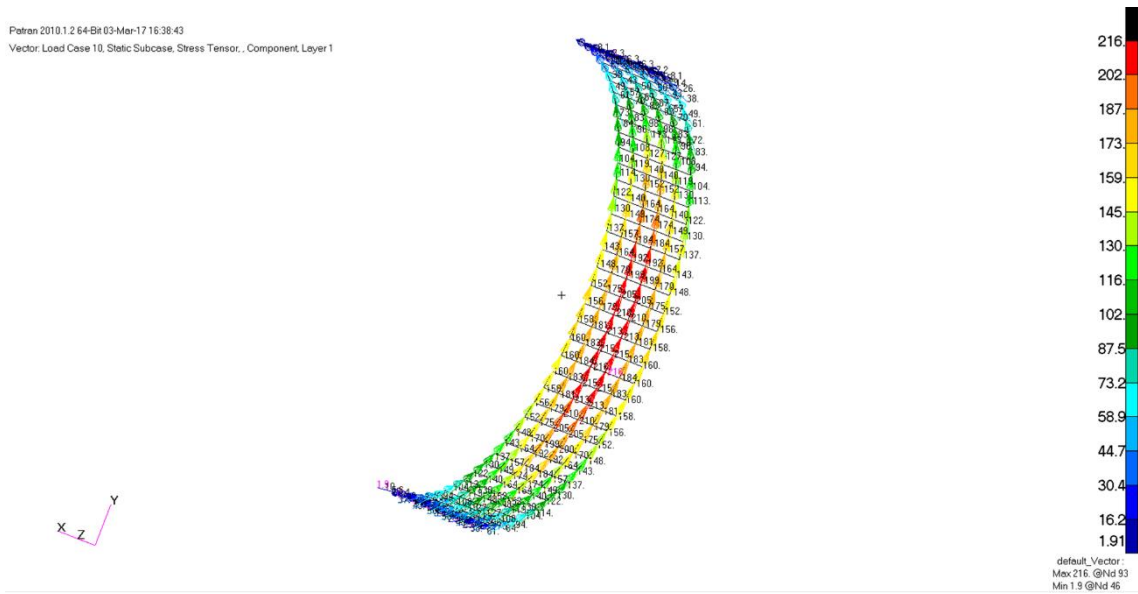
Figure 87 - Stress results for a composite curved beam (b = 127.5mm) , analysed with property PCOMP - obtained with MSC PATRAN®

Stress result for a composite curved beam with b = 140mm, analysed with property PCOMP , can be found in Figure 88.
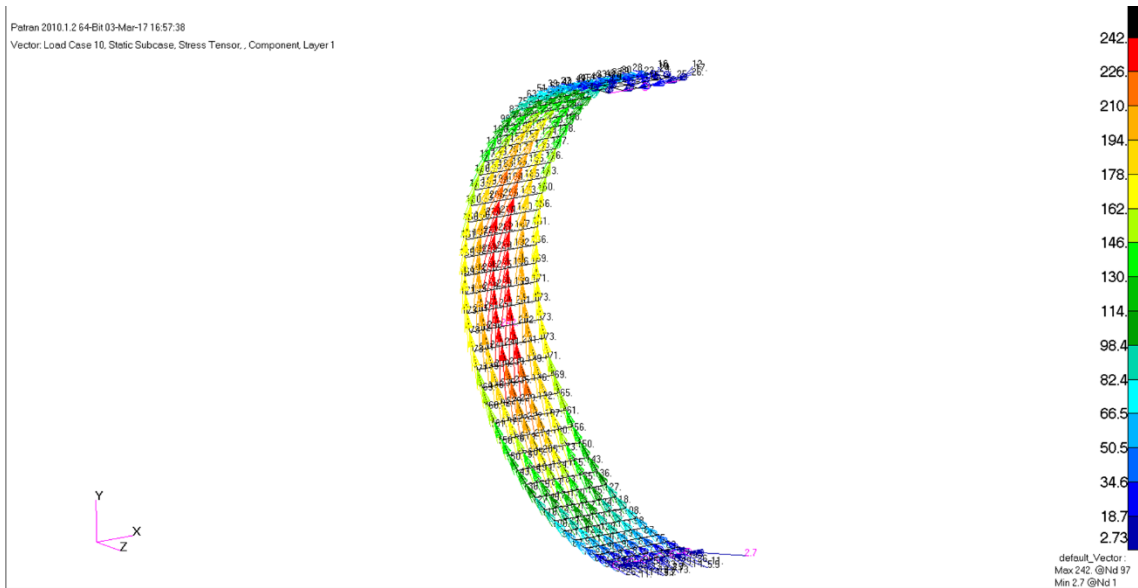
Figure 88 - Stress results for a composite curved beam (b = 140mm) , analysed with property PCOMP - obtained with MSC PATRAN®

Stress result for a composite curved beam with b = 94mm, analysed with property PSHELL can be found in Figure 89.
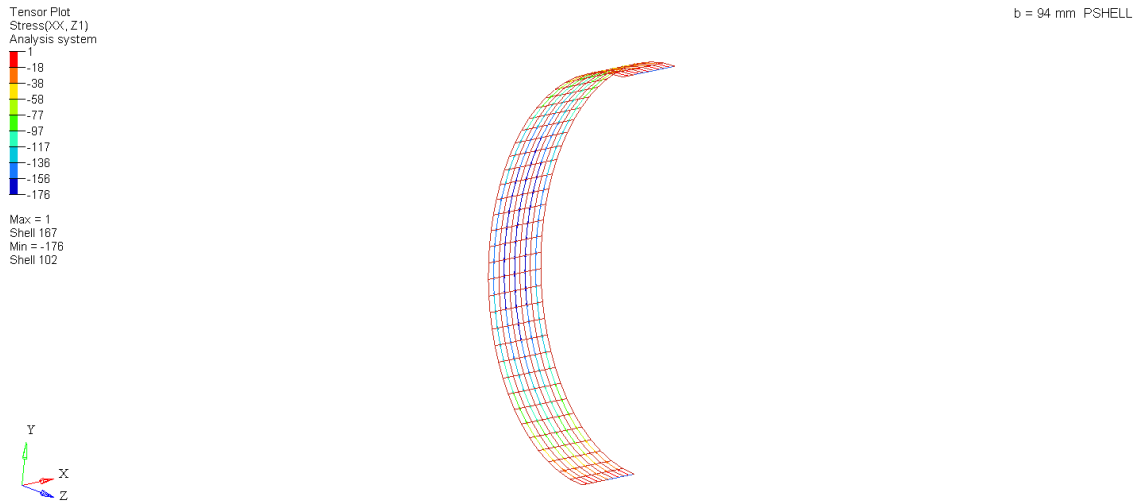
Figure 89- Stress results for a composite curved beam (b = 94mm) , analysed with property PSHELL - obtained with Hyperview®

Stress result for a composite curved beam with b = 127.5 mm, analysed with property PSHELL, can be found in Figure 90.
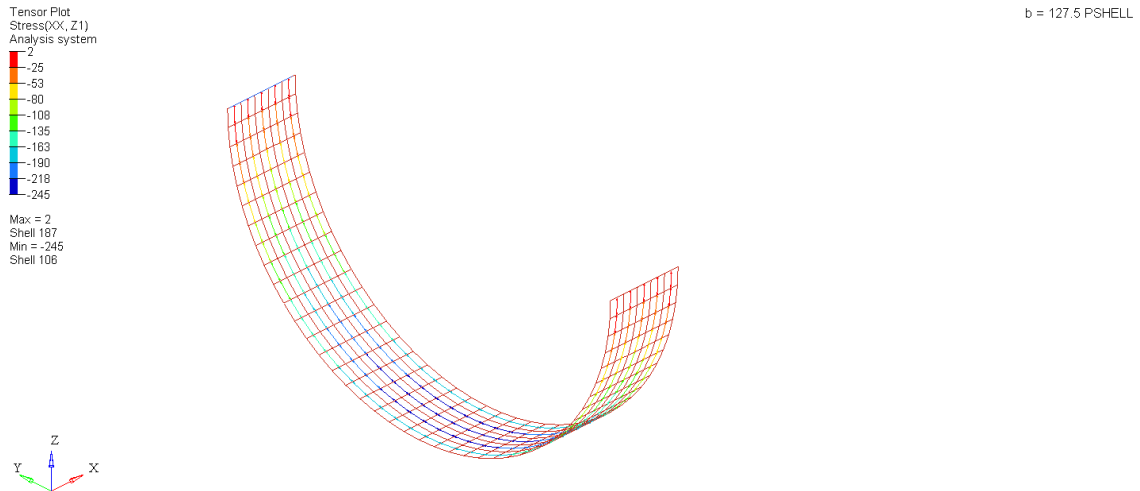
Figure 90 - Stress results for a composite curved beam (b = 127.5mm) , analysed with property PSHELL - obtained with Hyperview®

Stress result for a composite curved beam with b = 140 mm, analysed with property PSHELL can be found in Figure 91.
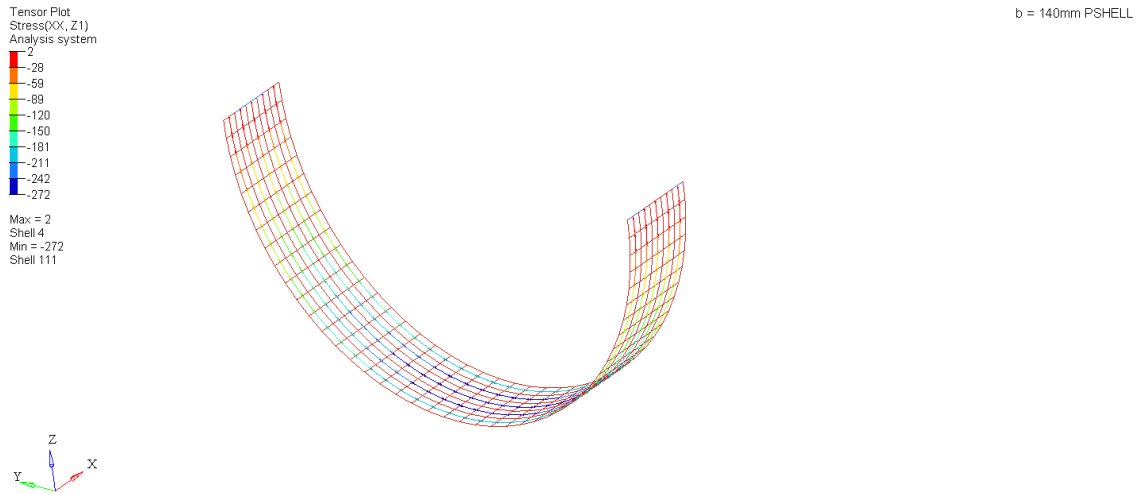
Figure 91- Stress results for a composite curved beam (b = 140mm) , analysed with property PSHELL - obtained with Hyperview®

Table 10 presents a resume-table which displays the results for the **isotropic material**:

Table 10 - Resume table for isotropic material

		Isotropic - Aluminium		
		(b=94mm)	**(b=127,5mm=a)**	**(b=140mm)**
Analytic	**horizontal (mm)**	91	135	153
	vertical (mm)	54	106	131
	Stress (without Corr.F.) (MPa)	429.27	580	639.33
FEM 1D	**horizontal (mm)**	91	135	153
	vertical (mm)	54	106	131
	Stress (MPa)	429.00	582	639.00
FEM 2D	**horizontal (mm)**	90	133	151
	vertical (mm)	53	104	129
	Stress (MPa)	448.00	613.00	674.00

Table 11 presents a resume-table which displays the results for the **orthotropic material**:

Table 11 - Results for Orthotropic material

		Ref. Composite		
		PCOMP		
		(b=94mm)	**(b=127,5mm=a)**	**(b=140mm)**
Analytic	**horizontal (mm)**	70	102	117
	vertical (mm)	41	79	100
	Stress (without Corr.F.) (MPa)	157.67	214.70	234.83
FEM 2D	**horizontal (mm)**	66	97	110
	vertical (mm)	39	77	95
	Stress (MPa)	155.00	216.00	242.00
		PSHELL		
Analytic	**horizontal (mm)**	70	102	117
	vertical (mm)	41	79	100
	Stress (without Corr.F.) (MPa)	157.67	214.70	234.83
FEM 2D	**horizontal (mm)**	66	98	111
	vertical (mm)	39	77	95
	Stress (MPa)	176.00	245.00	272.00

On Table 12 and

Table 13 it's possible to note the relative error between analytic and FEM solutions:

Table 12 - Relative error for isotropic material

		Isotropic - Aluminium		
		(b=94mm)	**(b=127,5mm=a)**	**(b=140mm)**
FEM 1D	**horizontal (%)**	0.11	0.08	0.07
	vertical (%)	0.12	0.10	0.09
	Stress (%)	0.06	0.35	0.05
FEM 2D	**horizontal (%)**	0.11	1.91	1.89
	vertical (%)	0.12	1.92	1.92
	stress Von Mises (%)	4.36	5.70	5.42

Table 13 - Relative error for orthotropic material

		Ref. Composite		
		PCOMP		
		(b=94mm)	**(b=127,5mm=a)**	**(b=140mm)**
FEM 2D	**horizontal (%)**	5.78	4.15	5.58
	vertical (%)	5.05	2.95	5.58
	stress (%)	1.70	0.60	3.05
		PSHELL		
FEM 2D	**horizontal (%)**	5.23	3.43	4.83
	vertical (%)	4.54	2.20	4.78
	stress (%)	11.62	14.11	15.83

The error related to stress results, associated with PSHELL property is justified by the assumed linear distribution of the software. Basically, it analyses the laminate as an equivalent single layer, while PCOMP property analyses the composite laminate, lamina by lamina, wich is more correct than the first type of analysis.

5.2.2.1 Convergence Analysis

Analysing and validating results is a very important step in FEM. The more elements used, the better the results. The main problem is that in complex setups, using too many elements result in long, expensive and unnecessary analysis.
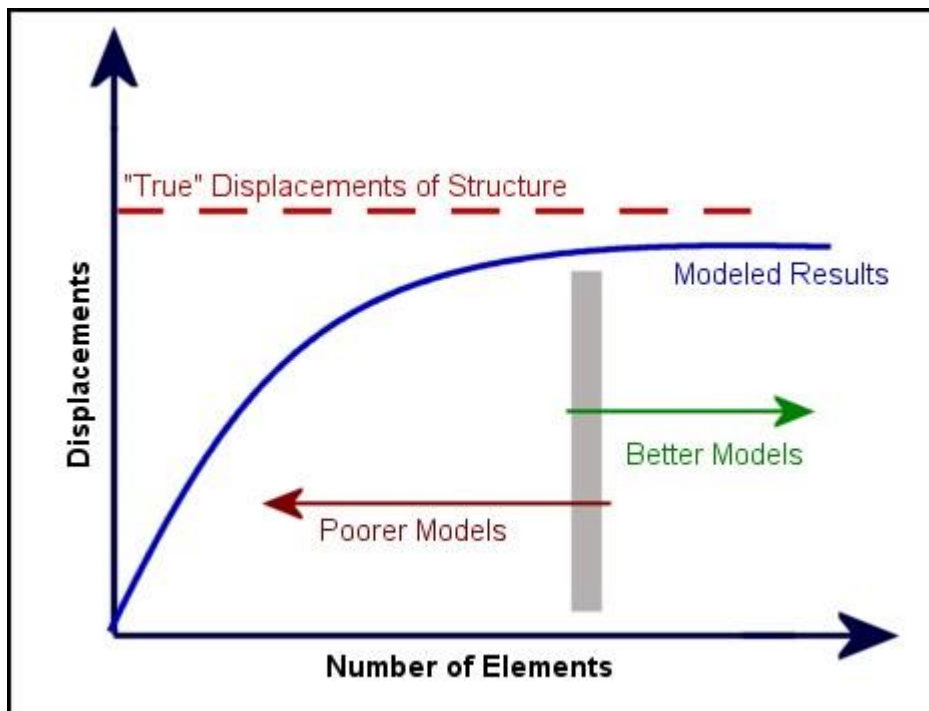
Figure 92 - Comparing results of different number of elements studies - (*Visual Analysis 12.0 Help* (2016))

The number of elements in a mesh is inversely proportional with the size of each element.

 To ensure a plane stress condition,the size of the elements should be at least 2.5 times the depth of the shell. As the depth of the studied shell is 4mm, the study of convergence started with an element size of 10.

There are 2 types of convergence:
1.   h- type - Changing the size of elements
2.   p- type -Changing the type of the elements (higher order)

The convergence study was performed with the model of a 2D curved isotropic beam (using properties from Table 8) with a=b=127.5mm, for different element size with the following geometric characteristics[4]:

Table 14 - Study of convergence - Geometry properties used

Radius	127.5mm
Width	45mm
Thickness	4mm
Force	548N

The results for the theoretical model were:

Vertical [mm]	106
Horizontal [mm]	135
Stress [Mpa]	576.2

The results for the FEM model and the comparison with the theoretical model can be checked in Table 15 for CQUAD elements.

Table 15 – Convergence Analysis for 2D Circle – CQuad Elements

	Horizontal	Vertical	Stress
El.Size	Relative error [%]	Relative error [%]	Relative error [%]
15	3	3	6
17	3	3	6
21	3	2	0
23	3	2	0
28	2	2	0
32	4	3	2
36	4	3	2
40	3	2	0
50	3	1	1
65	2	2	4
75	3	2	4
90	4	9	12

As it is possible to check, the relative error for small element sizes is small for displacement results as the element size is smaller (more elements in the mesh), while for stress it is a bit

---

[4] The study of the second type (p-type) was not considered since CQUAD8 elements and other higher order elements are not usually used in the aeronautical static strength assessments.

more considerable and it doesn't decrease significantly as the element size decreases (even though the relative error is smaller than 10% in most of the cases).

5.2.3. Geometry properties

After validating the built function on MATLAB® using FEM simulations, the first step was to choose a shape for the composite leaf spring.

To help choosing the geometry properties of the leaf spring and also the stacking, a MATLAB® program was developed to obtain primary results in a faster way.

Analysing graphic results obtained by MATLAB® function in terms of stress and deflection (both horizontal and vertical) the final shape of curvature was an ellipse with the following characteristics:

- a = 95.15 mm
- b = 106 mm
- Width = 45mm

Considering 3 different comparisons:

- Stress
- Horizontal deflection
- Vertical deflection

The main objective is to have an equilibrium between stress, horizontal and vertical displacement. It's clear that if parameter b increases, stress will increase, since for the same force, the arm that causes the bending moment also increases.

Deflection in both directions is also needed to dissipate the energy of the touch-down impact during the landing moment.
Taking into account the requirement in chapter 5.1"Maximum vertical deflection: 95mm" , the highest value of acceptable vertical displacement is 95mm, which is higher than any value considered for b in the 6 different studied stacking (see Figure 95).

As this requirement seemed a bit out of the typical values of deflection for landing gears of this scale, after a brief search it was found out that a value of 1/5 of the total height of the landing gear was acceptable, so 40 mm was the maximum value considered for vertical and horizontal displacement. Obviously a low value of b would create a more rigid structure but that is not desirable because it would not absorb the landing impact.

The considered stacking sequences were:

Stack 1: [45/ -45/ 0 / 0 / 45/ -45/ 90/ -45/ 45/ 0/ 0/ 45/ -45/ 90/ -45/ 45/ 0/ 0/ -45/ 45]

Stack 2: [45/ -45/ 0/ 0/ 45/ 0/ -45/ 90/ 45/ -45/ 0/ 45/ 0/ 0/ 45/ 0/ 45/ -45/ 90/ -45/ 0/ 45/ 0/ 0/ -45/ 45]

Stack 3: [45/ -45/ 0/ 0/ 0/ 45/ -45/ 90/ 90/ -45/ 45/ 0/ 45/ -45/ 0/ 0/ -45/ 45/ 0/ 45/ -45/ 90/ 90/ -45/ 45/ 0/ 0/ 0/ -45/ 45]

Stack 4: [45/ -45/ 0/ 0/ 45/ -45/ 0/ 0/ 0/ -45/ 45/ 90/ -45/ 45/ 0/ 0/ 45/ -45/ 90/ 45/ -45/ 0/ 0/ 0/ -45/ 45/ 0/ 0/ -45/ 45]

Stack 5: [45/ -45/ 0/ 0/ 90/ 45/ -45/ 45/ -45/ 0/ 0/ 0/ 45/ -45/ 90/ -45/ 45/ -45/ 45/ 0/ 0/ 45/ -45/ 45/ -45/ 90/ -45/ 45/ 0/ 0/ 0/ -45/ 45/ -45/ 45/ 90 / 0 / 0 / -45/ 45]

Stack 6: [45/ -45/ 0/ -45/ 45/ 90/ -45/ 45/ 0/ -45/ 45/ 0/ 0/ 45/ -45/ 90/ 90/ -45/ 45/ 0/ 0/ 45/ -45/ 90/ 90/ -45/ 45/ 0/ 0/ 45/ -45/ 0/ 45/ -45/ 90/ 45/ -45/ 0/ -45/ 45]

In Figure 93, Figure 94, Figure 95 it is possible to observe the obtained results for: stress, horizontal and vertical displacement (respectively).
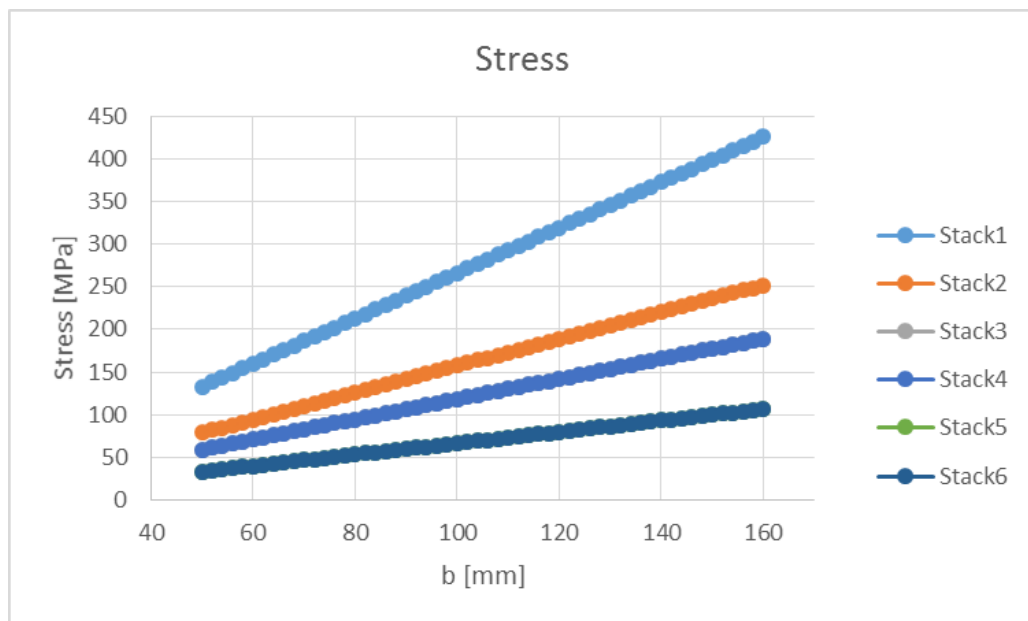
Figure 93 - Stress variation with parameter of geometry b.
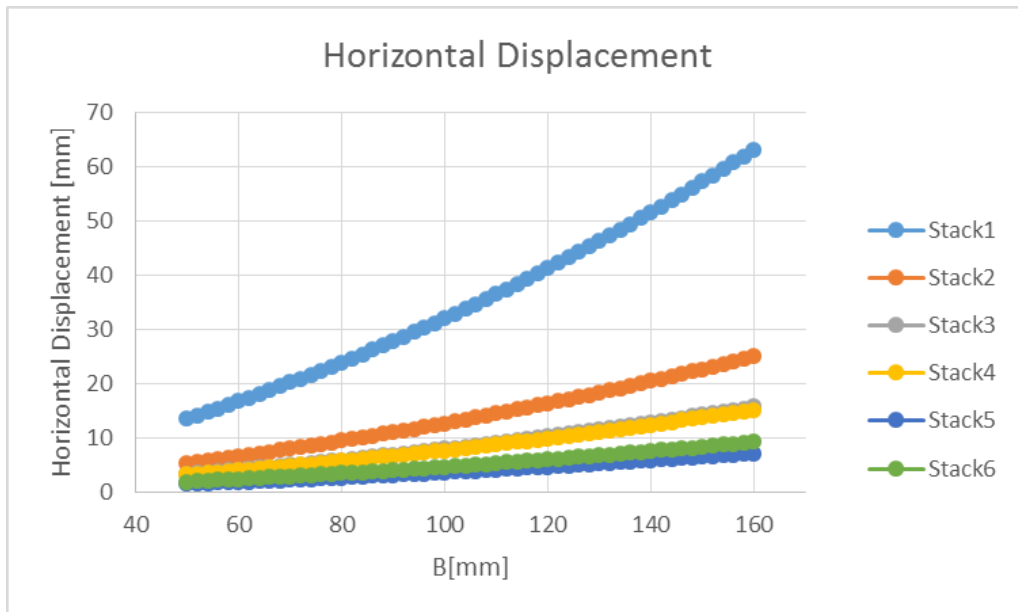
Figure 94 - Horizontal displacement variation with parameter of geometry b.
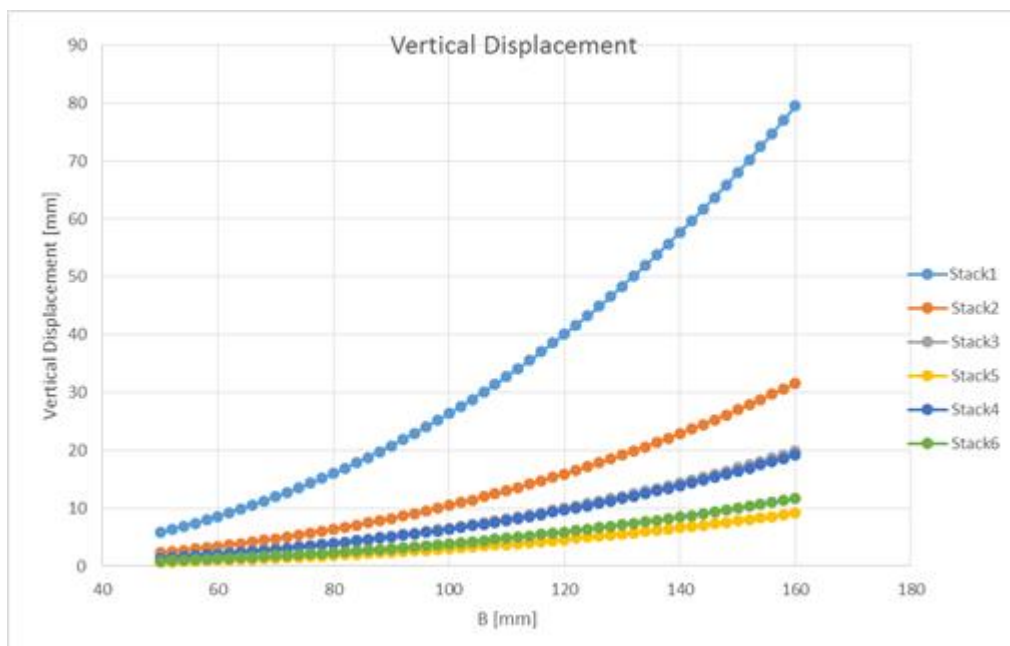
Figure 95 - Vertical displacement variation with parameter of geometry b.

5.2.4. Selection of stacking sequence

With a defined shape, a weight restriction of 180g and with the available material it is easy to find the maximum number of layers that can be applied.

The material that was provided by CEiiA was a PrePreg Carbon Fiber – Unidirectional and had the following mechanical properties (see Table 16).

Table 16 – PrePreg properties

Designation	Nominal Laminate Density	ILSS	Compression Strength	Compression Modulus	Tensile strenght.	E	In-Plane Shear strength	In-Plane G12
M21/35%/268/T700GC-UD	1.58 g/Cm^3	105 MPa	1465 MPa	119 GPa	2375 MPa	148 Gpa	95 Mpa	4.5 Gpa

Table 17 – Desired properties for Landing Gear leaf spring

Max. Weight (grams)	180
Max. Density	1.58
Max. Volume (cm3)	113.92
thickness (cm)	0.848
nº of layers	32

In order to choose the stack for this landing gear, staking commendations mentioned in 3.3.3 were taken in concern. (It's important to mention that the material used is Unidirectional) (DEFENSE S.D.).

The great advantage of this software is that is possible to study more than one stacking at the same time and with different geometries (varying *b*).

This software has as inputs:

- Properties of the material;
- Geometry properties of the landing gear;
- Matrix of stacking (in order to test/study more than one stacking at the same time)

The output of this software is:

- Stress in the critical zone of the landing gear;
- Deflections (vertical and horizontal) on the wheel zone of the landing gear;

Where:

- *b* is a variable [mm]
- *v* is vertical deflection [mm]
- *h* is horizontal deflection [mm]
- *s* is the stress [MPa]

The software code is located in the attachments pages of this thesis.

Different stacks were tested, taking account the previous defined requisites.

The selected composite stack was:

[45/-45/0/0/45/0/-45/90/45/-45/0/45/0/0/45/0/-45/45/90/-45/0/45/0/0/-45/45]

Where:

- 45 is a layer disposed with 45º

- -45 is a layer disposed with -45º

- 90 is a layer disposed with 90º

- 0 is a layer disposed with 0º

The results for this stack were inside the envelope that was imposed and was lighter than others stacks that were tested.

5.3. Detailed design

5.3.1. Design

After choosing and validating the general geometric properties and stack, it was necessary to detail the design, adding joints, axles, fasteners and also the wheel. . Landing gear parts were developed using Solidoworks® and CATIA® software.

Some typical sheet-metal design rules were taken in consideration according to (TOOL 2017).

- Distance between holes center must be at least 4 times the diameter of those holes.
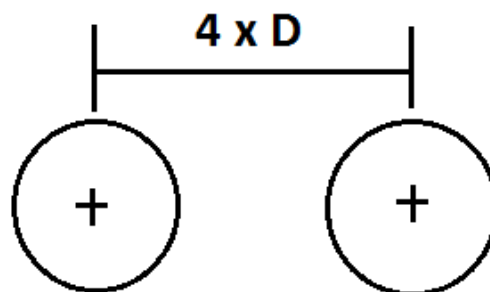
Figure 96 - Minimum distance between holes - (2017, January).

- "For a hole < 1" in diameter the minimum distance "D" = 2T + R"

Where R is the bend radius.
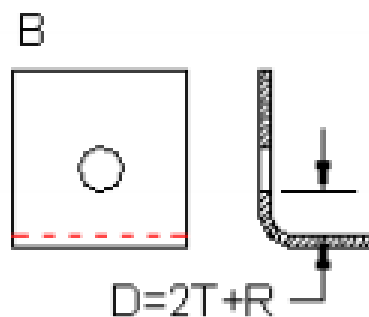
Figure 97 - Design sheet metal rules – forming near holes - tool, Q. (2017, January).

The first step was to update the landing gear spring leaf to a more aerodynamic shape (so that drag was decreased). these modifications were then tested and validated by FEM simulations.

Note: Technical designs of the produced objects can be found in the attachments.

The 3D spring leaf representation can be found in Figure 98:
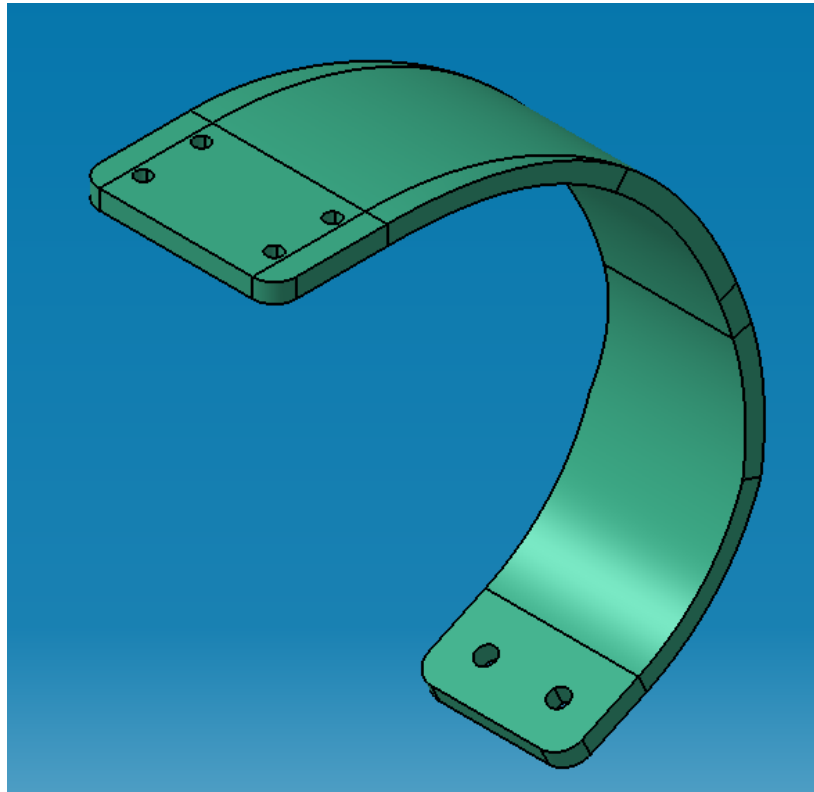
Figure 98 - Carbon Leaf Spring - 3D Representation - CATIA® Software

Then it was necessary to study the wheel and aircraft joints. These parts were designed to use the already existing connections of the old landing gear. The fork is the part that connects the wheel axle to the composite leaf spring.

The 3D Fork representation can be found in Figure 99:
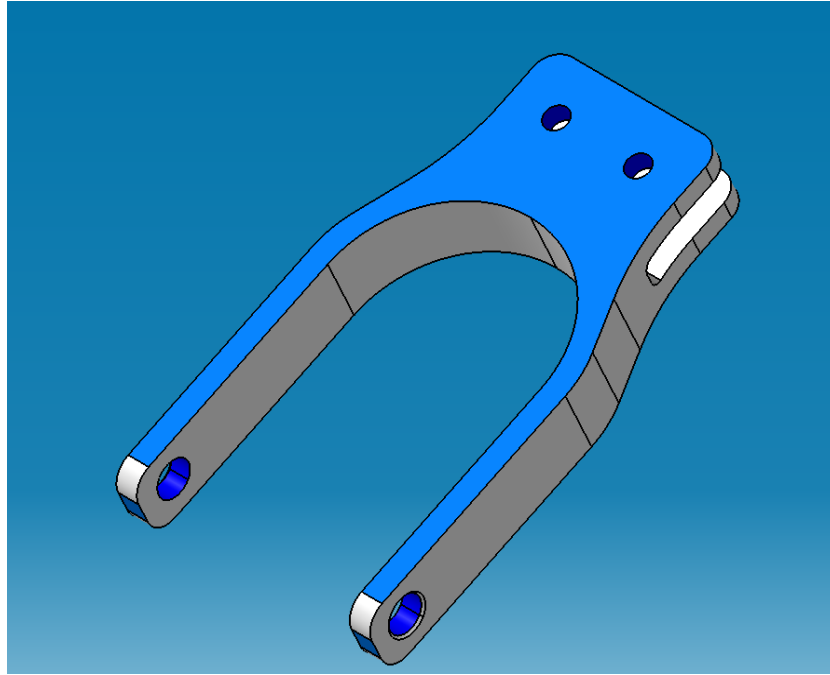
Figure 99 - Fork - 3D Representation - CATIA® Software

Figure 100 and Figure 101 represent under and upper plates that connect the landing gear to the existing parts of the aircraft by mean of screws.
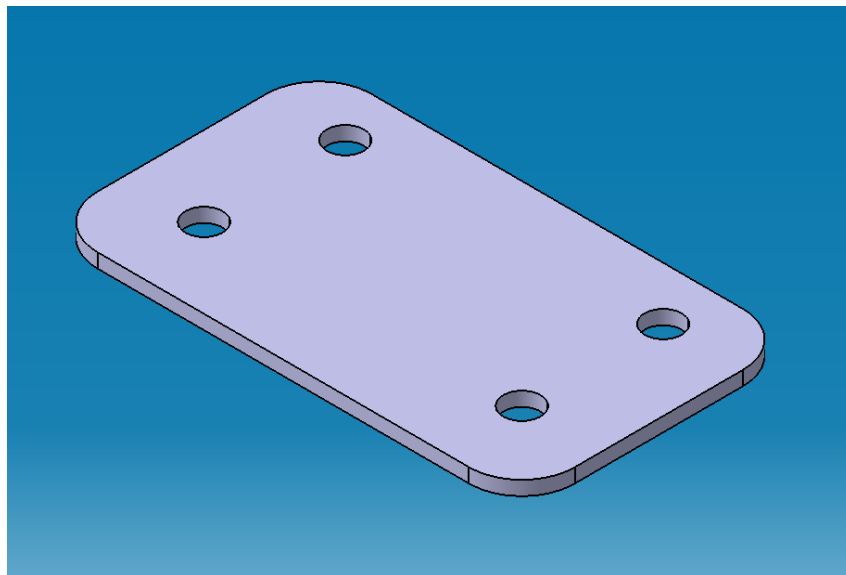
Figure 100 - Down Plate - 3D Representation - CATIA® Software
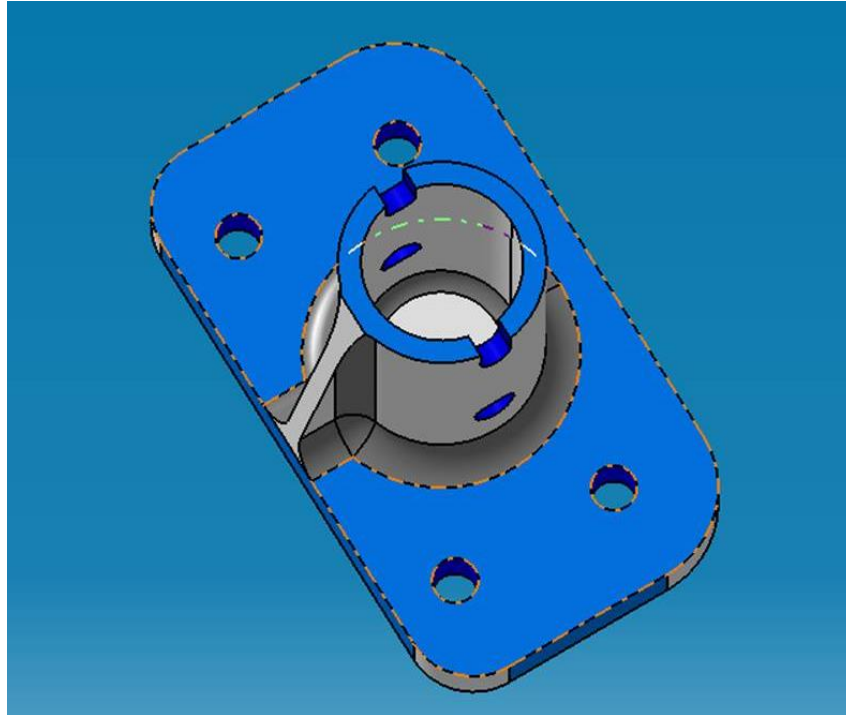
Figure 101 - Upper plate - 3D Representation - CATIA® Software

In Figure 102, it's possible to observe the landing gear setup (almost completed).
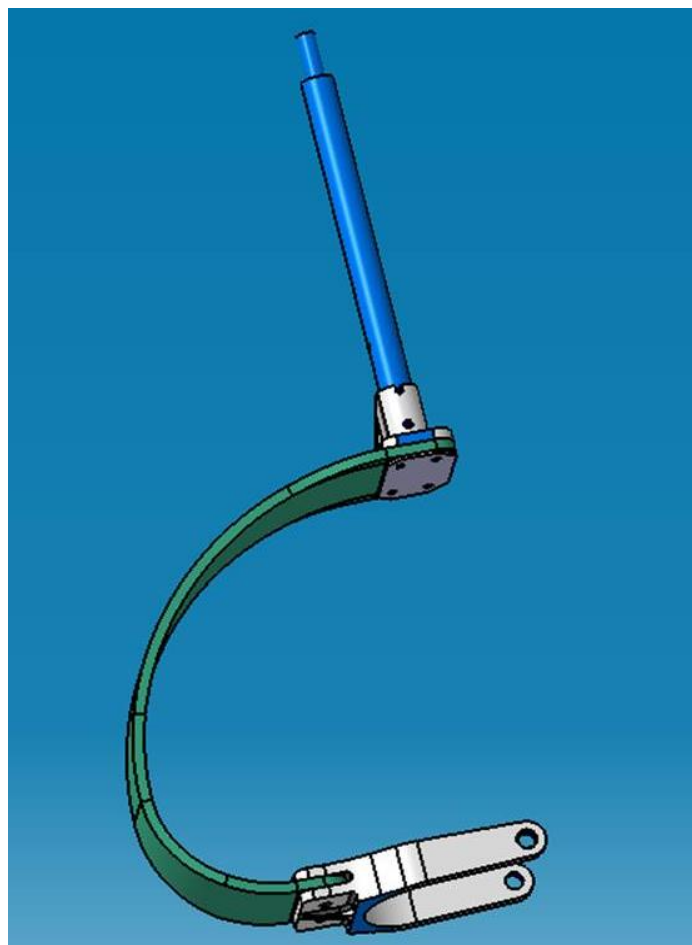
Figure 102 - Landing gear partially completed – CATIA® Software

The detail of the connector arm to the servo it's possible to be checked in Figure 103.

Figure 103 - Connector arm to the servo – Solidworks® Software

Note : Servo is a small motor that controls the direction of the landing gear.

After designing, it was necessary to repeat a new FEM simulation so that everything was checked and validated or in last case, improved (parts that what would had failed).

5.3.2. FEM properties

In Figure 104, Figure 105 and Figure 106 it is possible to check the groups of assemblies and part numbers of the nose landing gear system.
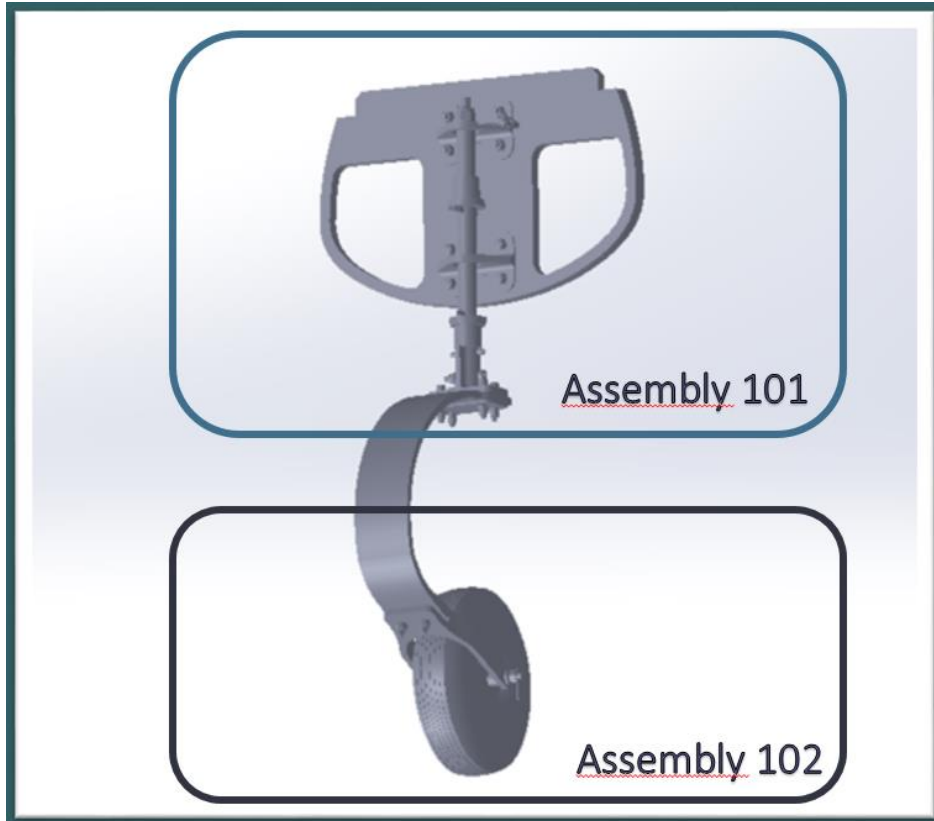
Figure 104 – Map of assemblies of the landing gear structure
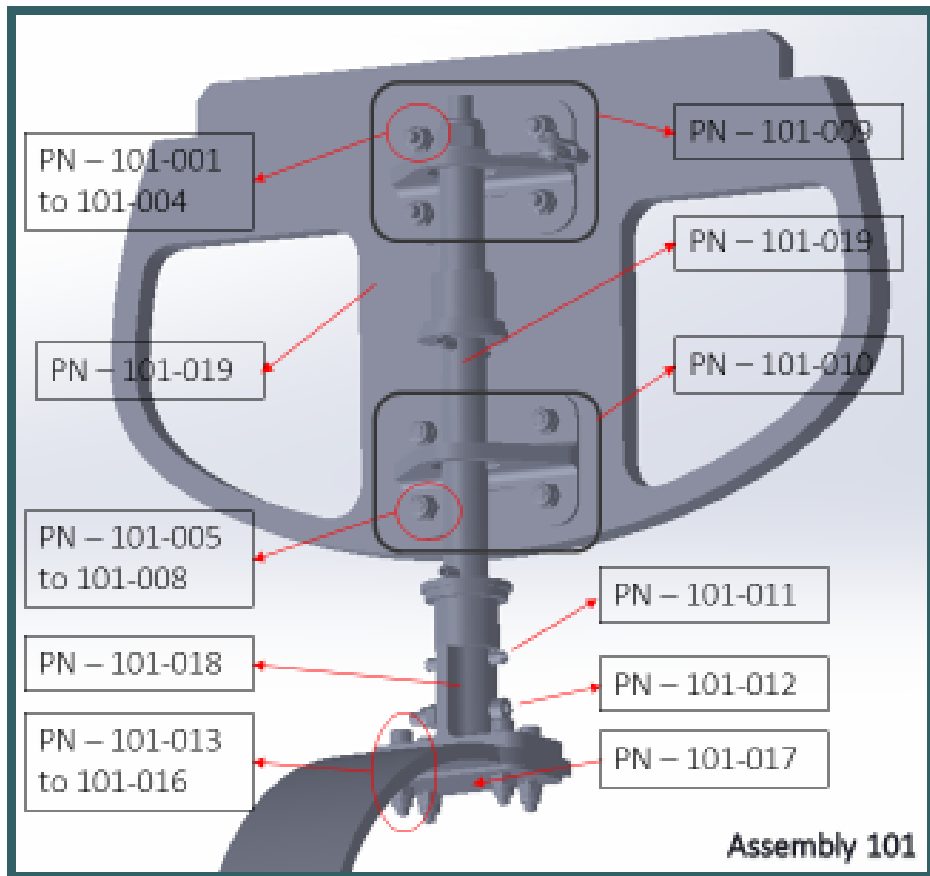
Figure 105 – Assembly 101 – Landing gear parts identification
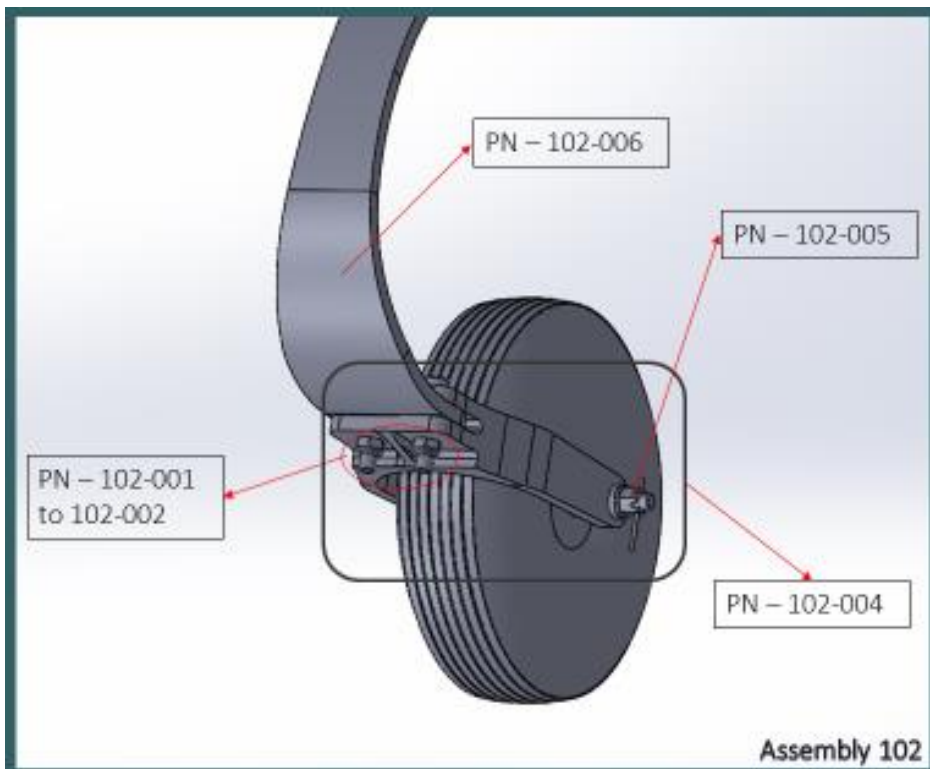
Figure 106- Assembly 102 – Landing gear parts identification

1) **Composite leaf**

The composite leaf was computed with PCOMP property using hyper-laminate add-in, introducing the information of the chosen stack. The representation of the carbon leaf spring can be checked in Figure 107.

Table 18 – Composite Leaf FEM details

Element Type	CQUAD
Element Size	10
Number of elements	174
Number of nodes	210
Property ID	PCOMP5
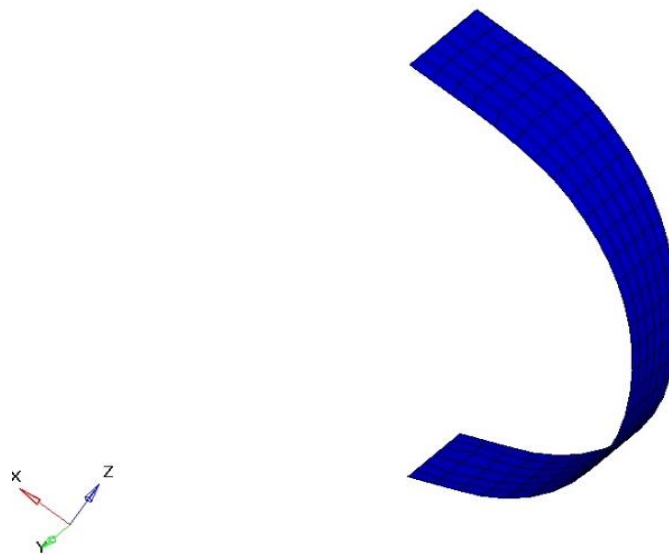
Figure 107 – Composite Leaf Spring represented by PCOMP property

2) Fuselage composite frame

The representation of the fuselage composite frame can be checked in Figure 108.

Table 19 – Composite frame FEM details

Element Type	CQUAD
Element Size	10
Number of elements	217
Number of nodes	282
Property ID	PCOMP6
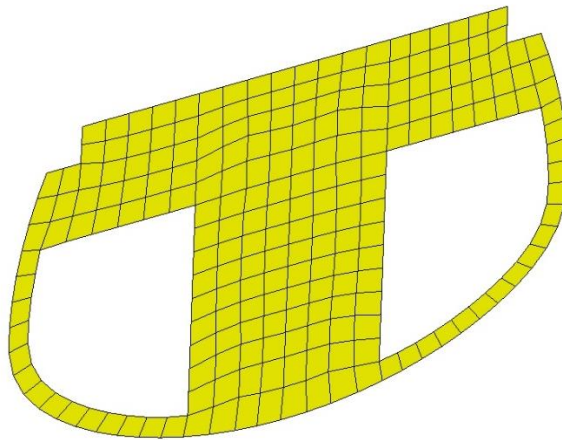
Figure 108 – Composite frame that couples the entire structure of the landing gear represented by PCOMP property

3) Landing gear Fork

The fork accommodates the wheel axle and is connected to the composite leaf spring.

The representation of the landing gear fork can be checked in Figure 109 and Figure 110.

Table 20 – Fork FEM details

Element Type	CQUAD
Element Size	10
Number of elements	130
Number of nodes	169
Property	PSHELL9
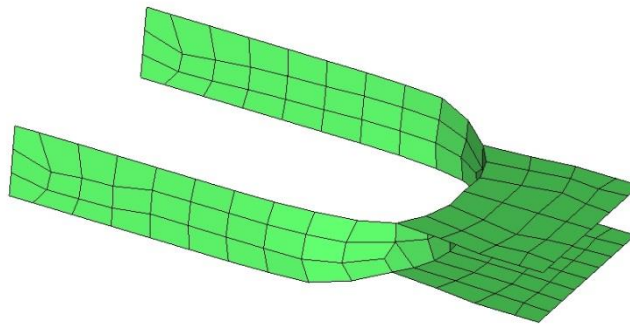
Figure 109 – Fork represented by PSHELL property.
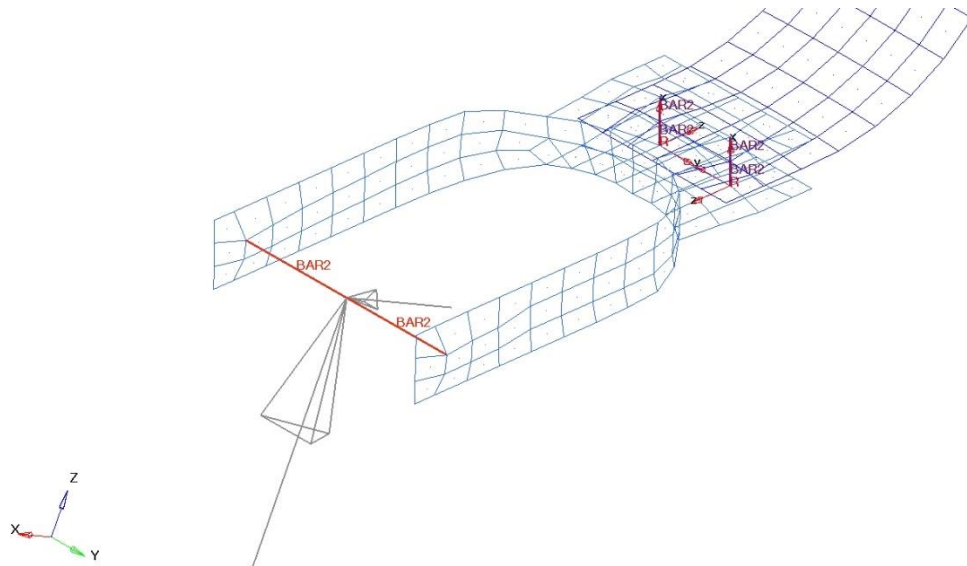
Figure 110 - Fork represented along with connections: Axle and composite leaf spring.

4) Connection Plates

These metallic plates connect the main vertical axle to the composite wall of the fuselage.

The representation of the connection plates can be checked in Figure 111, Figure 112 and Figure 113.
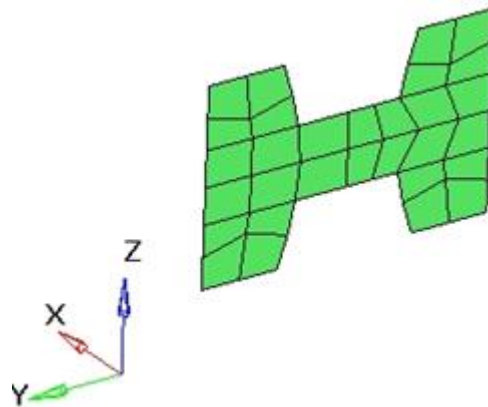
Figure 111 – Vertical part of the connection plate

Table 21 – Vertical part of the connection plate FEM Details

Element Type	CQUAD
Element Size	10
Number of elements	30
Number of nodes	48
Property	PSHELL 112
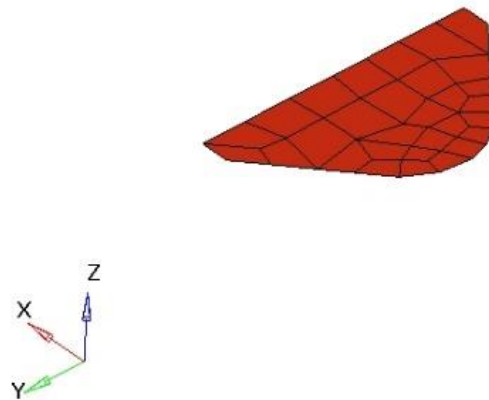
Figure 112 – Horizontal part of the connection plate

Table 22 - Horizontal part of the connection plate FEM Details

Element Type	CQUAD
Element Size	10
Number of elements	30
Number of nodes	42
Property	PSHELL 106
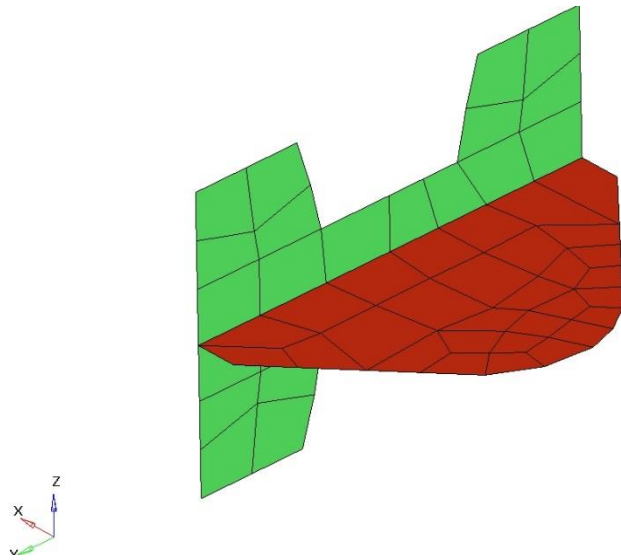
Figure 113 – Connection plate represented with PSHELL property

5) Up plate conector

The representation of the up plate connector can be checked in Figure 114.
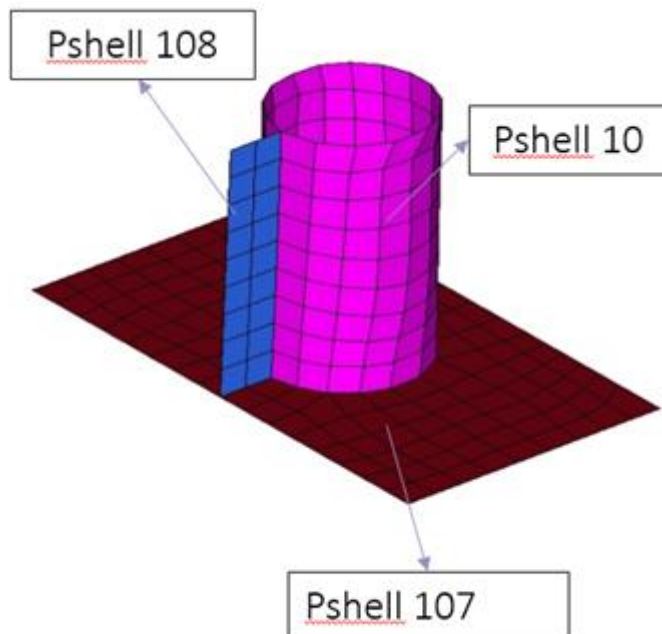
Figure 114 – Completed up plate represented with PSHELL property

Table 23 – Up Plate connector part of the connection plate FEM Details

Element Type	CQUAD
Element Size	10
Number of elements	321
Number of nodes	347
Property	PSHELL 108, 10 and 107

6) Down Plate

The representation of the down plate connector can be checked in Figure 115.
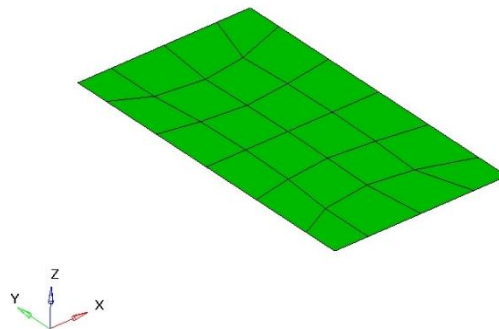
Figure 115 – Down plate represented with PSHELL property

Table 24 - Down Plate part of the connection plate FEM Details

Element Type	CQUAD
Element Size	10
Number of elements	24
Number of nodes	35
Property ID	PSHELL3

Detail of assembly between up and down plate

The representation of the assembly between up and down plate connectors can be checked in Figure 116.
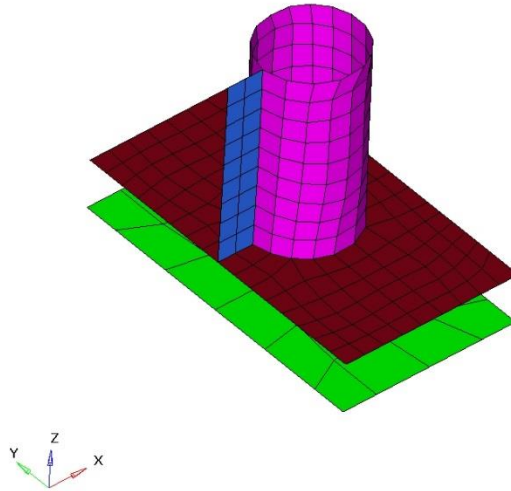
Figure 116 - Detail of assembly between up and down plate

7) **Entire Structure**

The representation of the entire landing gear structure can be checked in Figure 117.
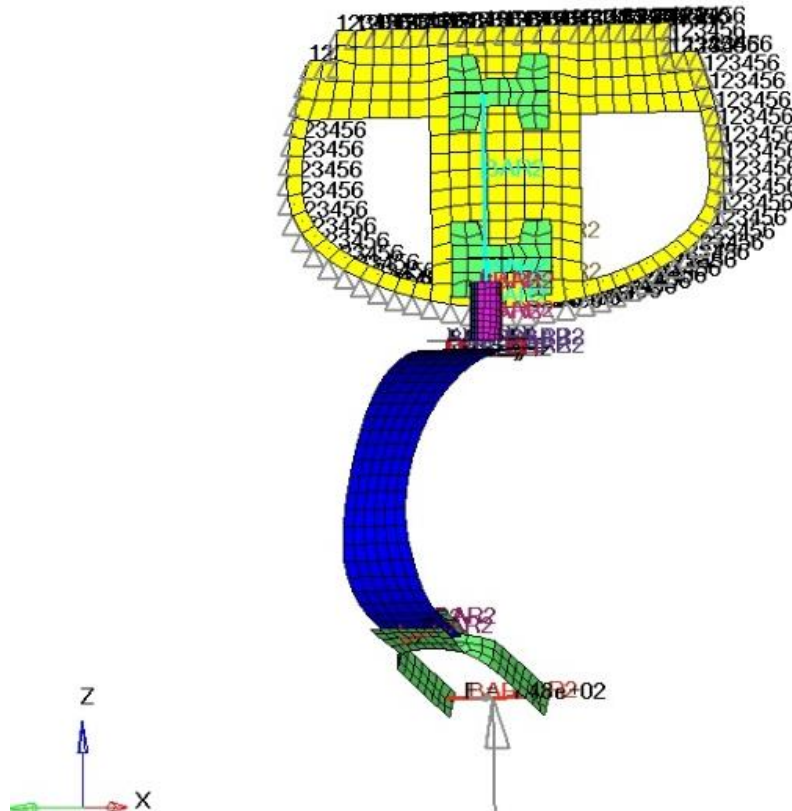
Figure 117 – Representation of the entire structure in a FEM model

Element Type	CQUAD
Number of elements	1015
Number of nodes	1210

Forces

The two forces (horizontal and vertical) were applied in the center of the wheel axle (that is represented by two CBARs with property ID PBARL 91). This values for the forces were considered taking account the formulation of loads Vnose and Dnose calculated in chapter - *3.1.1 Identification of Landing Gear requirements*.

The representation of the applied forces can be checked in Figure 118.
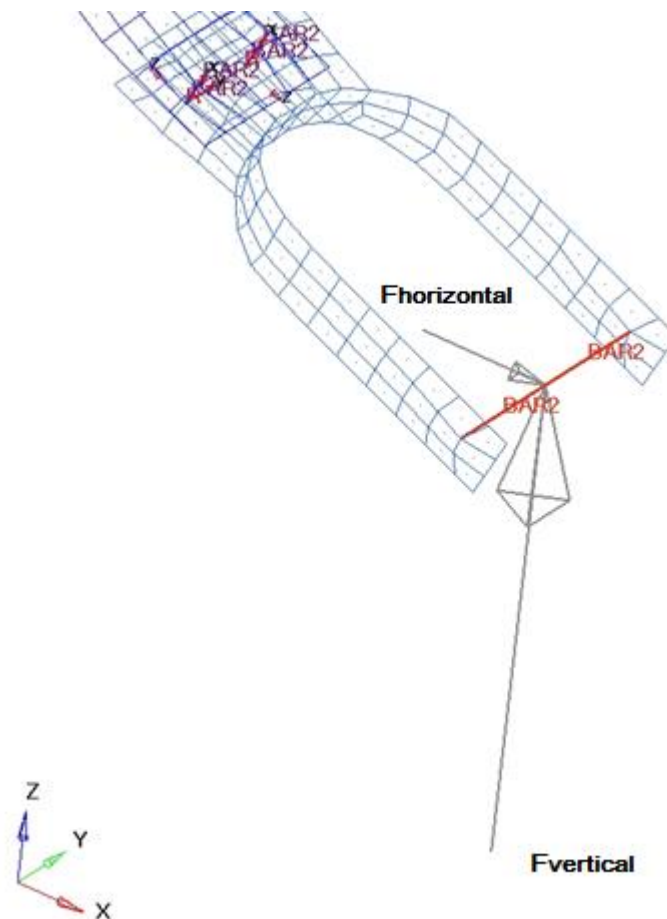
Figure 118 – Representation of the applied forces

Table 25 – Applied forces

Force Identification	Magnitude [N]
Horizontal	137
Vertical	502
Horizontal (with Safety Factor)	208
Vertical (with Safety Factor)	753

Boundary conditions

Fixed conditions were introduced around the frame that couples the landing gear to the rest of the fuselage as can be checked in Figure 119.
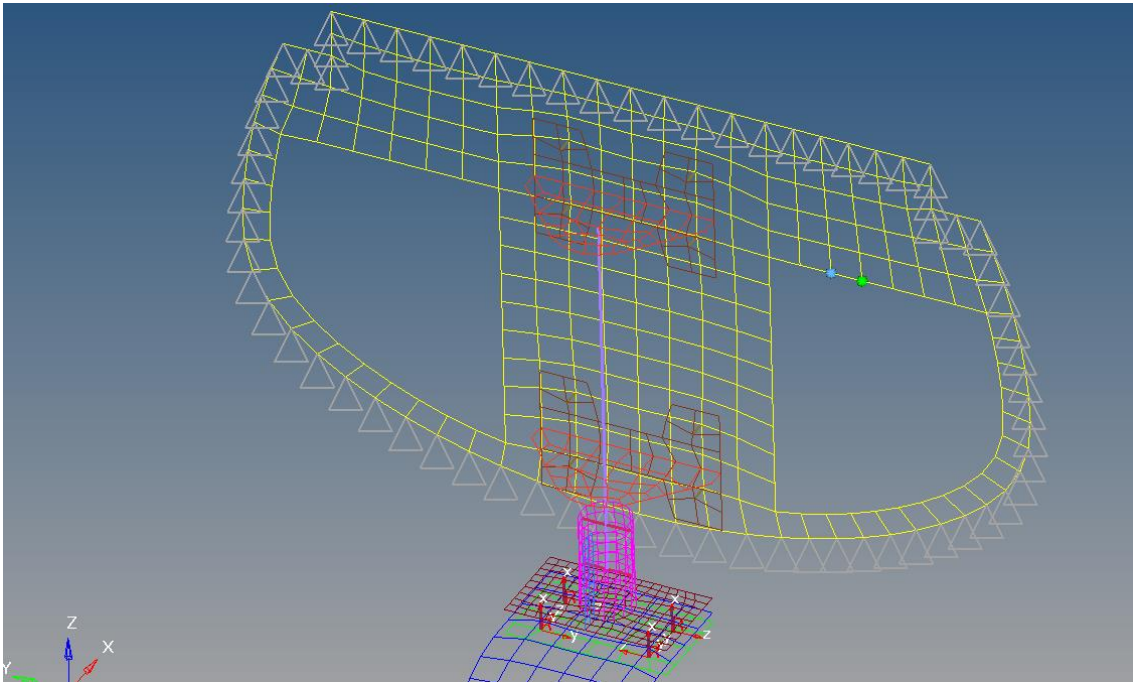
Figure 119 – Detail of the boundary conditions around the composite frame

Connection between elements of different pieces

In cases where the connection between different pieces existed, it was necessary to impose that a node of the PSHELL should be coincident with the CBAR. As it is possible to observe in Figure 120 a CBAR connected to the horizontal connection plate.
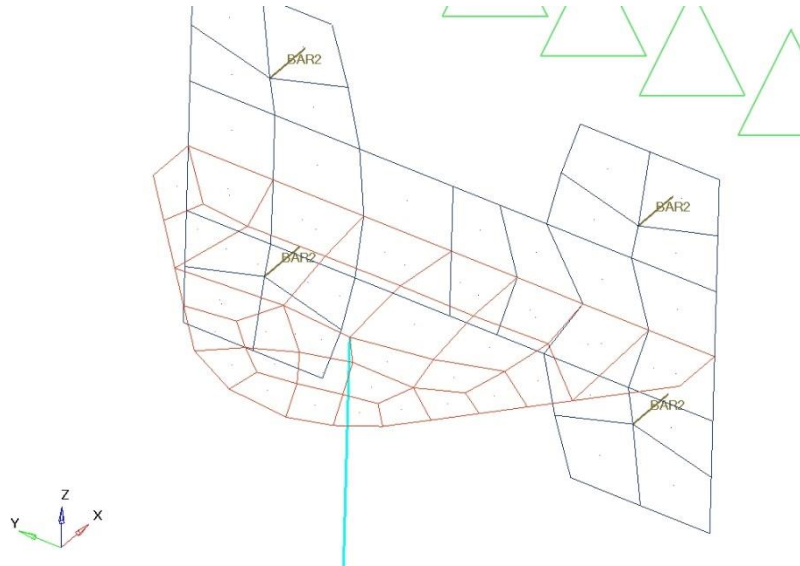
Figure 120 – Detail of different elements connection

Fastener connections

Fasteners were considered as CBARs to connect two or more different pieces/materials as it is possible to check in Figure 121.
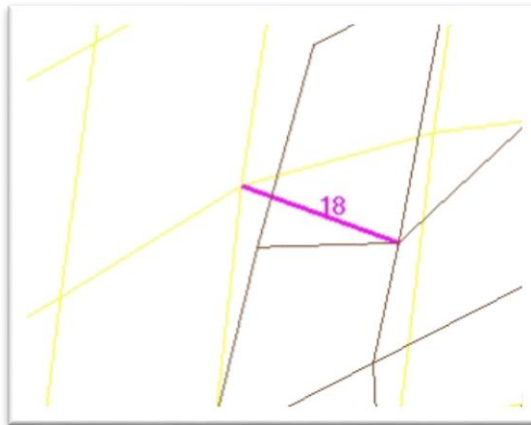
Figure 121 – Fastener connections between two different pieces in FEM model

The resume tables of properties and materials for each piece can be found in Table 26, Table 27 and Table 28.

Composite parts:

Table 26 – Composite parts present in the landing gear structure

Part Name	Part Number	Prop_ID	MAT_ID
Wall Frame - Sandwich	PN – 101-019	PCOMP06	MAT8_5 + MAT8_6
Leaf Spring	PN – 102-006	PCOMP05	MAT8_4

Metal parts:

Table 27 – Metallic parts present in the landing gear structure

Part Name	Part Number	Prop_ID	MAT_ID
Horizontal metal suport	PN – 101-009 and PN – 101-010	PSHELL106	MAT1_10
Vertical metal suport	PN – 101-009 and PN – 101-010	PSHELL112	MAT1_11
Small vertical cilinder	PN – 101-018	PSHELL10	MAT1_2
Vertical Cilinder membrane	PN – 101-018	PSHELL108	MAT1_2
Horizontal plate	PN – 101-018	PSHELL107	MAT1_2
Inferior horizontal plate	PN – 101-017	PSHELL3	MAT1_1
Fork	PN – 102-004	PSHELL9	MAT1_1

CBARs:

Table 28 – CBARs present in the landing gear structure

Part Name	Part Number	Prop_ID	MAT_ID
Wheel axle	PN – 102-005	Pbarl_91	Mat1_3
Fasteners: Fork-leaf	PN – 102-001 to 102-002	Pbarl_18	Mat1_3
Fasteners: leaf - up plate	PN – 101-013 to 101-016	Pbarl_7	Mat1_3
Fasteners: Wall frame, metal suports	PN – 101-001 to 101-004	Pbarl_103	Mat1_3
Main vertical axle	PN – 101-019	Pbarl_4	Mat1_1
Horizontal Pin 1	PN – 101-011 and PN – 101-012	Pbarl_1	Mat1_3

The identification of isotropic materials can be found Table 29:

Table 29 – Isotropic materials present in the landing gear structure

MAT_ID	E (Mpa)	poisson	Material
MAT1_1,MAT1_2,MAT1_11, MAT1_10	70000	0.33	Aluminium
MAT1_3, MAT1_12	210000	0.3	Steel

The identification of orthotropic materials can be found Table 30:

Table 30 – Orthotropic materials present in the landing gear structure

MAT_ID	E1 (Mpa)	E2(Mpa)	Nu12	G12 (Mpa)	G1Z (Mpa)	G2Z (Mpa)	Xt (Mpa)	Xc (Mpa)	Yt (Mpa)	Yc (Mpa)	S (Mpa)
MAT8_4	148000	9362.121	0.3	4500	4500	4500	2375	1465	38.423	142.85	95
MAT8_6	45	45	0.022	22			1.3	1.3	1.3	1.3	0.8
MAT8_5	38000	38000	0.09	2667			389	280	389	271	50

Where:

- Mat8_4 – PrePreg UD used for the landing gear leaf spring

- Mat8_5 – Carbon Fiber used in the sandwich structure of the fuselage frame

- Mat8_6 – Airex used in the sandwich structure of the fuselage frame

The properties of the pieces can be divided in: PSHELL and PBARL (dim is the radius of the fastener):

Table 31 – PSHELL properties

Properties	Thickness [mm]	Properties	Thickness [mm]
PSHELL2	1.5	PSHELL111	1.5
PSHELL3	1.6	PSHELL112	2
PSHELL9	8	PSHELL12	5
PSHELL10	4	PSHELL13	2
PSHELL107	5	PSHELL106	5
PSHELL108	4	PSHELL115	5
PSHELL110	1.6	PSHELL116	4

Table 32 – PBARL properties

Properties	Type	Mat ID	dim (mm)
PBARL18	ROD	3	3.5
PBARL7	ROD	3	2
PBARL103	ROD	3	2
PBARL91	ROD	3	2.5
PBARL102	ROD	2	7
PBARL96	ROD	3	2
PBARL19	ROD	12	2.5
PBARL8	ROD	12	2
PBARL109	ROD	12	2
PBARL92	ROD	12	2.5
PBARL104	ROD	11	7
PBARL97	ROD	12	2
PBARL1	ROD	3	3
PBARL4	ROD	1	7

5.3.3. FEM simulations

The results were processed in NSC Nastran® and then were analysed graphically in HyperView®.

Stress Von Mises – Valid of metallic parts.
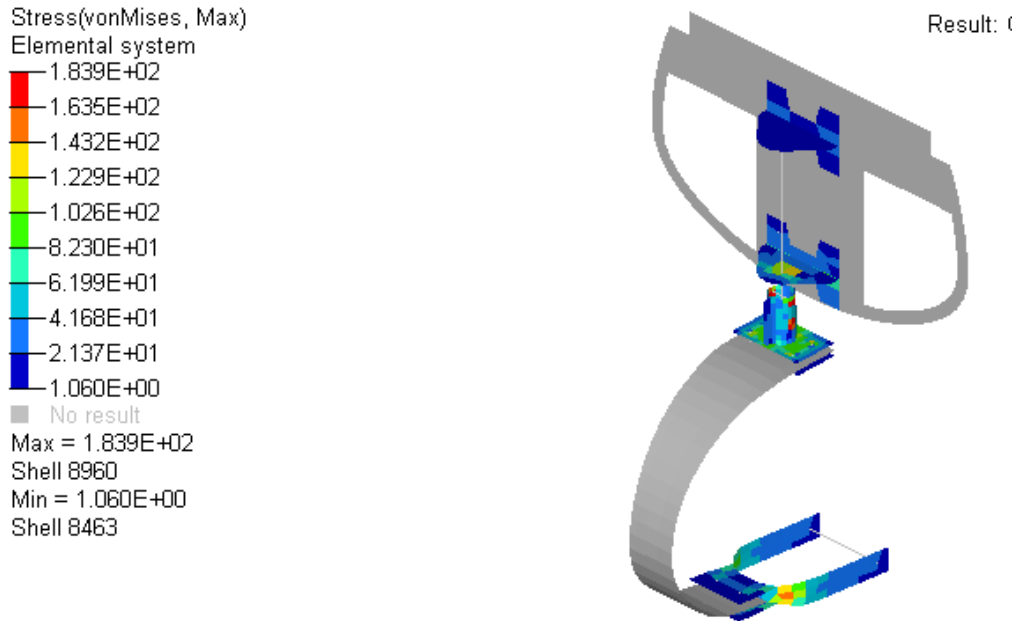
Figure 122 - Von Mises Stress - Hyperview Software®

Composite stress results – Carbon Fiber leaf-spring – PATRAN software
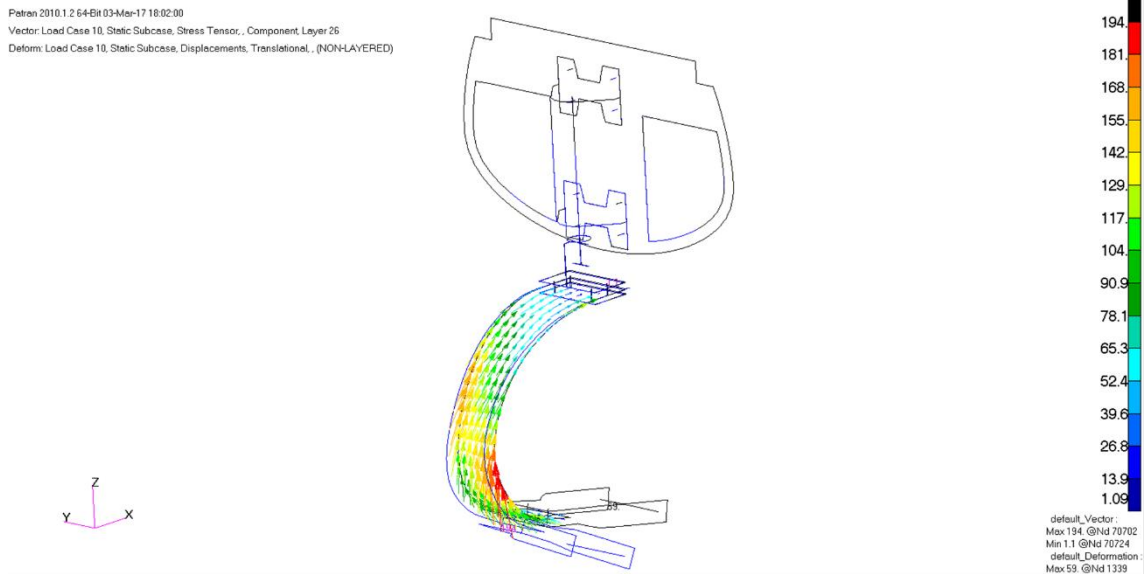
Figure 123 – Stress Results for the composite leaf spring - PATRAN®

Failure Index

For composite stress there is an index in Hyperview® software entitled Failure index. This index deals with macro level results – it is an individual ply failure index and must be always less than 1.

"Tsai-hill" and "Tsai-Wu" failure criterias that were mentioned before in chapter 3.3.6.2 , were considered for the calculations.

This failure index might be applied for direct stress or for inter-laminar stress. Inter-laminar stress is based on the first-order shear deformation laminated plate theory. For the Failure Index simulations it was considered the safety factor on the applied forces as it is the only way to simulate the ultimate strength in terms of failure index (as it is a factor it cannot be multiplied by 1.5).

Direct stress – Tsai Hill
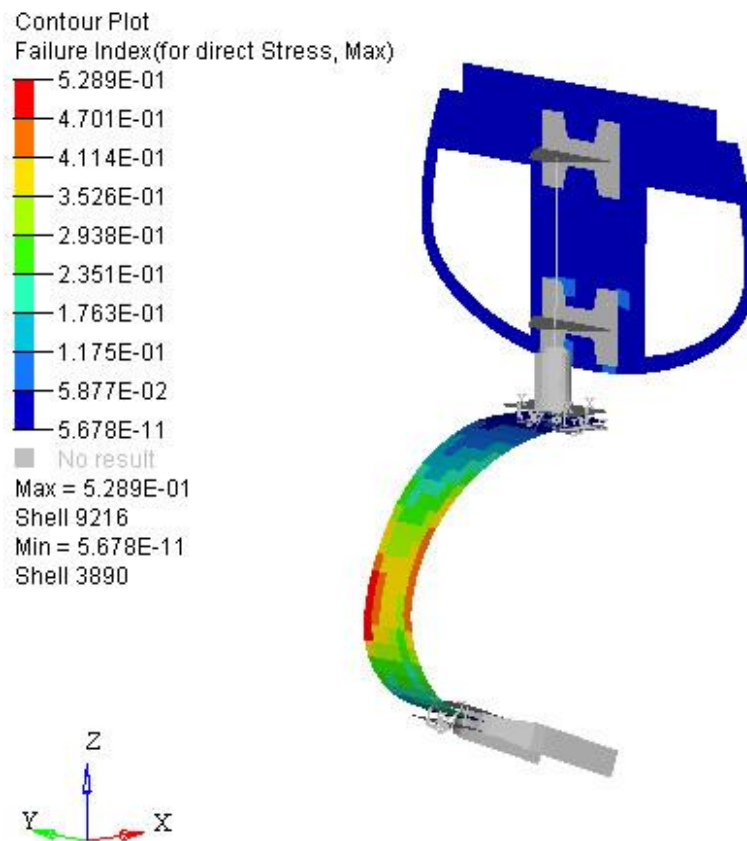
Figure 124 - Failure index - direct stress – Tsai-Hill criteria - Hyperview Software®

Direct stress – Tsai Wu
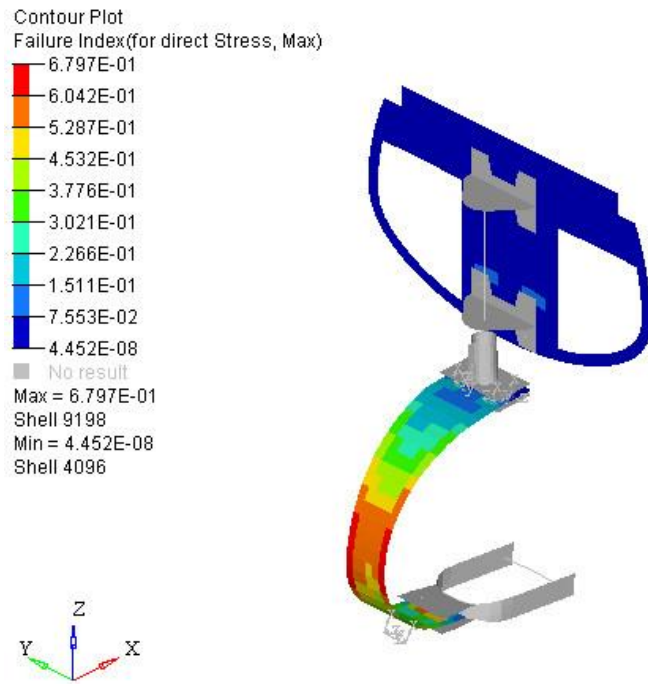
Figure 125 - Failure index - direct stress – Tsai-Wu criteria - Hyperview Software®

Inter laminar stress – Tsai Hill
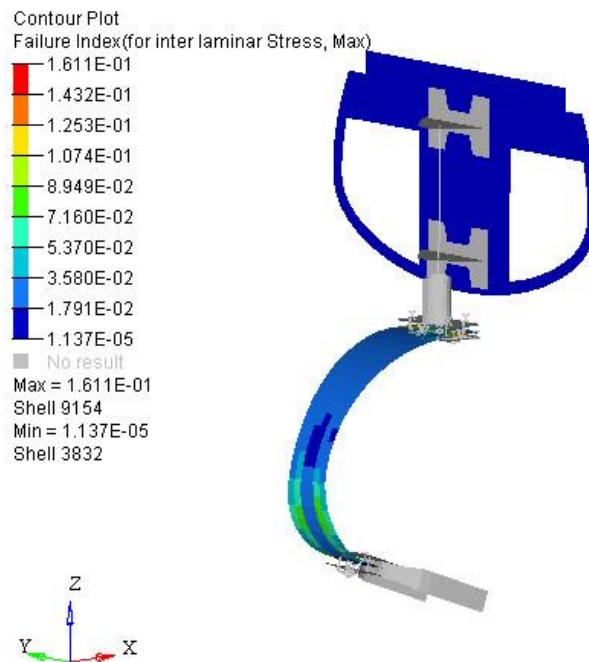
Figure 126 - Failure index - inter laminar stress – Tsai-Hill criteria - Hyperview Software®

Inter laminar stress – Tsai Wu
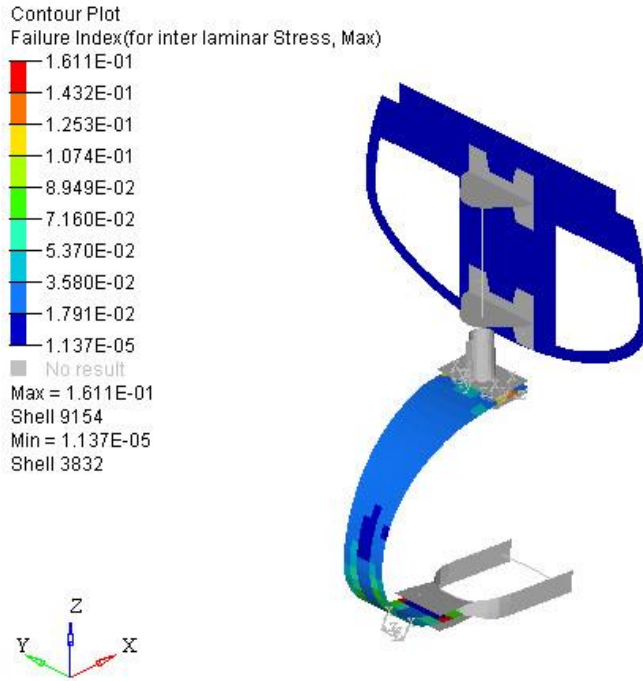
Figure 127 - Failure index - inter laminar stress – Tsai-Wu criteria - Hyperview Software®

Displacements

To compute displacements it was not considered the safety factor of 1.5 on the forces. The values for horizontal and vertical displacement can be checked in Figure 128 and Figure 129 and are summed up in Table 33.

Horizontal
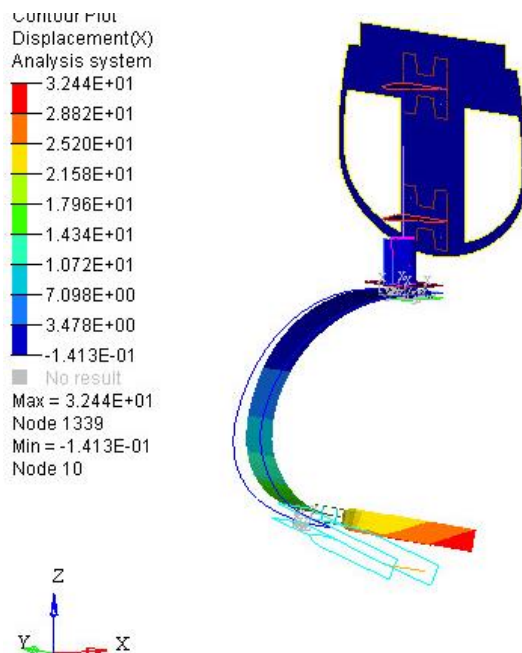
Figure 128 - Horizontal Displacement - X direction - Hyperview Software®

Vertical
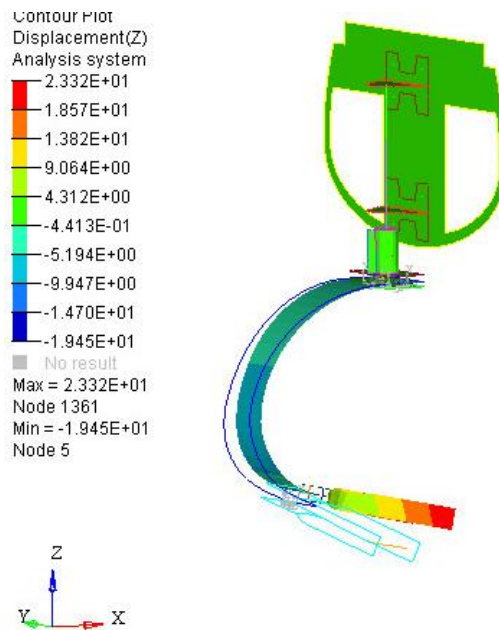
Figure 129 - Vertical Displacement - Z direction - Hyperview Software®

Table 33 – Maximum displacements for a simultaneous vertical of 502N and horizontal load of 137N

	Max. Displacement. [mm]
Horizontal	32
Vertical	23

All the results are summed up in Table 34:

Table 34 – Results of FEM simulation – Landing Gear complete

With Safety Factor	Failure index - Direct Stress -Hill	0.59
	Failure index - Inter-laminar -Stress - Hill	0.16
	Failure index - Direct Stress - Wu	0.68
	Failure index - Inter-laminar -Stress - Wu	0.16
Without Safety Factor	Von Mises Stress [MPa]	97.09
	Composite Stress P1 [MPa]	273.4
	Horizontal displacement [mm]	32
	Vertical displacement [mm]	23

As the maximum Von Mises stress is lower than the tensile yield stress of Al 7075 T6, Ck45 steel and Al 2024 and failure index for both direct and inter-laminar stress were lower than 1 (for both failure criterions) for these tests, the landing gear is validated. In the next chapters bearing, shear and axial stress will be analysed.

5.3.4. Bearing stress calculation

In this study it was found cases of single shear and double shear forces. Double shear exists for instance in the connection between the aluminium fork and the composite leaf and also between the composite leaf and the up and down plates.

In order to analyse double shear situations two methods will be considered, with the aim of double checking the results and to assure that no mistakes were committed:

- Grid Point Forces
- CBAR forces

As explained in chapter 4.3.1, the output of shear stress is divided in two components, shear in plane 1 and shear in plane 2, as can be checked in Figure 130.
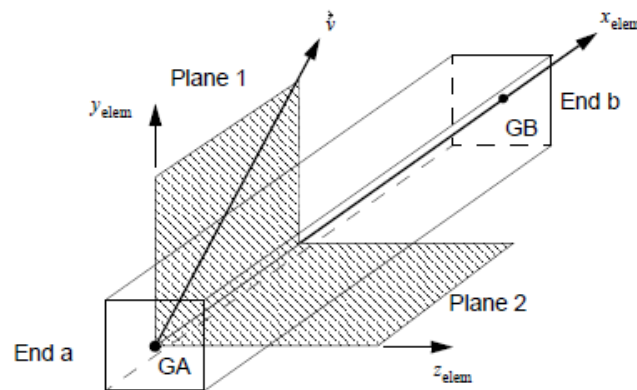
Figure 130 - CBAR Element Geometry - (MSC Software 2013)

Grid Point Forces needed a transformation of coordinate system because all the stress values were calculated considering the global system and not the local system of the bar.

It was required to assign a local system to each bar as can be observed in Figure 131.
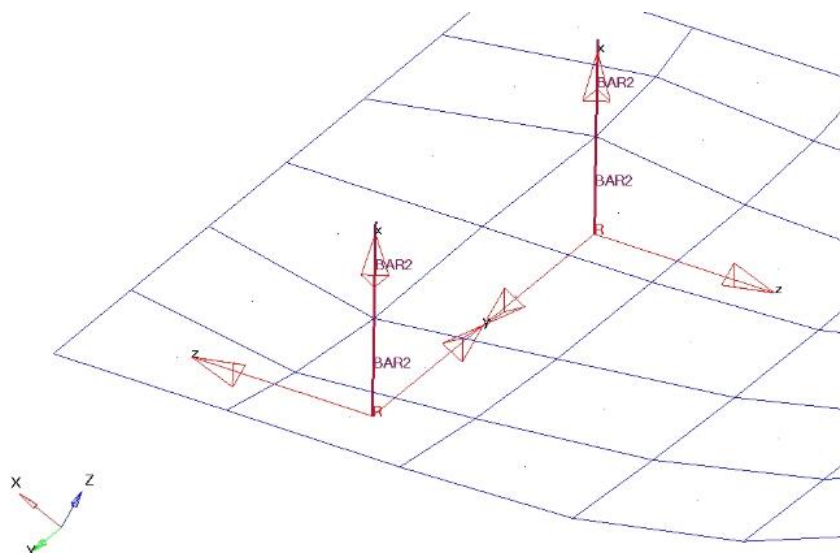
Figure 131 – Local Referential for each CBAR

To calculate bearing stress, auxiliary tables were created in Excel Software (see Annex C : Table 45, Table 46, Table 47 and Table 48).

All the bearing stress results respected the following condition:

$$1.5 \ \sigma_{Bearing} < \sigma_{allowable \ Bearing}$$

 It's possible to check some examples of calculations in Table 35, Table 36 and Table 37.

Table 35 – Maximum bearing stress

Part	El. ID	Diam.[mm]	Material	Thick.[mm]	σbr allwb[Mpa]	σbr limit[Mpa]	UL.F.	MSbr
SC 18-UAV fibre	18	4.0	Sandwich Carbon	0.3	378.0	83.37	1.5	2.02

In order to analyse double shear situation, two methods were considered as was referred in this chapter.

Grid Point Forces

Table 36 - Example of calculation of double shear forces – Grid Point Forces method

GP FORCES									
POINT-ID	ELEMENT-ID	T1	T2	T3		s1	s2	Axial	Double Shear
4	9	-1.72E+02	-3.88E+02	1.79E+03					
8	9	1.72E+02	3.88E+02	-1.79E+03		2.02E+02	-4.87E+01	1.72E+02	207.8
8	10	1.44E+02	-1.86E+02	1.75E+03					
6	10	-1.44E+02	1.86E+02	-1.75E+03					
3	12	-1.33E+02	-3.91E+02	-1.83E+03					
7	12	1.33E+02	3.91E+02	1.83E+03		2.02E+02	4.87E+01	1.33E+02	207.8
7	11	1.10E+02	-1.89E+02	-1.79E+03					
5	11	-1.10E+02	1.89E+02	1.79E+03					

Where for Grid Point Forces (GP Forces):

- T1 - Axial stress (= Axial)

- T2 - Shear stress in plan 1 (See Figure 130)

- T3 - Shear stress in plan 2 (See Figure 130)

- S1 = T2[element X] – T2[element y]

- S2 = T3[element X] – T3[element y]

- Double Shear $= \sqrt{S1^2 + S2^2}$

- Element X and Element Y are CBars that share a node and can be seen in an example in Figure 132

CBAR forces

Table 37 - Example of calculation of double shear forces – CBAR Forces method

Element ID	S1 [MPa]	S2 [MPa]	Axial [MPa]	Shear [MPa]	S1' [MPa]	S2' [MPa]	Double Shear [MPa]
9	1794	-388	171	1835	49	-202	208
10	1745	-186	-144	1755			

Where for CBAR Forces:

- Axial - Axial stress
- S1 - Shear stress in plane 1 (See Figure 130)
- S2 - Shear stress in plane 2 (See Figure 130)
- S1' = S1[element X] – S1[element y]
- S2' = S2[element X] – S2[element y]
- Double Shear stress = $\sqrt{S1^2 + S2^2}$

Element X and Element Y are CBars that share a node and can be seen in an example in Figure 132.
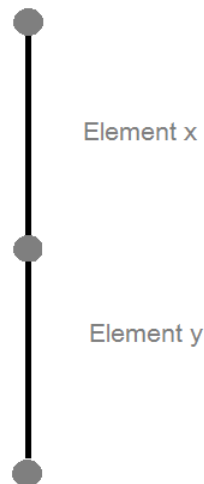
Figure 132 – CBAR example with 2 elements: X and Y

5.3.4.1 Critical Stress

When a fastener is subjected to shear and tensile loads at the same time, the combined load needs to be compared with the fastener strength. Usually load ratios and interaction curves (see Figure 133 and equation 174) are used for this situation (BARRETT 1990).
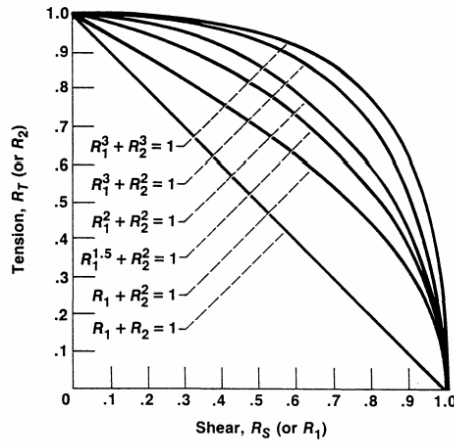
Figure 133 - Interaction Curves (Barrett 1990)

The most conservative interaction curve is:

$R_1 + R_2 = 1$

and the least conservative is:

$$R_1{}^3 + R_2{}^3 = 1$$

The project department of CEiiA provided an Excel Sheet that calculated the combined safety margin for a situation of shear and axial stress for a certain situation. This table sheet uses the safety margin relation found in equation 174 and in Figure 134. The results for each evaluated component can be found in Table 48.
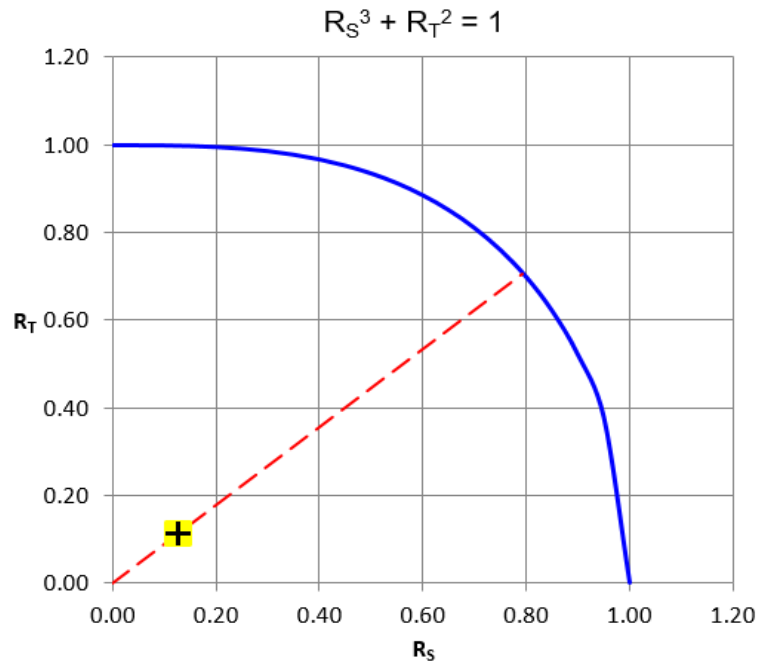
Figure 134 – Safety margin relation with Shear and Axial stress interaction

$$R_S{}^3 + R_T{}^2 = 1 \qquad (174)$$

Where:

- RT – Axial Tension load ratio (R2)

- RS – Shear Tension load ratio (R1)

$$R_T = \frac{Actual\ tensile\ load}{Allowable\ tensile\ load}$$ (175)

$$R_s = \frac{Actual\ shear\ load}{Allowable\ shear\ load}$$ (176)

Note: It was not found information about shear strength of the carbon steel CK45 but as is considered in (BURGUN 2003), shear strength for carbon steels can be:

$$F_{su} = 0.6 \times F_{tu}$$ (177)

Where F_{tu} , is tension strength.

The critical situations for bearing and shear-tension combined are described in Figure 135.

All the safety margins are higher than one so the structure will not have problems of bearing or shear + tension stresses.

Critical Bearing

Part	Element ID	Diameter [mm]	Material	Thickness [mm]	Bearing Allowable [Mpa]	Bearing Stress limit [Mpa]	UL.Fact.	MSbr
UAV fiber	18	4.0	Sandwich Carbon	0.3	378.0	83.37	1.5	2.02

Critical Fastener

Element ID	Fastener Type	Diameter[mm]	Shear Allowable [N]	Tension Allowable [N]	Tension Load [N]	Shear Load [N]	UL.Fact.	MS t+s
28	Ck45 small Pin	6	9576	16540	11	1578	1.5	3.04
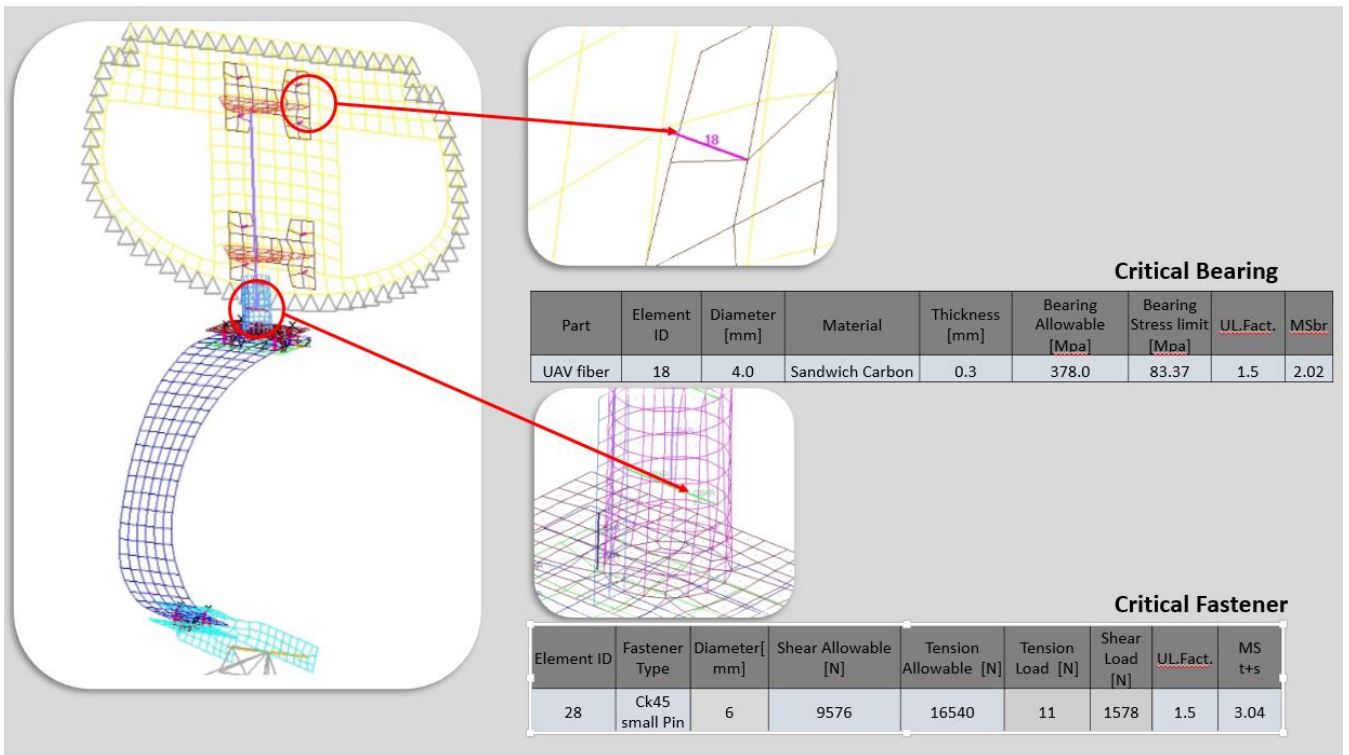
Figure 135 – Critical situations for bearing stress and fasteners (shear and tension)

6. Tests

Vertical Drop Test

According to (ADMINISTRATION 1967), the drop test must be prepared on the complete airplane, or on units consisting of wheel, tire, and shock absorber, in their proper relation, from free drop heights not less than those determined by the following formula:

$$h = 2.54 \times 3.6 \left(\frac{W}{S}\right)^{1/2} \quad [m] \tag{178}$$

But: $0.234 < h < 0.475$m

If wing lift is provided, the drop test can be performed with an effective weight:

$$We = W \frac{[h + (1 - L) * d]}{(h + d)} \quad [N] \tag{179}$$

Where:

- h – Drop height (Cm).
- d – Deflection under impact on the tire plus the vertical component relative to the drop mass (Cm).
- W – Wnose (N) – equal to the vertical component of the static reaction that would exist at the nose wheel, assuming that the mass of the airplane acts at C.G. and exerts a force of 1G down and 0.33G forward.
- L – Ratio of assumed wing lift to the airplane weight, but no more than 2/3.

Inertia load factor:

$$n = n_j \frac{w_e}{W} + L \tag{180}$$

Where:

- n_j - the load factor developed in the drop test (that is, the acceleration (dv/dt) in Gs recorded in the drop test) plus 1.0.
- We, W, and L - the same as in the drop test computation.

"The value of n determined in accordance with paragraph (e) may not be more than the limit inertia load factor used in the landing conditions" (ADMINISTRATION 1967).

Inertia load factor must be higher than 2.67, unless these lower values will not be higher during taxiing at speeds up to takeoff speed over terrain.

To find the mass that should be used to simulate the aircraft load on the moment of impact a simple method was used:

If all the potential energy is changed for kinetic energy (ignoring drag and other type of external forces) at the moment of impact we have:

$$\frac{1}{2} * m * v^2 = m * g * h \tag{181}$$

Where:

h – drop height [m]

m – mass of the body that falls [kg]

v – speed [m/s]

Simplifying:

$$v = \sqrt{2 * g * h} \quad [\frac{m}{s}]$$

If the vertical deflection is known by FEM then it's possible to obtain the time that the landing gear will deflect at that speed.

$$v = \frac{\Delta y}{\Delta t} \quad [\frac{m}{s}]$$

$$\Delta t = \frac{\Delta y}{\sqrt{2 * g * h}} \quad [s]$$

If the time to get null speed is known, it's easy to calculate deceleration:

$$a = \frac{\Delta v}{\Delta t} = \frac{0 - v}{\Delta t} \; [m/s^2]$$

$$Gs = \frac{g}{a}$$

- Where g stands for gravity acceleration [m/s^2]

As we know the vertical load that the landing gear will be subjected at the moment of impact and the number of Gs, it's easy to obtain the mass that should be used for the test.

$$mass = \frac{vertical\ reaction}{Gs} \tag{182}$$

To do all these calculations another program was developed in MATLAB®. The code can be found at the attachments.

The test-bed for this setup was designed in order to simulate an impact during the landing.

Two options are presented, one that include skids and other more economic that include plastic bushes.

Both versions were tested by FEM simulation using Hypermesh® and NASTRAN® software.

The impact test consists in a vertical moviment of the landing gear with mass on it, simulating a landing with leveled conditions.

This vertical moviment is assured by three rounded rails and it's started when 3 dowels are desingaged from those vertical rails.

Results:

<div align="center">Table 38 - Results for the G's calculation</div>

Weight [kg]	25.0
Surface Area [m^2]	2.4
Force [N] (horiz + vertical)	520.4
h [Cm]	13.4
hmin [Cm]	22.9
Speed [m/s]	2.1
dz [m]	0.048
Time [s]	0.022
Acel. [m/s^2]	94.4
Gs	9.6

$$mass = \frac{520.4}{9.6} = 54.2 \; N = 5.5 \; kg$$

Note: It was considered the combination of horizontal and vertical force:

$$Force = \sqrt{Vertical \; F^2 + Horizontal \; F^2}$$

In order to simulate both landing loads (vertical and horizontal), a ramp must be used as can be seen in Figure 136. Considering loads obtained in chapter 5, we have:

Figure 136 - Ramp to simulate two normal loads simultaneously

$$tang\ \theta = \frac{148}{548} \tag{183}$$

$$\theta \approx 15º \tag{184}$$

Test Base Designs:

Two slightly different options were designed. The first has skids to reduce drag on the rails to the minimum value (see Figure 137 and Figure 138). The second option is a little more economic because those skids are substituted by plastic bushes (see Figure 139 and Figure 140).
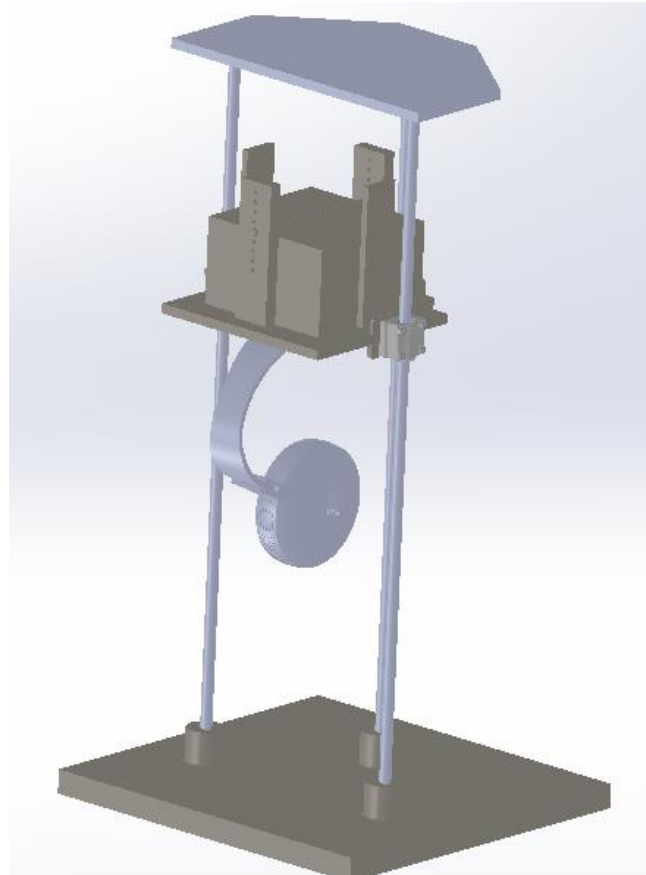
Figure 137 - First option of the test base
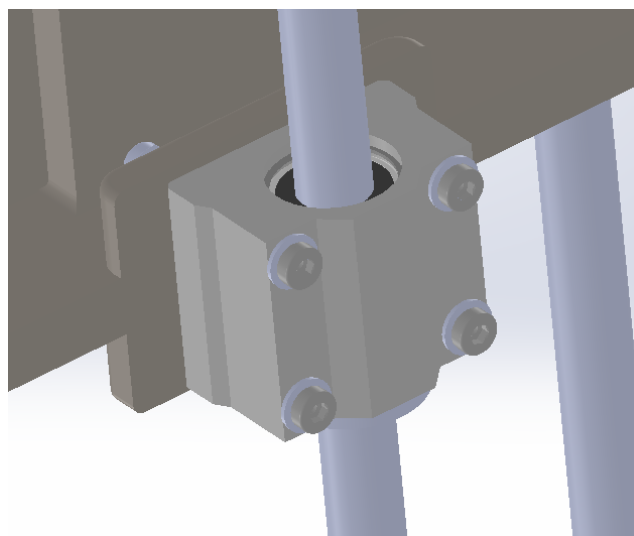
Figure 138 – Skid detail – First option of the test base
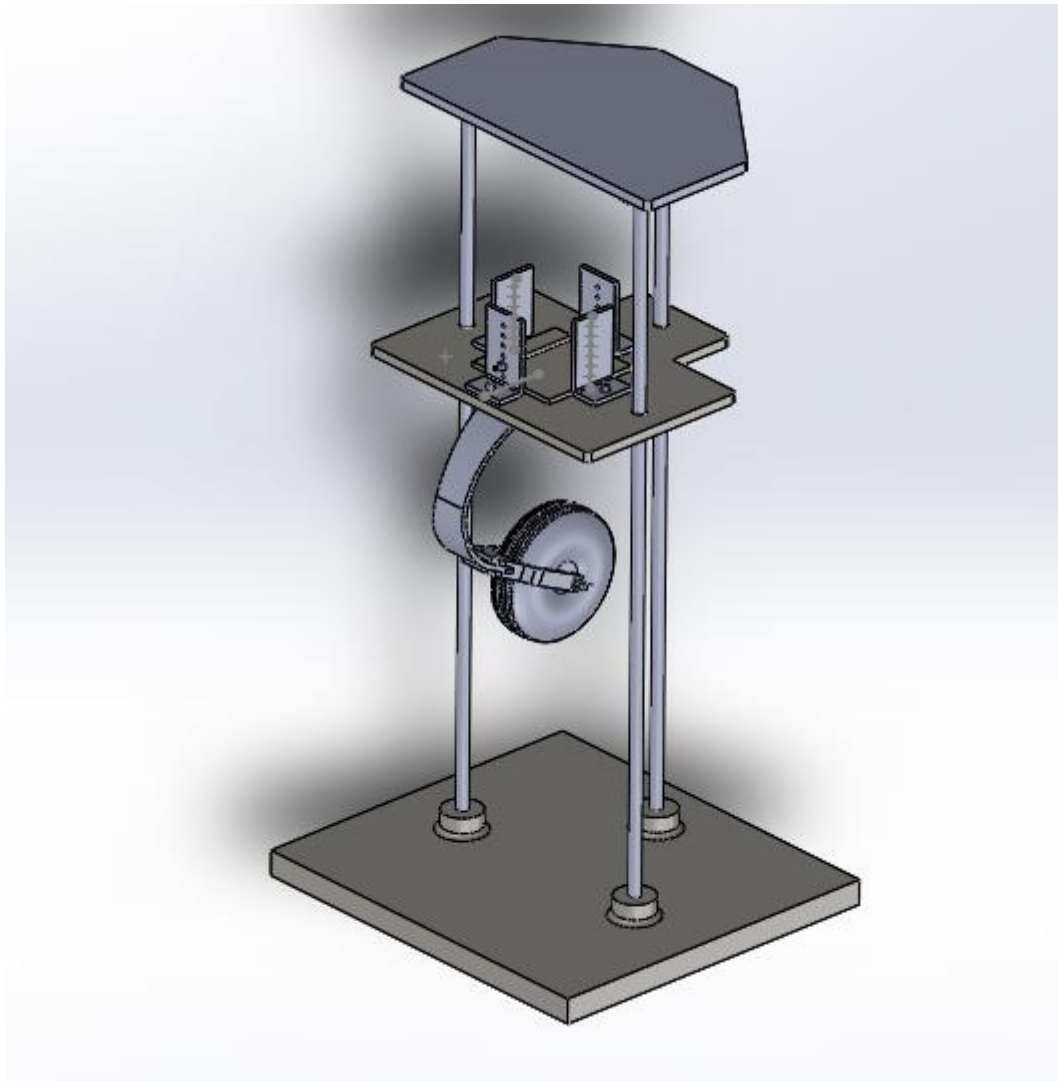
Figure 139 - Second option of the test base
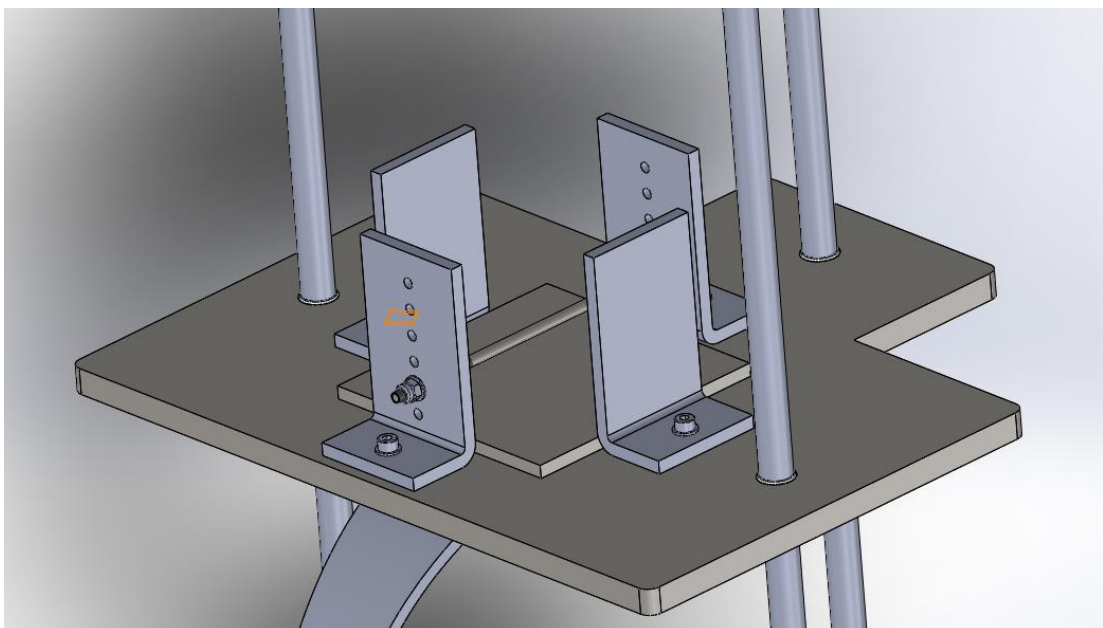
Figure 140 - Detail of the weight's support

The support for the weights is adaptable to the shape and size of them and their vertical movement relative to the base support is blocked by a steel pin that is screwed at the end and can be tied in many different heights.

Test base FEM simulation

The FEM simulation main objective was to test the screws that secured the skids and also the 3 pins that secured all the movable structure when static and with the weights on it. CBush was used to simulate the conection of the skids and bushes to the weight plataform. To simulate screws that connected the weight platform to the skids, CBars were used. The vertical force was applied at the center of the platform - that was modeled with the midsurface feature with a certain thickness – PSHELL.

The three vertical round rails were CBars as also the 3 safe pins. The representation of the FEM model can be checked in Figure 141.
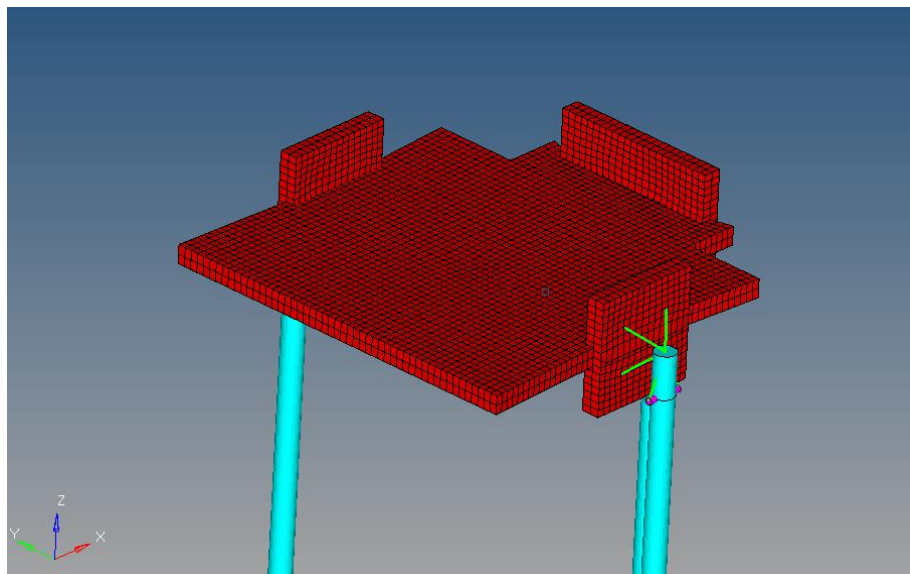
Figure 141 - Test Bed display in Hypermesh® Software

The connection between the skid and the platform is shown in Figure 142 with more detail:
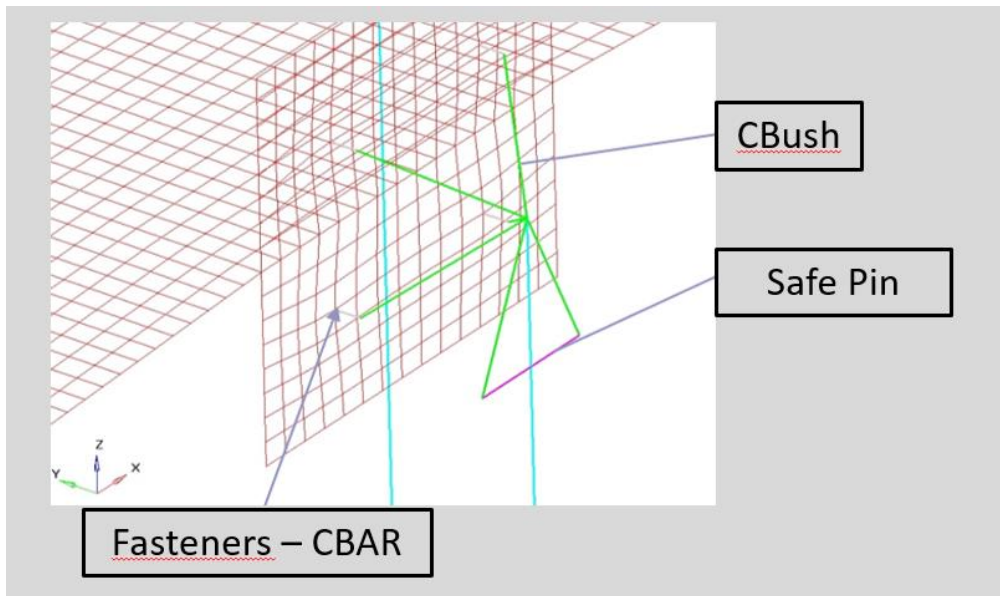
Figure 142 - Details of the connection between the rail, the skid and the platform

The safe pin is supported by the CBUSH at the 2 ends of it in order to do a conservative calculation.

Fasteners that connect the skid and the platform are represented by the CBars

Pbush properties that were used are represented in Table 39.

Table 39 - Pbush properties

PBUSH_ID	1	2	3	4	5	6
101	1.00E+10	1.00E+10	1.00E+10	1.00E+10	1.00E+10	0.00E+00
102	1.00E+10	1.00E+10	0	1.00E+10	1.00E+10	1.00E+10

Where:

- 1, 2, 3 are rigidity related to displacements along axis: X, Y and Z
- 4, 5, 6 are rigidity related to rotations around the axis X, Y and Z

Material properties can be checked in Table 40. Steel was used for the metallic simulated parts.

Table 40 – Material properties

MAT_ID	E (Gpa)	ν
MAT1	220	0.3

Properties of CBARs – PBARL – are represented in Table 41 and can be observed in Figure 143.

Table 41 – PBARL properties

Properties	Type	MAT_ID	dim (mm)
PBARL26	ROD	1	6
PBARL27	ROD	1	2
PBARL28	ROD	1	2
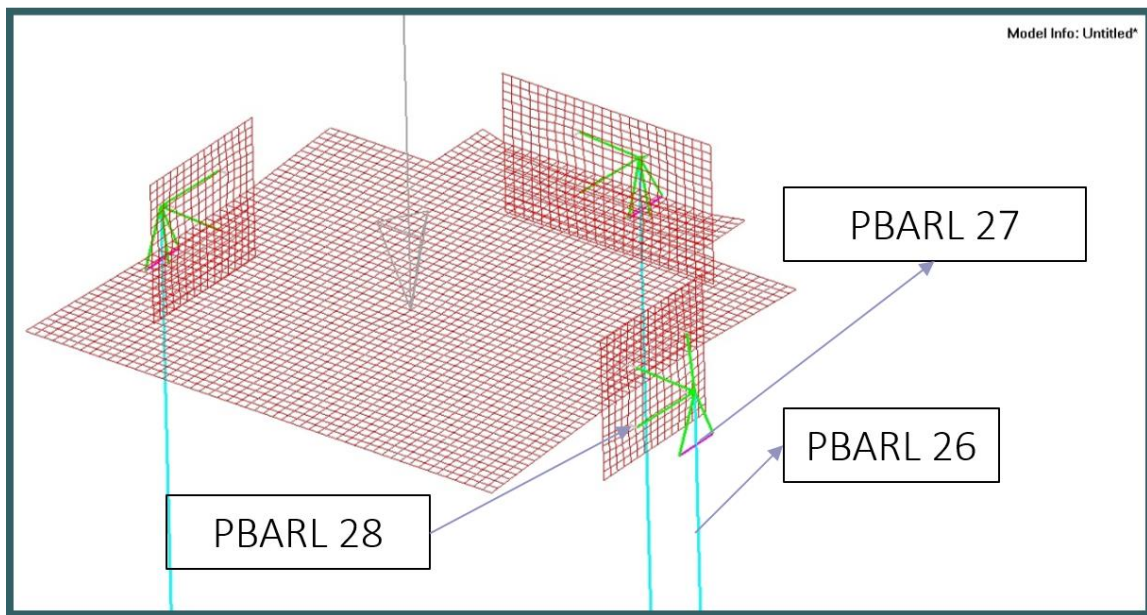
Figure 143 – PBARL identifications

PSHELL

PSHELL property was assigned to the test-bed base and can be checked in Figure 144.

Table 42 – PSHELL property of the test base

Properties	MAT_ID	dim (mm)
Pshell 1	1	10
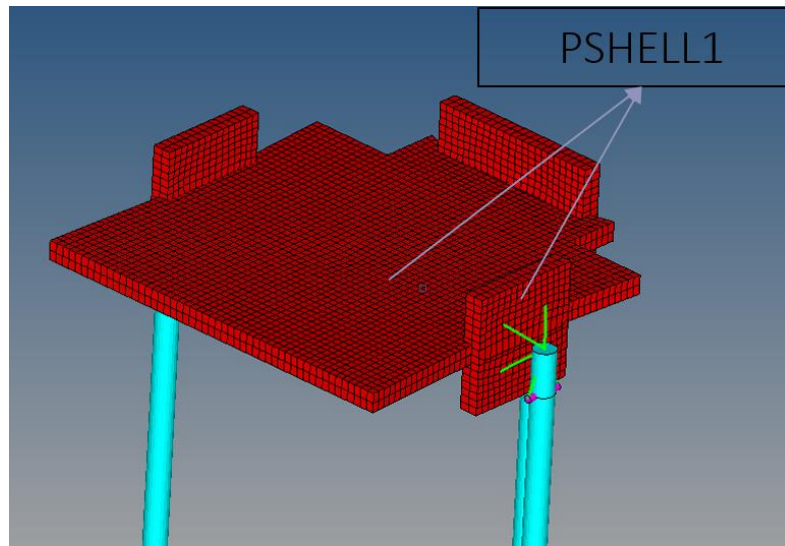
Figure 144 – PSHELL property assigned to test bed base

Force

The tested force was 200 N. The reason to use a higher value is based in the fact that this test bed can be used for other landing gear tests.

Boundary conditions

Fixed conditions were introduced at the lower extreme of the three principal rails as can be checked in Figure 145.
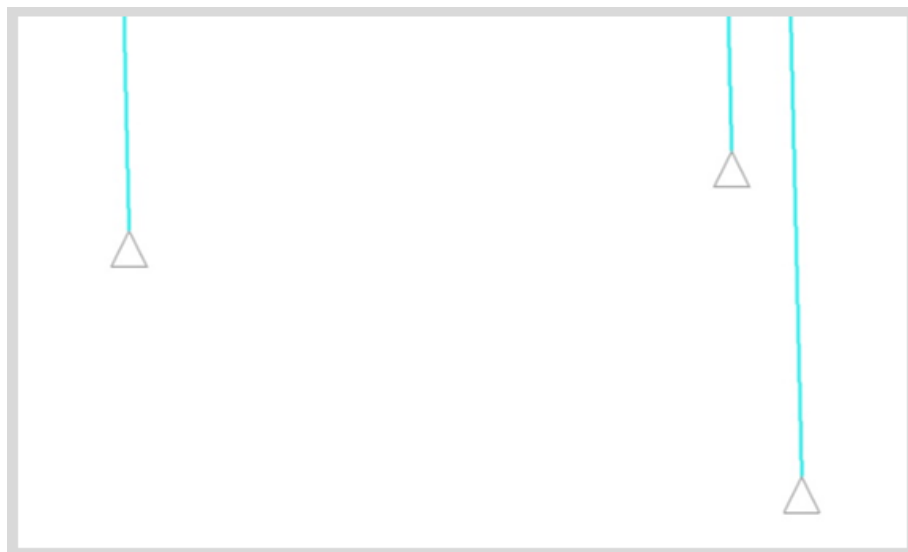
Figure 145 – Fixed conditions on vertical rails

The results of the simulations can be seen in the next figures:

Stress – Von Mises – All the parts were metallic.
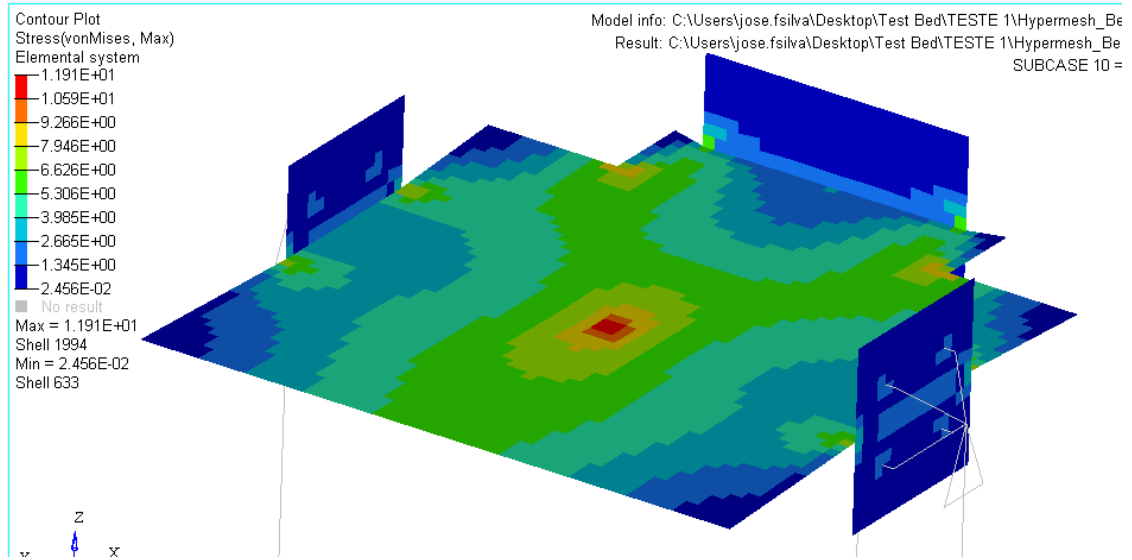
Figure 146 - Von Mises stress – metallic parts - Hypermesh® Software

1D Stress – CBAR SA1
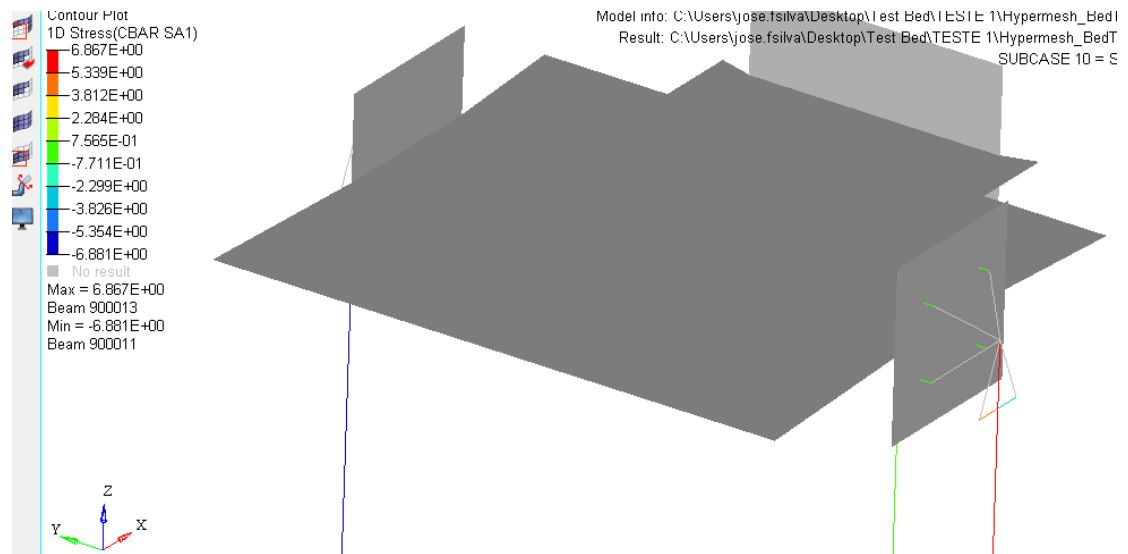
Figure 147 - 1D Stress represented on CBars - Hypermesh® Software

1D Stress – CBAR SA2
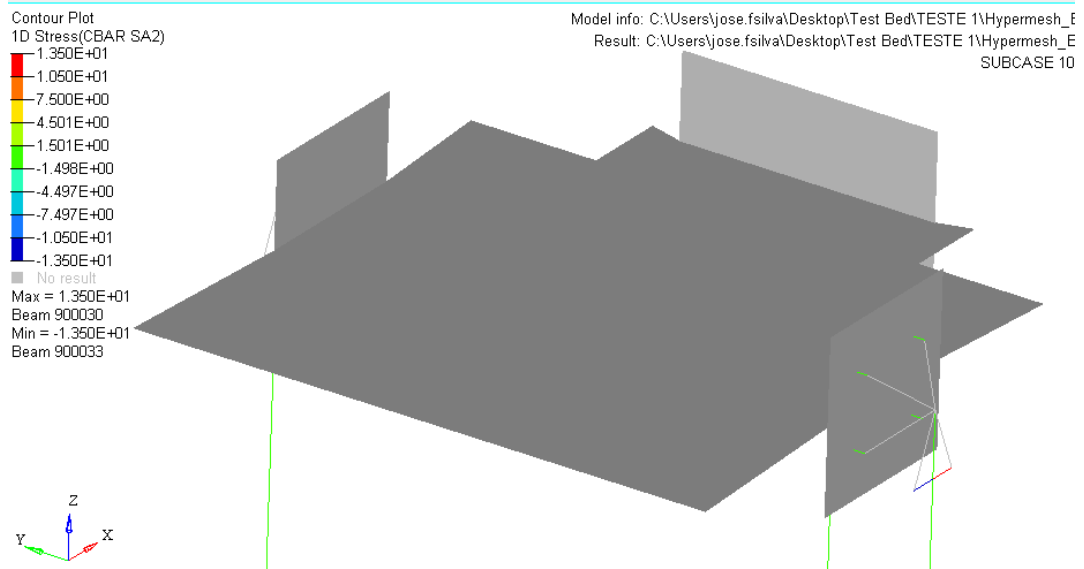
Figure 148 - 1D Stress represented on CBars - Hypermesh® Software

1D Stress – CBAR SA3
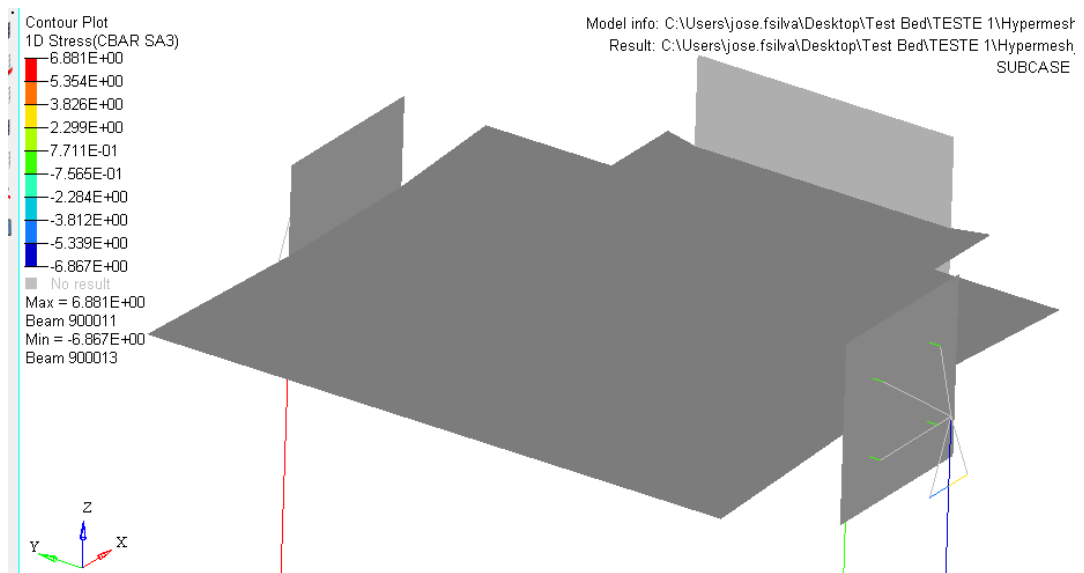
Figure 149 - 1D Stress represented on CBars - Hypermesh® Software

1D Stress – CBAR SA4
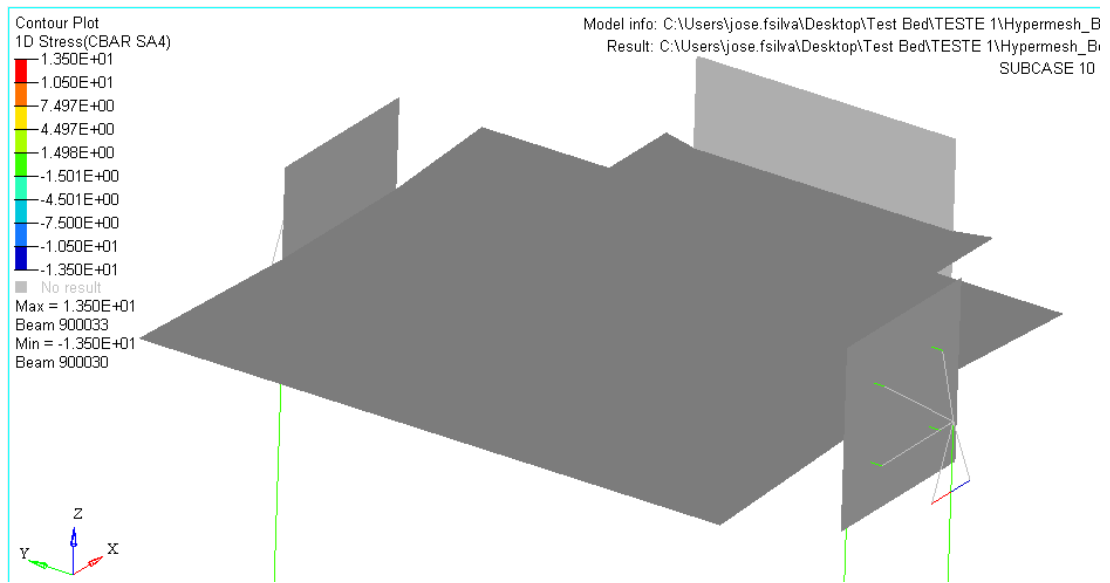
Figure 150 - 1D Stress represented on CBars - Hypermesh® Software

The results can be summed up in the Table 43:

The stress values were low and all the structure was validated.

Table 43 - Stress Maximum absolute results for test-bed [MPa]

	Types of stress					
	Von Mises [MPa]	1D -SA1 [MPa]	1D -SA2 [MPa]	1D -SA3 [MPa]	1D -SA4 [MPa]	Element Forces [N]
Vertical Rail	0	6.88	1.13	6.88	13.5	231
Safety Pin	0	4.33	13.5	4.95	13.5	18.0
Screws	0	0	0	0	0	72.5
Platform	11.9	0	0	0	0	0

7. Conclusions / Future Works

With this master thesis, all the steps of developing a nose landing gear were taken. Studying the state of the art of the landing gears, studying the actual legislation and also composites manufacturing.

A deep analysis was done when referring to the landing gear itself, since studying the involved loads, studying theoretical and analytic models of curved beams, theory of composite materials and even the tests that are typically performed on nose landing gears.

It was also needed to consider the landing gear requirements imposed by CEiiA and the actual legislation. The next step was the conceptual design where a landing gear configuration was chosen and then was decided the geometry parameters and composite stacking sequence. For this part a MATLAB software code was developed in order to save time and calculations, providing a faster approach to the first values of geometry and stack parameters. This software started with the initial goal of increasing the speed process of selecting geometric properties of isotropic curved beams. However it ended as software that also performs calculations for orthotropic materials (PREPREGs).

After this software being developed it was needed to test it. The tests consisted in using different shapes of curved beams subjected to a certain load case and comparing the obtained results by the MATLAB software code and FEM software.

Later it was needed to start the detailed design. Landing gear parts (composite and metallic) were developed using Solidworks® and CATIA® software and typical design rules were considered. After this it was needed to model the landing gear in a finite element method - FEM - software - HyperMesh® in order to validate the design.

For the test part it was considered the actual legislation. It was needed to calculate loads involved in the test. Then it was needed to design a jig-test. After this it was also required to validate this design in a finite element method - FEM - model.

However, in order to actually finish the project, it would be necessary to produce the nose landing gear, the test-base and then test the landing gear. After testing, it would be interesting to co-relate the results with the FEM predictions and close the cycle if the result of the test was satisfactory.

If the result of the test was not satisfactory, it would be essential to find what would had led to the failure (because it could be a simple calculation error, a manufacture defect, for example).

It was also possible to conclude that a leaf spring composite landing gear it's more appropriate than a rigid composite strut landing gear in small scale UAVs and also that prepreg carbon fiber would be the suitable material for a small production of nose landing gears.

A continuous airworthiness maintenance program was also created in order to ensure that the working life of these landing gears would not be compromised.

It would also be interesting to develop a test-base for fatigue testing so that is possible to predict the service life cycle of the setup and find existing fatigue problems. Another interesting future work would be studying crack propagation in landing gears.

If possible it would also be very important to perform campaign tests for the used materials following aviation industry standards with the intention of obtaining certification of the landing gear.

8. References

9. Referências

© Altair Engineering, Inc. *Pratical Aspects of Finite Element Simulation - A student Guide.* Michigan, 2011.

2012. http://aviationglossary.com/principal-structural-elements-pse/.

Active Structures Laboratory. "Active Structures Laboratory." 2005. http://scmero.ulb.ac.be/Teaching/Courses/MECA-H-406/H-406-5-LaminatedComposites.pdf (acedido em 07 de February de 2017).

Administration, Federal Aviation. "FAR - Federal Aviation Regulations." EUA, 1967.

Aero, Aerotrek. *Aerotrek Aero.* 2010. http://www.aerotrek.aero/photos/spats/593m.jpg (acedido em 07 de February de 2017).

Aircraft, Golden Skies R/C. *Golden Skies R/C Aircraft.* s.d. http://www.goldenskiesrc.com/SLG.html (acedido em 02 de February de 2017).

Airliners. *Airliners photos.* 2000. http://www.airliners.net/photos/airliners/3/6/9/2395963.jpg (acedido em 07 de February de 2017).

Altair. "2006." *Altair Univesity.* s.d. http://www.altairuniversity.com/wp-content/uploads/2012/04/1D_Elements_Extract.pdf (acedido em 15 de February de 2017).

Barrett, Richard T. *Fastener Design Manual.* Lewis Research Center, Cleveland, Ohio , EUA: NASA Reference Publication, 1990.

BB composite. *BB composite.* 2005. http://bbcomposite.com/tags/pegaz (acedido em 02 de February de 2017).

BURGUN, ROBERT SCOTT,. "The Design, Analysis, Construction and Testing of an Uninhabited Aero Vehicle Platform." 2003.

CEiiA. *CEiiA.* 2015. https://www.ceiia.com/aero-uas30 (acedido em 07 de February de 2017).

Club, Algoa Flying. *Algoa Flying Club.* 2011. http://www.algoafc.co.za/wp-content/uploads/2013/06/C152_1.jpg (acedido em 2 de February de 2017).

Company, Wright Brothers Aeroplane. *Wright Brothers Aeroplane Company.* s.d. http://www.wright-brothers.org/Information_Desk/Just_the_Facts/Airplanes/Wright_Airplane_images/Model_AB/1910_Model_AB_launch.jpg (acedido em 2 de February de 2017).

Composites, Cured. *Cured Composites.* s.d. http://curedcomposites.com/images/lg1.JPG (acedido em 2 de February de 2017).

Composites, Net. 03 de January de 2017. http://netcomposites.com/guide-tools/guide/repair/vacuum-bagging/ (acedido em 2 de February de 2017).

Currey, Norman S. *Aircraft Landing Gear Design: Principles and Practices* . Washington, USA: AIAA EDUCATION SERIES , 1988.

Dassault Systemes. *Help Solidworks.* 2007. http://help.solidworks.com/2015/English/SolidWorks/cworks/r_TsaiWu_Failure_Criterion.htm (acedido em 02 de February de 2017).

Defense, Us Dept Of. *Composite Materials Handbook-MIL 17 - volume 3.* USA: TECHNOMIC, 2001.

Division on Engineering and Physical Sciences; National Materials Advisory Board. *Accelerated Aging of Materials and Structures: The Effects of Long-Term Elevated-Temperature Exposure.* EUA: Engineering and Technology, 1996.

EASA. *CS-VLA.* 2009.

Elimco. *Elimco.* 2015. http://elimco.com/eng/c_Unmanned-Aircraft-Vehicles-UAV-_10.html (acedido em 7 de February de 2017).

Engineer on a disk. *Engineer on a disk.* 2008. http://engineeronadisk.com/notes_mechanic/axiala3.html (acedido em 7 de February de 2017).

FAA . *CHAPTER 9. Aircraft systems and components - SECTION 1. Inspection and Maintenance of landing gear.* Advisory Circular, EUA: FAA, 2001.

FAA - Federal Aviation Administration. *Handbook Manual, Aircraft – Chapter 13.* s.d. https://www.faa.gov/regulations_policies/handbooks_manuals/aircraft/amt_airframe_handbook/media/ama_Ch13.pdf (acedido em 7 de February de 2017).

Failure of laminates and the Tsai–Hill criterion. 2004. https://www.doitpoms.ac.uk/tlplib/fibre_composites/laminate_failure.php (acedido em 7 de February de 2017).

Fast Aviation Data. *Fast Aviation Data.* s.d. https://www.fastaviationdata.com/wp-content/uploads/PN/PN001/PNFiles/aai-rq-7-shadow.jpg (acedido em 2 de February de 2017).

"FE-modeling of bolted joints in structures ." Master Thesis, Sweden, 2012.

Fiber Dynamics, Inc. *Projects of Fiber Dynamics.* s.d. http://www.fiberdynamics.net/images/predator_b_mq_9_reaper_close_up_big.jpg (acedido em 7 de February de 2017).

Flite, Freedom. *Freedom Flite Landing gears.* s.d. http://www.ultralightassembly.com/back40.htm (acedido em 7 de February de 2017).

Flugzeugbau, Remos Aircraft GmbH. *My-Remos.* 2016. http://www.my-remos.de/ (acedido em 7 de February de 2017).

FPV Mmodel. *FPV Mmodel.* 2015. http://www.fpvmodel.com/new-mugin-plus-4500mm-plane_g962.html (acedido em 7 de February de 2017).

Gear, Fults Landing. *Fults Landing Gear.* 2001-2015. http://www.fultslandinggear.com/Scorpionseries.html (acedido em 7 de February de 2017).

Giant, Sierra. *Sierra Giant landing gears.* 2008. http://www.sierragiant.com/prod19.html (acedido em 7 de February de 2017).

Gramoll, Kurt. *Ecourses.* 2012. http://www.ecourses.ou.edu/cgi-bin/eBook.cgi?topic=me&chap_sec=01.2&page=theory (acedido em 7 de February de 2017).

Gudmundsson, Snorri. *General Aviation Aircraft Design; Applied methods and procedures.* Elsevier Inc., 2014.

Hagen, Brad. *P40 Warhawk.* 2002. http://www.p40warhawk.com/Models/Reviews/Models/Scratchbuilders/P-40B-C/P40gears.jpg (acedido em 2 de February de 2017).

Hart, Mike. *Stressebook.* s.d. http://www.stressebook.com/wp-content/uploads/2015/01/RBE2-Vs-RBE3-600x263.png (acedido em 07 de February de 2017).

Hexion. *Hexion.* s.d. www.hexion.com/uploadedImages/Micro_Sites/EpoxyPhenolicComposites/Automotive/Your_Process/Prepreg_Illustration_V5.jpg (acedido em 7 de February de 2017).

HTT, Maya. "Siemens PLM Community." *Siemens PLM Community.* October de 2016. https://community.plm.automation.siemens.com/t5/Fibersim-Forum/Failure-Index-vs-Strength-Ratio-in-a-Quadratic-Failure-Criterion/td-p/372808 (acedido em 2 de February de 2017).

J.N.Reddy. *An Introduction to the finite element method - 3rd edition.* Texas, Usa: Mc Graw Hill, 2006.

Jollivet, Thomas, Catherine Peyrac, e Fabien Lefebvre. "Damage of composite materials ." *ScienceDirect*, 2013.

Kim, Prof. Olivier de Weck and Dr. Il Yong. "MIT - Massachusetts Institute of Technology." January de 2004. http://web.mit.edu/16.810/www/16.810_L4_CAE.pdf (acedido em 7 de February de 2017).

Kumar, Ashwini. *Stability of structures.* Allied publishers limited, 1998.

"Fiber-Reinforced Composites: Materials, Manufacturing, and Design." Em *Fiber-Reinforced Composites: Materials, Manufacturing, and Design*, de P.K. Mallick, 554. EUA, New York: Marcel Dekker, 1993.

Media Defense. *Media Defense.* 2012. http://media.defense.gov/2012/Jul/31/2000129312/-1/-1/0/120730-F-AP630-087.JPG (acedido em 7 de February de 2017).

Montana State University. *Design Allowables.* 2007. http://www.montana.edu/dcairns/documents/introduction_to_aerospace-web/12-DesignAllowables.pdf (acedido em 07 de February de 2017).

MSC Software. *MSC Nastran 2013 - Quick Reference guide.* MSC Software, 2013.

Nano Motion. *Nano Motion.* s.d. http://www.nanomotion.com/piezo-ceramic-motor-technology/piezoelectric-effect/ (acedido em 07 de February de 2017).

NATO. "STANAG 4703 - LIGHT UNMANNED AIRCRAFT SYSTEMS AIRWORTHINESS REQUIREMENTS." 2014.

Net Composites. *Net Composites Ldt.* s.d. http://netcomposites.com/guide-tools/guide/repair/vacuum-bagging (acedido em 7 de February de 2017).

Network 54. *Network 54.* 2010. http://www.network54.com/Forum/242894/thread/1279326539/last-1280428304/TAI+Anka+MALE+UAV (acedido em 7 de February de 2017).

Ni, Michael C. *Composite Airframe Structures.* Hong Kong: Conmilit Press, 1992.

Pikey, W.D. "Peterson's stress concentration factors." 1997.

Pilot Planes. *Pilot Planes.* s.d. http://www.pilot-planes.com/images/roughrivervarieze.jpg (acedido em 7 de February de 2017).

Plymouth University. *Composite Strength and Failure Criteria - Power Point.* United Kingdom, 2009.

Reddy, J. N . *An Introduction to the Finite Element Method - 2nd edition.* USA: MC Graw Hill, 1993.

Reddy, J.N. *Mechanics of laminated composite plates and shells .* CRC Press, 2004.

S.Timoshenko. *Strength of Materials - Vol II.* D.Van Nostrand Company, 1940.

Sadraey, Mohammad. Em *Aircraft Design: A Systems Engineering Approach*, de Mohammad Sadraey. Nashua, New Hampshire, United States: Daniel Webster College, 2012.

Satuma. *Satuma - UAVs.* s.d. http://satuma.org/product/flamingo/ (acedido em 7 de February de 2017).

SeStrucutres. *SeStrucutres.* 17 de October de 2016. https://www.sestructures.com/foundations/17-public-site/foundations/foundations-finite-element/38-foundations-rbe2-vs-rbe3 (acedido em 7 de February de 2017).

Tadashi Horibe, Kotaro Mori. "In-Plane and Out-of-Plane Deflection of J-Shaped Beam." *Journal of Mechanical Engineering and Automation*, 2015.

The Aviation History Online Museum. *The Aviation History Online Museum.* 2016. http://www.aviation-history.com/sopwith/camel.htm (acedido em 07 de February de 2017).

Thompson, Robert Ian. United Kingdom Patente US8640988 B2. 2014.

Thota, Dr. Jagadeep. *Energy & Variational Methods in Mechanics I.* University of Nevada Las Vegas, 2009.

tool, Quality. *Quality tool.* 2014. http://www.qualitytool.com/resources/Design-Handbook-Rev3.pdf (acedido em 7 de February de 2017).

UAV Factory. *UAV Factory.* s.d. http://www.uavfactory.com/product/46 (acedido em 7 de February de 2017).

UNIVERSAL ANALYTICS, INC. *UAI/NASTRAN User's Guide .* California, USA: UNIVERSAL ANALYTICS, INC., 1999.

University of Cambridge. *University of Cambridge.* s.d. https://www.doitpoms.ac.uk/tlplib/fibre_composites/laminate_failure.php (acedido em 7 de February de 2017).

University of Washington. 17 de Outubro de 2016. http://courses.washington.edu/me354a/Energy%20methods.pdf (acedido em 7 de February de 2017).

Wade. *Long Ez Push.* s.d. http://www.longezpush.com/chapter-13-nose-nose-gear/ (acedido em 7 de February de 2017).

Westman, Auron L. EUA Patente US 8,317,130 B1 . 2012.

Yari, Mehdi. *CorrosionPedia.* 2012. https://www.corrosionpedia.com/2/1556/corrosion/galvanic-corrosion-of-metals-connected-to-carbon-fiber-reinforced-polymers (acedido em 7 de February de 2017).

Ye, J. Lam, D. and Zhang, D. *Initiation and Propagation of Transverese Cracking in Composite Laminates.* Paper, Leeds, U.K.: Computational Materials Science, 2010.

Zafer Gürdal, Raphael T. Haftka,Prabhat Hajela. "Design and Optimization of Laminated Composite Materials." Em *Design and Optimization of Laminated Composite Materials*, de Raphael T. Haftka,Prabhat Hajela Zafer Gürdal, 245. Florida, USA: Wiley - Interscience Publication, 1999.

Annex A - MATLAB® Software codes

For deflection and stress calculation:

For confidentiality reasons MATLAB codes cannot be displayed.

Development of a nose landing gear of an unmanned aircraft (RPAS)

Annex B: Detailed Designs
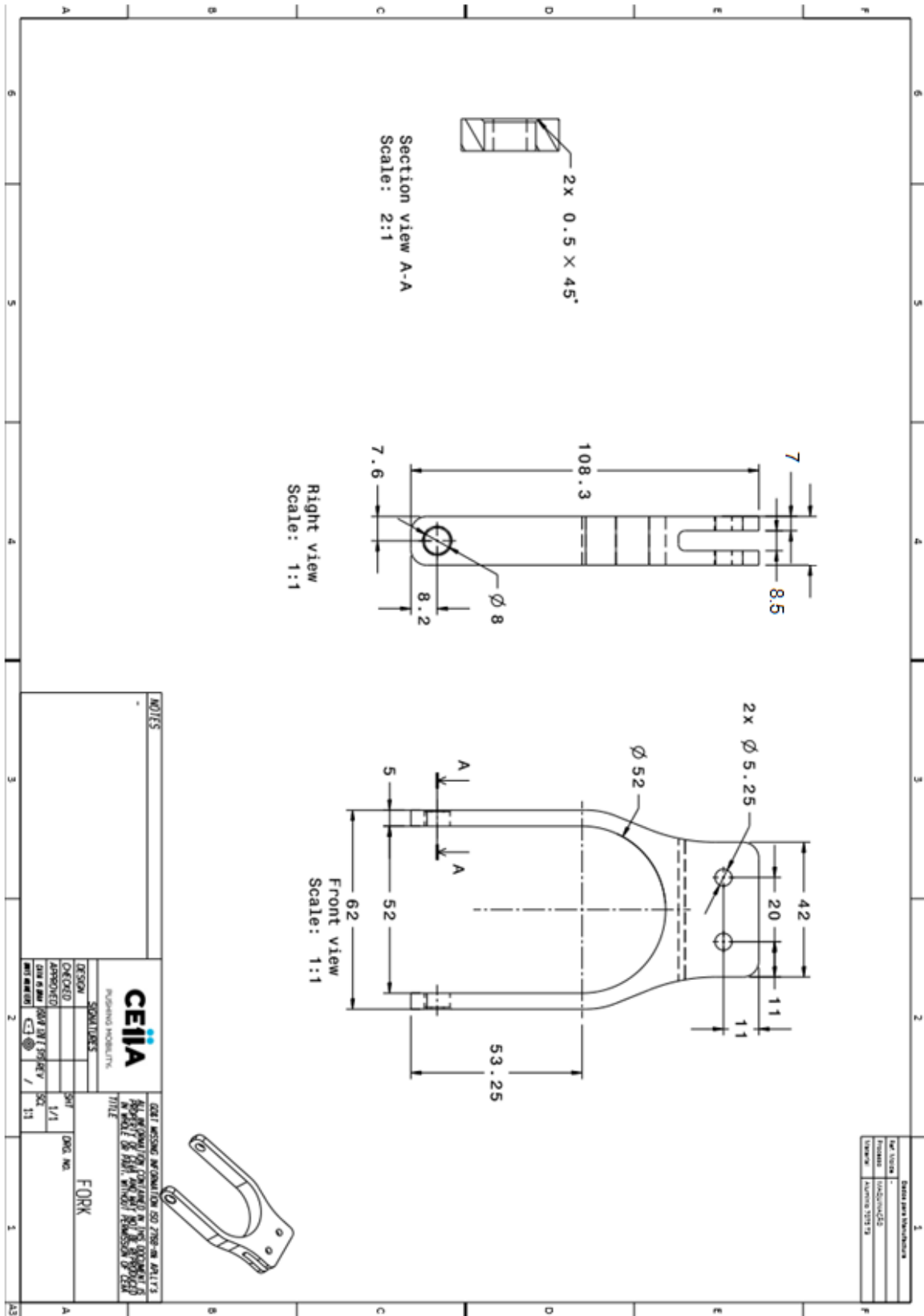
Figure 151 – Detailed design: Fork

175
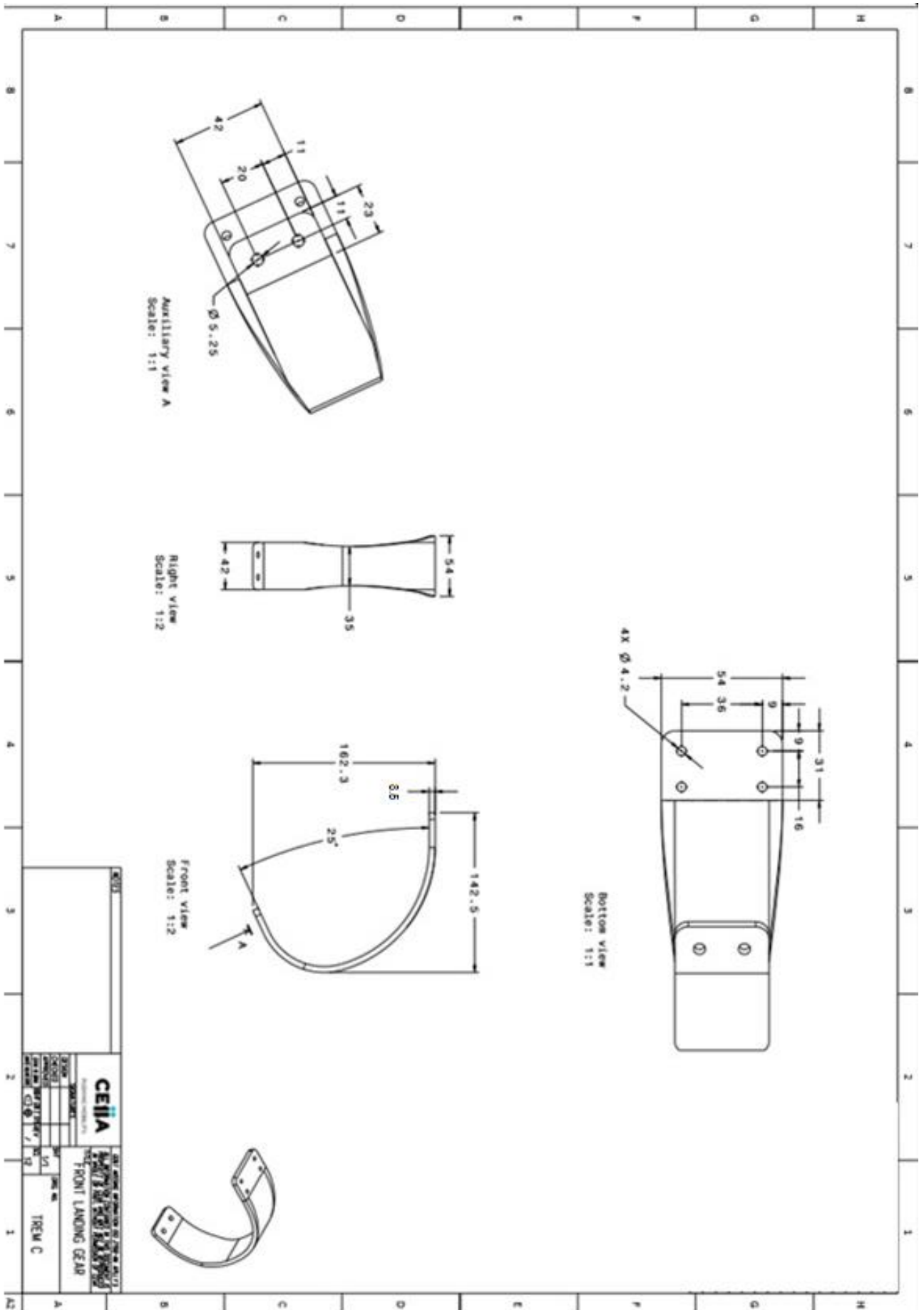
Figure 152 – Detailed design – Landing gear composite leaf
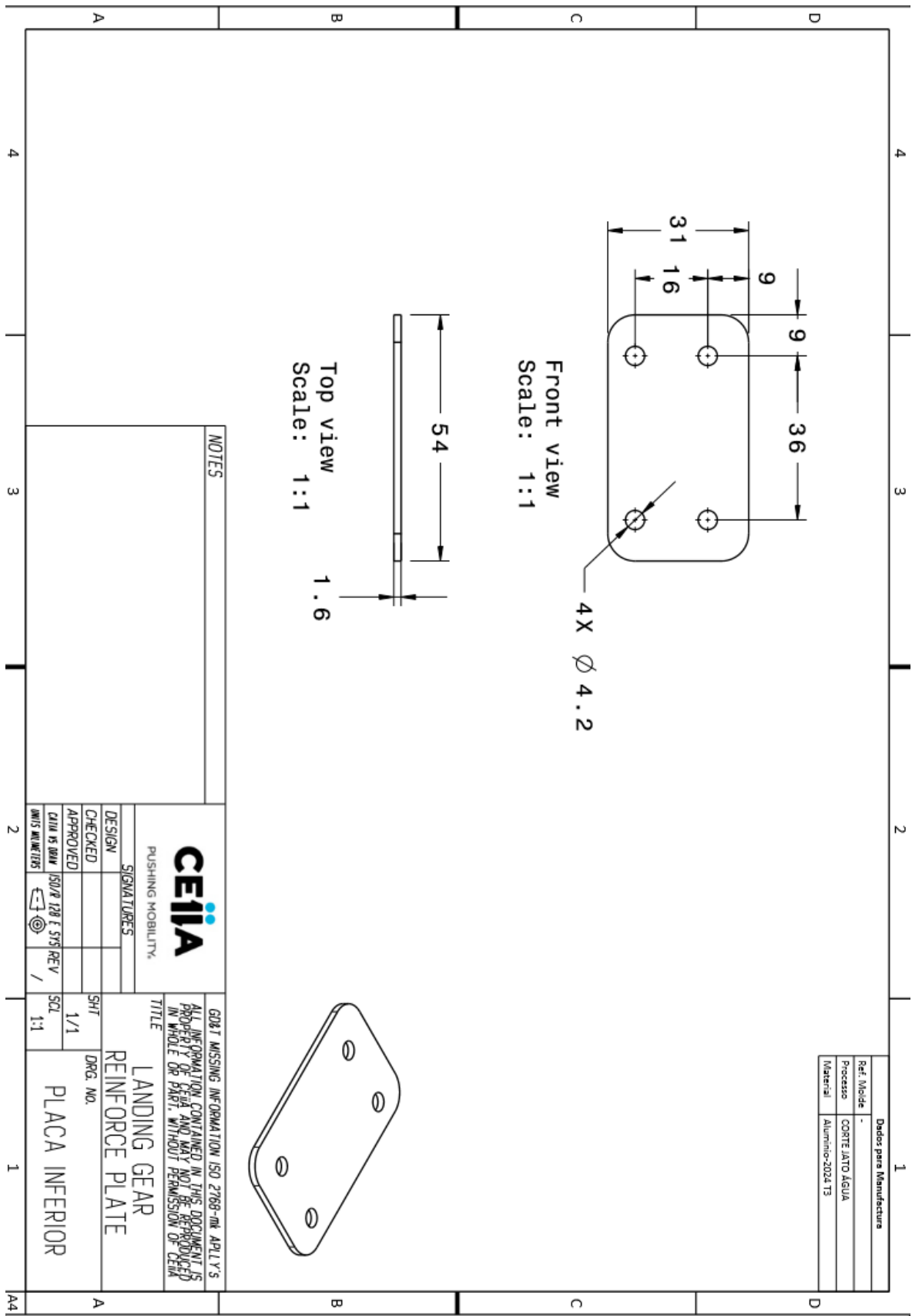
Figure 153 – Detailed design - Down Plan plate
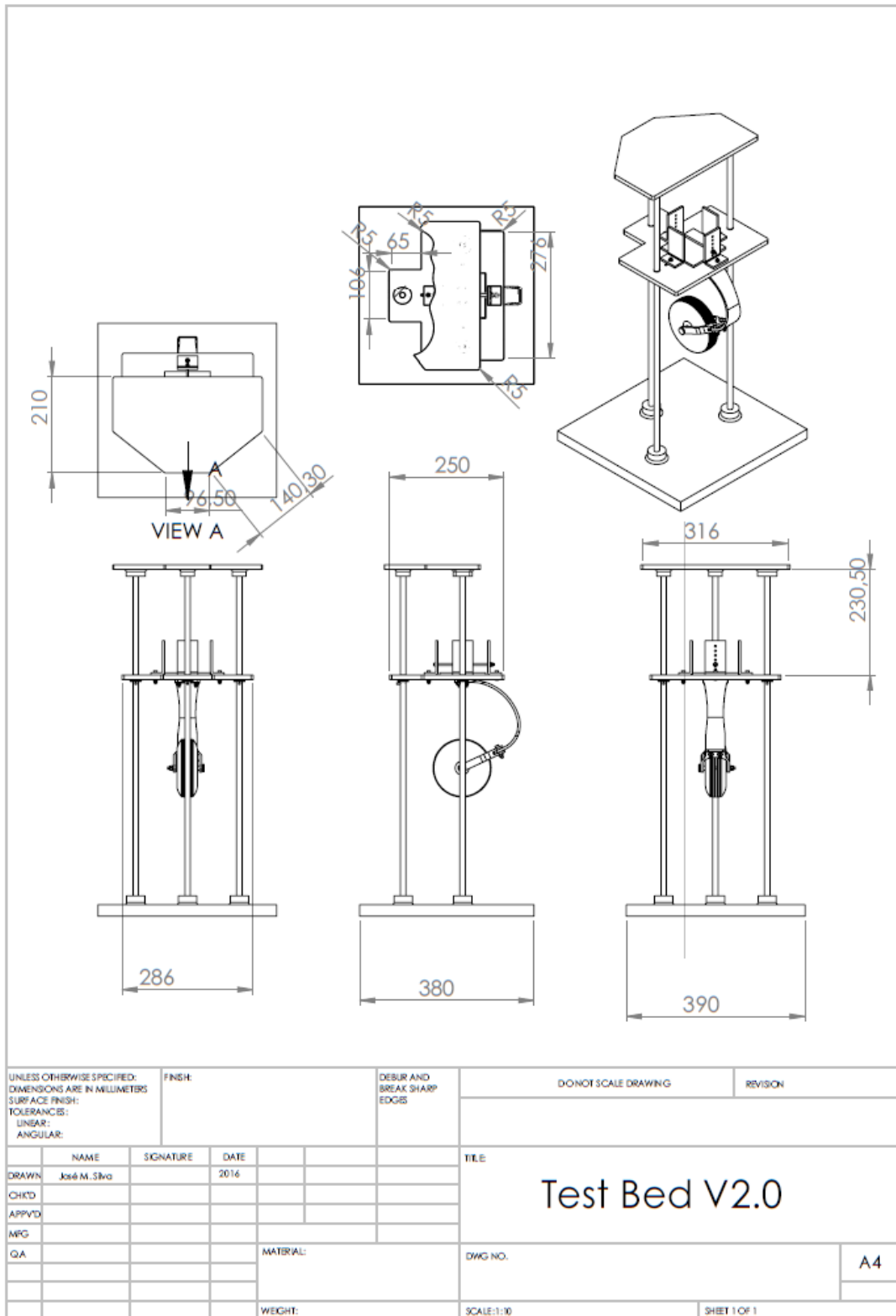
Figure 154 - 2D Design of the Test Bed

Annex C: Calculations

Table 44 – List of Parts of the Test Base

Designation	Part Number	Quantity	Material	Link
Superior Base	1	1	Steel - Ck45	
Inferior base	2	1	Steel - Ck45	
Moving Base	3	1	Steel - Ck45	
M4 Nut	5	9	Zinc plated steel	https://www.fabory.com/pt/fixacao/porcas-de-rebitar-insertos/porcas-porcas-de-rebitar-insertos/porca-auto-bloqueante-sextavada-com-inserto-nao-metalico-din-985-1987-aco-zincado-5-m4/p/1230004001
M4 Circular Plate	7	8	Zinc plated steel	https://www.fabory.com/en/fasteners/washers-o-rings/plain-washer-without-chamfer-flat-punched-din-125-1a-steel-140hv-zinc-plated-m4/p/38031040001
M4 Screws	8	8	Stainless Steel	https://www.fabory.com/en-FR/fasteners/hexagon-socket-products/hexagon-socket-head-cap-screw-din-912-stainless-steel-a4-70-m4x22/p/55050040022
Plastic Bushing	9	3	Nylon	https://www.fabory.com/en-FR/fasteners/engineering-parts-machine-parts/insulating-bush-plastic-polyamide-nylon-pa-6-6-m12/p/567601200001
Vertical Rail - 752 x diam12mm	10	3	Steel - Ck45	
Drop-pin - 20xdiam 4 mm	11	3	Steel - Ck45	
Weight lateral suport	12	2	Al2024	
Weight lateral suport with holes	13	2	Al2024	
Weight pin 128 x 4mm diam	14	1	Steel - Ck45	

Table 45 – Bearing Stress Results

Identification	CBAR ID	Shear 1 (N)	Shear 2 (N)	Tension (N)	Total Shear (N)	Diam. (mm)	Thick. (mm)	Double Shear (N)	σbearing (Mpa)	σbearing* 1.5 (Mpa)	BringAllwb (Mpa)	Material	Safety Margin
Fork 1 - axle	30	111.2	-412.0	-10.2	426.8	5.0	7.0		12.2	18.3	662.0	Al7075	35.2
Fork 2 - axle	31	-110.8	410.0	-10.2	424.7	5.0	7.0		12.1	18.2	662.0	Al7075	35.4
SC9 -Fork.UP	9	2691.1	-581.5	257.1	2753.2	6.0	7.0	207.8	4.9	7.4	662.0	Al7075	88.2
SC9 - Composite	9	2691.1	-581.5	257.1	2753.2	6.0	5.7	207.8	6.1	9.1	404.9	Prepreg	43.6
SC12-Fork.UP	12	-2752.3	586.3	199.8	2814.1	6.0	7.0	207.8	4.9	7.4	662.0	Al7075	88.2
SC12 - Composite	12	-2752.3	586.3	199.8	2814.1	6.0	5.7	207.8	6.1	9.1	404.9	Prepreg	43.6
SC12-Fork.UP	12	-2752.3	586.3	199.8	2814.1	6.0	7.0	207.8	9.9	14.8	662.0	Al7075	43.6
SC10-Fork.UP	10	2618.0	-278.5	-215.9	2632.8	6.0	7.0	207.8	4.9	7.4	662.0	Al7075	88.2
SC10-Composite	10	2618.0	-278.5	-215.9	2632.8	6.0	5.7	207.8	6.1	9.1	404.9	Prepreg	43.6
SC11-Fork.UP	11	-2679.2	283.4	-165.4	2694.2	6.0	7.0	207.8	4.9	7.4	662.0	Al7075	88.2
SC11 - Composite	11	-2679.2	283.4	-165.4	2694.2	6.0	5.7	207.8	6.1	9.1	404.9	Prepreg	43.6
SC1 - maquinado.Down	1	312.7	-337.4	-1347.2	460.0	4.0	5.0	105.3	4.2	6.3	524.0	Al2024	82.8
SC1 - Composite	1	-188.3	-92.0	932.1	209.6	4.0	5.0	105.3	7.5	11.3	662.0	Al7075	57.7
SC2 - composite	2	-211.0	-248.7	24.0	326.1	4.0	5.7	105.3	4.6	6.9	404.9	Prepreg	57.7
SC2 - downPlate	2	-211.0	-248.7	24.0	326.1	4.0	1.6	105.3	12.7	19.1	404.9	Prepreg	20.2
SC3 - composite	3	217.7	-166.5	-23.7	274.1	4.0	5.7	130.2	7.4	11.1	524.0	Al2024	46.4
SC3 - downPlate	3	217.7	-166.5	-23.7	274.1	4.0	1.6	130.2	15.7	23.5	404.9	Prepreg	16.2
SC4 - machnd_piece_Down	4	312.7	-337.4	-1347.2	460.0	4.0	5.0	130.2	7.4	11.1	524.0	Al2024	46.4
SC4 - Composite	4	312.7	-337.4	-1347.2	460.0	4.0	5.7	130.2	6.5	9.8	662.0	Al7075	66.8
SC11 - Composite	11	-2679.2	283.4	-165.4	2694.2	6.0	5.7	207.8	6.1	9.1	404.9	Prepreg	43.6
SC5-machnd_piece_Down	5	-216.4	61.9	970.1	225.1	4.0	1.6	114.6	5.7	8.6	662.0	Al7075	76.0
SC5 - Composite	5	-216.4	61.9	970.1	225.1	4.0	5.7	114.6	5.0	7.5	404.9	Prepreg	52.9
SC6 - composite	6	-232.3	233.5	23.5	329.3	4.0	5.7	114.6	5.0	7.5	404.9	Prepreg	52.9
SC6 - downPlate	6	-232.3	233.5	23.5	329.3	4.0	1.6	114.6	13.9	20.8	404.9	Prepreg	18.5
SC8 - machnd_piece_Down	8	314.0	367.5	-1377.0	483.4	4.0	5.0	137.1	6.9	10.3	662.0	Al7075	63.4
SC8 - Composite	8	314.0	367.5	-1377.0	483.4	4.0	5.7	137.1	6.0	9.0	404.9	Prepreg	44.1
SC7 - composite	7	225.5	181.7	-24.0	289.6	4.0	5.7	137.1	6.0	9.0	404.9	Prepreg	44.1
SC7 - downPlate	7	225.5	181.7	-24.0	289.6	4.0	1.6	137.1	16.5	24.8	404.9	Prepreg	15.3
SC27 - machined.Cil	27	-1544.1	-227.7	5.3	1560.8	6.0	4.0	65.0	65.0	97.5	662.0	Al7075	5.8
SC27 - Pino Principal	27	-1544.1	-227.7	5.3	1560.8	6.0	14.0	18.6	18.6	27.9	400.0	Ck45	13.4
SC28- Pino Principal	28	1561.7	229.5	10.5	1578.5	6.0	14.0	18.8	18.8	28.2	400.0	Ck45	13.2
SC28 - machined.Cil	28	1561.7	229.5	10.5	1578.5	6.0	4.0	65.8	65.8	98.7	662.0	Al7075	5.7
SC9095-machined.Cil	9095	1443.8	-204.3	-48.7	1458.2	6.0	4.0	60.8	60.8	91.2	662.0	Al7075	6.3
SC9095- Main Pin	9095	1443.8	-204.3	-48.7	1458.2	6.0	14.0	17.4	17.4	26.0	400.0	Ck45	14.4
SC9096- Main Pin	9096	-1440.0	160.5	-53.6	1448.9	6.0	14.0	17.2	17.2	25.9	400.0	Ck45	14.5
SC9096-machined.Cil	9096	-1440.0	160.5	-53.6	1448.9	6.0	4.0	60.4	60.4	90.6	662.0	Al7075	6.3
SC9094 - horizontal_ Ear	9094	-221.2	3.8	-822.2	221.2	14.0	5.0		3.2	4.7	524.0	Al2024	109.6
SC26- horizontal_Ear	26	413.4	-4.4	-46.6	413.4	14.0	5.0		5.9	8.9	524.0	Al2024	58.1
SC26- horizontal_ Ear	26	413.4	-4.4	-46.6	413.4	14.0	5.0		5.9	8.9	524.0	Al2024	58.1
SC - 25 - fibra UAV	25	-11.5	44.4	83.6	45.9	4.0	0.3		44.1	66.1	378.0	Sandwich Carbon	4.7
SC - 22 - fibra UAV	22	-20.3	-68.4	121.2	71.3	4.0	0.3		68.6	102.9	378.0	Sandwich Carbon	2.7
SC - 21 - fibra UAV	21	22.5	22.5	122.9	72.0	4.0	0.3		69.3	103.9	378.0	Sandwich Carbon	2.6
SC - 18 - fibra UAV	18	-13.7	85.6	45.8	86.7	4.0	0.3		83.4	125.1	378.0	Sandwich Carbon	2.0
SC - 25 - vertical_ Ear Sup	25	-11.5	44.4	83.6	45.9	4.0	2.0		5.7	8.6	524.0	Al2024	59.9
SC - 22 - vertical_Ear inf	22	-20.3	-68.4	121.2	71.3	4.0	2.0		8.9	13.4	524.0	Al2024	38.2
SC - 21 - vertical_Ear inf	21	22.5	-68.4	122.9	72.0	4.0	2.0		9.0	13.5	524.0	Al2024	37.8
SC - 18 - vertical_Ear Sup	18	-13.7	85.6	45.8	86.7	4.0	2.0		10.8	16.3	524.0	Al2024	31.2

Table 46 – GP Forces results

			GP FORCES						
POINT-ID	ELEMENT-ID	T1	T2	T3		s1	s2	Axial	Double Shear
4	9	-1.72E+02	-3.88E+02	1.79E+03					
8	9	1.72E+02	3.88E+02	-1.79E+03		2.02E+02	-4.87E+01	1.72E+02	207.8
8	10	1.44E+02	-1.86E+02	1.75E+03					
6	10	-1.44E+02	1.86E+02	-1.75E+03					
3	12	-1.33E+02	-3.91E+02	-1.83E+03					
7	12	1.33E+02	3.91E+02	1.83E+03		2.02E+02	4.87E+01	1.33E+02	207.8
7	11	1.10E+02	-1.89E+02	-1.79E+03					
5	11	-1.10E+02	1.89E+02	1.79E+03					
20	5	-6.47E+02	4.15E+01	-1.44E+02					
16	5	6.47E+02	-4.15E+01	1.44E+02		1.14E+02	-1.06E+01	6.47E+02	114.6
16	6	-1.57E+01	1.56E+02	-1.55E+02					
10	6	1.57E+01	-1.56E+02	1.55E+02					
19	8	9.18E+02	-2.09E+02	2.45E+02					
15	8	-9.18E+02	2.09E+02	-2.45E+02		5.90E+01	-1.24E+02	-9.18E+02	137.1
15	7	1.60E+01	-1.50E+02	1.21E+02					
11	7	-1.60E+01	1.50E+02	-1.21E+02					
17	1	-6.21E+02	-1.26E+02	6.16E+01					
13	1	6.21E+02	1.26E+02	-6.16E+01		-1.51E+01	1.04E+02	6.21E+02	105.3
13	2	-1.60E+01	-1.41E+02	1.66E+02					
9	2	1.60E+01	1.41E+02	-1.66E+02					
18	4	8.98E+02	-2.08E+02	-2.25E+02					
14	4	-8.98E+02	2.08E+02	2.25E+02		6.33E+01	1.14E+02	-8.98E+02	130.2
14	3	1.58E+01	-1.45E+02	-1.11E+02					
12	3	-1.58E+01	1.45E+02	1.11E+02					

Table 47 – CBAR Forces Results

CBAR FORCES										
El ID	**s1**	**s2**	**Axial**	**Shear**		**El ID**	s1	s2	Axial	Shear
9	1794.1	-387.7	171.4	1835.5		8	209.3	245.0	-918.0	322.3
10	1745.4	-185.7	-143.9	1755.2		7	150.3	121.1	-16.0	193.1
	S1'	S2'	Double Shear				S1'	S2'	Double Shear	
	48.7	-202.0	207.8				59.0	123.9	137.2	
El ID	s1	s2	Axial	Shear		**El ID**	s1	s2	Axial	Shear
11	-1786.2	188.9	-110.3	1796.1		1	-125.5	-61.3	621.4	139.7
12	-1834.9	390.9	133.2	1876.1		2	-140.6	-165.8	16.0	217.4
	S1'	S2'	Double Shear				S1'	S2'	Double Shear	
	48.7	-202.0	207.8				15.1	104.5	105.5	
El ID	s1	s2	Axial	Shear		**El ID**	s1	s2	Axial	Shear
5	-144.3	41.3	646.7	150.1		4	208.5	-224.9	-898.1	306.7
6	-154.9	155.7	15.7	219.6		3	145.1	-111.0	-15.8	182.7
	S1'	S2'	Double Shear				S1'	S2'	Double Shear	
	10.6	-114.4	114.9				63.3	-114.0	130.4	

Table 48 – Results for Shear and Tension combination

Element ID	Fastener Type	Diameter[mm]	Shear Allowable [N]	Tension Allowable [N]	Tension Load [N]	Shear Load [N]	UL.Fact.	MSbr+s
SC9-Fork.UP	DIN 912 Stainless steel A2 70 M6X30	6.0	8793	19792	257	208	1.5	24.60
SC9 - Composite	DIN 912 Stainless steel A2 70 M6X30	6.0	8793	19792	257	208	1.5	24.60
SC12-Fork.UP	DIN 912 Stainless steel A2 70 M6X30	6.0	8793	19792	200	208	1.5	25.56
SC12 - Composite	DIN 912 Stainless steel A2 70 M6X30	6.0	8793	19792	200	208	1.5	25.56
SC10-Fork.UP	DIN 912 Stainless steel A2 70 M6X31	7.0	8793	19792	-216	208	1.5	29.05
SC10 - Composite	DIN 912 Stainless steel A2 70 M6X32	8.0	8793	19792	-216	208	1.5	29.05
SC11-Fork.UP	DIN 912 Stainless steel A2 70 M6X33	9.0	8793	19792	-165	208	1.5	28.60
SC11 - Composite	DIN 912 Stainless steel A2 70 M6X34	10.0	8793	19792	-165	208	1.5	28.60
SC4-machnd_piece_Down	DIN 912 Stainless steel A4 70 M4X22	4	3908	8796	-1347	130	1.5	3.35
SC4- Composite	DIN 912 Stainless steel A4 70 M4X22	4	3908	8796	-1347	130	1.5	3.35
SC3- downPlate	DIN 912 Stainless steel A4 70 M4X22	4	3908	8796	-24	130	1.5	19.22
SC3- composite	DIN 912 Stainless steel A4 70 M4X22	4	3908	8796	-24	130	1.5	19.22
SC1-maquinado.Down	DIN 912 Stainless steel A4 70 M4X22	4	3908	8796	932	105	1.5	5.24
SC1 - Composite	DIN 912 Stainless steel A4 70 M4X22	4	3908	8796	932	105	1.5	5.24
SC2- composite	DIN 912 Stainless steel A4 70 M4X22	4	3908	8796	24	105	1.5	23.41
SC2- downPlate	DIN 912 Stainless steel A4 70 M4X22	4	3908	8796	24	105	1.5	23.41
SC5-machnd_piece_Down	DIN 912 Stainless steel A4 70 M4X22	4	3908	8796	970	115	1.5	4.99
SC5- Composite	DIN 912 Stainless steel A4 70 M4X22	4	3908	8796	970	115	1.5	4.99
SC6- composite	DIN 912 Stainless steel A4 70 M4X22	4	3908	8796	24	115	1.5	21.46
SC6- downPlate	DIN 912 Stainless steel A4 70 M4X22	4	3908	8796	24	115	1.5	21.46
SC8-machnd_piece_Down	DIN 912 Stainless steel A4 70 M4X22	4	3908	8796	-1377	137	1.5	3.26
SC8- Composite	DIN 912 Stainless steel A4 70 M4X22	4	3908	8796	-1377	137	1.5	3.26
SC7- composite	DIN 912 Stainless steel A4 70 M4X22	4	3908	8796	-24	137	1.5	18.20
SC7 - downPlate	DIN 912 Stainless steel A4 70 M4X22	4	3908	8796	-24	137	1.5	18.20
SC27 - machined.Cil	Ck45 small Pin	6	9576	16540	5	1561	1.5	3.09
SC27 - Pino Principal	Ck45 small Pin	6	9576	16540	5	1561	1.5	3.09
SC28- Pino Principal	Ck45 small Pin	6	9576	16540	11	1578	1.5	3.04
SC28 - machined.Cil	Ck45 small Pin	6	9576	16540	11	1578	1.5	3.04
SC9095-machined.Cil	Ck45 small Pin	6	9576	16540	-49	1458	1.5	3.39
SC9095- Main Pin	Ck45 small Pin	6	9576	16540	-49	1458	1.5	3.39
SC9096- Main Pin	Ck45 small Pin	6	9576	16540	-54	1449	1.5	3.42
SC9096- machined.Cil	Ck45 small Pin	6	9576	16540	-54	1449	1.5	3.42
SC9094 - horizontal_Ear	DIN 912 Stainless steel A4 70 M4X22	4	3908	8796	-822	221	1.5	6.14
SC26- horizontal_Ear	DIN 912 Stainless steel A4 70 M4X23	4	3908	8796	-47	413	1.5	5.34
SC26 - horizontal_Ear	DIN 912 Stainless steel A4 70 M4X24	4	3908	8796	-47	413	1.5	5.34
SC - 25 - fibra UAV	DIN 912 Stainless steel A4 70 M4X25	4	3908	8796	84	46	1.5	45.67
SC - 22 - fibra UAV	DIN 912 Stainless steel A4 70 M4X26	4	3908	8796	121	71	1.5	29.72
SC - 21 - fibra UAV	DIN 912 Stainless steel A4 70 M4X27	4	3908	8796	123	72	1.5	29.38
SC - 18 - fibra UAV	DIN 912 Stainless steel A4 70 M4X28	4	3908	8796	46	87	1.5	28.14
SC - 25 - vertical_Ear Sup	DIN 912 Stainless steel A4 70 M4X29	4	3908	8796	84	46	1.5	45.67
SC - 22 - vertical_Ear inf	DIN 912 Stainless steel A4 70 M4X30	4	3908	8796	121	71	1.5	29.72
SC - 21 - vertical_Ear inf	DIN 912 Stainless steel A4 70 M4X31	4	3908	8796	123	72	1.5	29.38
SC - 18 - vertical_Ear Sup	DIN 912 Stainless steel A4 70 M4X32	4	3908	8796	46	87	1.5	28.14

Table 49 - General information of the landing gear FEM model

Part	Property Type	Elements Number	Nodes Number	Element Size [mm]	Element Type
Leaf Spring	PCOMP5	174	210	10	CQUAD
Fuselage Composite frame	PCOMP6	217	282	10	CQUAD
Fork	PSHELL9	130	169	10	CQUAD
Connection plate Vertical	PSHELL 112	30	48	10	CQUAD
Connection plate Horizontal	PSHELL 106	30	42	10	CQUAD
Up plate	PSHELL 108, 10 and 107	321	347	10	CQUAD
Down Plate	PSHELL 03	24	35	10	CQUAD

Annex D: NATO Email contact

"Good morning,

My name is José Miguel Silva and I'm working in my master thesis: "Development of a nose landing gear of an unmanned aircraft (RPAS) ".

I'm writing to you because I think that I've found some mistakes in the AEP 83 STANAG 4703, more precisely in the "UL.GL.1 Basic Landing Conditions " table.

Where for "both main wheels (Dr)" and Tail (nose) wheels (Dr) I think that it should be "nj" instead of "n", and in Tail (nose) wheels (Vr) it should be (n-L)W b'/d' instead of
 (n-L)W'/d' .

Best Regards,
José Miguel Silva"